UNIVERSITY OF CALIFORNIA

Santa Barbara

Space-time variability of bio-optical properties in the Southern California Bight

A dissertation submitted in partial satisfaction of the

requirements for the degree Doctor of Philosophy

in Geography

by

Fernanda Henderikx Freitas

Committee in charge:

Professor David A. Siegel, Chair

Professor Tommy Dickey

Professor Libe Washburn

December 2015

The dissertation of Fernanda Henderikx Freitas is approved.

_____

Tommy D. Dickey

_____

Libe Washburn

_____

David A. Siegel, Committee Chair

December 2015

Space-time variability of bio-optical properties in the Southern California Bight

ACKNOWLEDGEMENTS

I have a lot of people to thank for these past 5 years. In 2008, in the middle of a M.Sc. crisis, I read a paper by David Siegel and decided to write a long-shot email to his team to ask for some data. A few hours later, David Court sent me all the data they had, pretty much saving my thesis (Thank you D. Court!). I then decided that working with those generous people one day would be an honor. Somehow, David Siegel accepted me as his graduate student in 2010 without ever having met me. One of those right place – right time moments, a.k.a. a small miracle. Dave has been a real source of inspiration, and I hope I was able to absorb a little bit of his abilities during these years. Dave, you are the best advisor I could have asked for, so thank you so much for everything.

I want to thank the NASA Earth Space and Science Fellowship for allowing me the privilege of working solely on the stuff that I love. Thank you to the many other funding sources that supported me as well: the Geography Department for giving me the opportunity to teach Remote Sensing courses; the Earth Research Institute, Marine Science Institute and the BON project for the travel grants and summer fellowships; and the SBC-LTER for supporting my research and for investing on the glider back in 2010. More specifically, I'd like to thank Dr. Dan Reed, Dr. Bob Miller, Mo Lovegreen, Jose Saleta and the faculty at the Geography Department and the Marine Science Interdepartmental Program.

Three people in particular were absolutely crucial to the development of my research. Thank you Stuart Halewood and Erik Stassinos for teaching me everything I know about how the glider works and for turning me into a pseudo-glider engineer. Thank you for your enthusiasm and the many hours troubleshooting and talking about science and life. Thanks also to Erik Fields, who made work so much easier for me with Chapter Three! I truly

enjoyed being around you guys.

Thank you Nathalie Guillocheau and all the Plumes and Blooms crew for the great data. Thank you Dr. Melanie Fewings and Dr. Debora Rodriguez for inspiring me to be a better scientist. Thank you Dr. Leonel Romero and Dr. Carter Ohlmann for always giving great advice. Thank you Chris Gotschalk for the many how-to matlab requests and Darla Sharp for showing me the Unix ways.

Thank you Maiana Hanshaw for your presence, no matter where in the world we are. Thank you Alicia Cortes for being my guru for post-PhD life. My cohort and lab mates have also provided lots of laughter and nerdy talks. Special thanks to Tom Bell, Rebecca Barron, Eli Aghassi, James Allen, Kelsey Bisson and Nick Dellaripa. Thanks also to Chantal Swan and Tiho Kostadinov, which I have only met a couple of times, but were serious sources of motivation. Thank you Diana Repogle-Purinton for re-igniting my love for dancing, keeping me sane, and thank you Orange for brightening up my day.

To my mentors, David Siegel, Tommy Dickey, Libe Washburn and Stefane Maritorena, thank you for reading so many drafts of everything, and for your encouragement. To Dave, thank you for letting me go to so many conferences, for inviting me to meetings, for introducing me to the right people, for reading rough drafts, for your recommendation letters, for helping me see the big picture, and for allowing me to be independent and figure things out on my own.

To Bob Lansdorp, thank you for making me laugh and for your endless strength and support. And then there are my parents. My favorite people. Mom, you are the most incredible person I have ever met. I learn from you every day. Dad, I miss you so much already. I wouldn't be here today without their unconditional love and support.

DEDICATION

I dedicate this dissertation to my dad. Obrigada por tudo, pai!

VITA OF FERNANDA HENDERIKX FREITAS
December 2015

EDUCATION

Bachelor of Science in Oceanography, Universidade Federal do Parana, Brazil (summa cum laude). Sep. 2007.
Master of Science in Geo-Information Science and Earth Observation, University of Southampton (UK), Lunds Universitet (Sweden), Warsaw University (Poland) and University of Twente (The Netherlands). Mar. 2009.
Doctor of Philosophy in Geography, University of California, Santa Barbara. Dec 2015.

PROFESSIONAL EMPLOYMENT

2009-2010: *Spatial Analyst* for the Food and Agriculture Organization of the United Nations, Brasilia, DF, Brasil
2010-2011: *Teaching Assistant*, Department of Geography, University of California, Santa Barbara
2011-2015: *Graduate Research Assistant*, University of California, Santa Barbara
2015: *Teaching Associate*, Department of Geography, Un. of California, Santa Barbara

AWARDS

Conselho Nacional de Desenvolvimento Cientifico e Tecnologico Studentship (2004-2007, Brasil)
Erasmus Mundus Joint Masters Degree Scholarship (2007-2009, The Netherlands)
NASA Earth and Space Science Fellowship (2011-2014, USA)
NASA/University of Maine Ocean Optics Summer class scholarship (2011, USA)
Earth Research Institute Summer Fellowship (2015, USA)

PUBLICATIONS

"Space-Time variability of bio-optical properties in the Southern California Bight" Unpublished thesis submitted in partial fulfillment of the requirements for the Doctor of Philosophy in Geography, University of California, Santa Barbara, 2015. 192pp.

"Assessing controls on cross-shelf phytoplankton and suspended particle distributions," *In Review at the Journal of Geophysical Research* (December 2015).

"Satellite assessments of particulate matter and phytoplankton variations in the Santa Maria Basin and Southern California Bight". *In prep*.

FIELDS OF STUDY

Major Field: Oceanography
Minor Fields: Optical Oceanography; Remote Sensing; Coastal oceanography

ABSTRACT

Space-Time variability of bio-optical properties in the Southern California Bight

by

Fernanda Henderikx Freitas

This dissertation examines the variability of physical and bio-optical properties in the Southern California Bight over various time and space scales. The research is divided into three chapters, and each chapter was written mostly as stand-alone pieces. An abstract is presented for each, and Tables, Figures and Appendices that support the text are shown at the end of each specific chapter. A list of all the references used in the text is shown at the end of the dissertation.

In ***Chapter One***, ***"Assessing controls on cross-shelf phytoplankton and suspended particle distributions",*** an underwater glider was used to "super-sample" the inner and mid-shelf Santa Barbara Channel (from 20 to 70m depth), providing data in detail never before observed. Highly resolved glider data in time and depth for a 4km long section perpendicular to the coast allowed answering questions such as: what is the space-time distribution of bio-optical properties (specifically phytoplankton and sediments) in the inner/mid-shelf SBC? And, what are the main controls on the variability of these properties? Six glider missions were completed, sampling a wide range of environmental conditions (e.g. upwelling, highly stratified, large blooms, small blooms, intense mixing). A storm

event was also captured by the glider, providing a unique view of its evolution and effect on bio-optical properties. This confirmed the importance of instruments such as gliders in sampling events that are normally missed by ships and satellites. The data allowed characterizing the coastal zone in terms of surface, bottom and intermediate nepheloid layers of various compositions that evolve according to specific stratification conditions. Winds, precipitation, waves, and surface currents were used to infer some of the drivers of the variability. Waves were found as the main controls on sediment re-suspension during the storm mission, and advection processes were related to local changes in phytoplankton abundances. Unique examples of high-frequency events, such as the cross-shore propagation of a phytoplankton patch, the interaction between tides and sediment re-suspension and the co-evolution of phytoplankton and non-biogenic materials in similar portions of the water column – determining the complexity of the coastal ocean - are shown and discussed.

In ***Chapter Two***, ***"Transport and Fate of heat, salt, oxygen and particles in the innershelf Santa Barbara Channel, CA"***, the capabilities of the glider dataset are explored even further to ask questions that are in the very core of the studies in upwelling environments: How important is the cross-shelf exchange of materials to the health of nearshore ecosystems? Is the innershelf a source or a sink for particles/heat/salt? Is the nearshore zone net autotrophic or net heterotrophic? Do source/sink patterns change over time? Although the glider was not equipped with velocity meters, this study takes advantage of the Acoustic Doppler Current Profiler moored at the 10m isobath just North of the shallowest glider observations to provide depth-resolved velocity estimates for the calculations of biogeochemical fluxes across the innershelf. Despite large uncertainties, interesting patterns of the nearshore zone acting as a source or sink for phytoplankton,

sediments and oxygen are observed for the different missions. Nonetheless, this study shows the feasibility of using depth-resolved instruments to assess cross-shore transport of biogeochemical properties, and provides insights into how an experiment should be designed to properly obtain those fluxes estimates in the future.

Chapter Three, ***"Satellite assessments of particulate matter and phytoplankton variations in the Santa Maria Basin and Southern California Bight",*** takes a larger scale approach to determine what drives bio-optical variability in the Southern California Bight and Santa Maria Basin. This study took advantage of the now more than 13 years worth of quality optical imagery from SeaWiFS, MODIS and MERIS sensors, which were spectrally merged using a bio-optical algorithm to increase space-time coverage. 8-day composites and 2-km pixel sizes were used in the analysis, allowing the observation of weekly to seasonal and inter-annual changes in bio-optical properties, as well as long-term trends. Controls on chlorophyll distribution were different in different portions of the domain, indicating the importance of regional scale upwelling and larger scale changes in circulation patterns in determining productivity. Controls on backscatter far from shore mimicked the observed for chlorophyll. Near the coast, however, changes in backscatter were shown to be modulated by waves throughout the seasons and, episodically, by the large discharge events associated with El Niño conditions.

TABLE OF CONTENTS

CHAPTER ONE

Assessing controls on cross-shelf phytoplankton and suspended particle distributions

Abstract

Characterizing the space/time variability of bio-optical properties is essential to understanding the mechanisms that control cross-shelf phytoplankton and suspended particle distributions in coastal waters. Approximately 400 high-resolution cross-shelf sections of physical and bio-optical data, which were collected with an oceanographic glider in the innershelf Santa Barbara Channel, California, revealed complex relationships among optical properties and the potential driving mechanisms controlling their distributions. While the seasonal cycle was responsible for much of the variability in physical properties, strong episodic events dominated variability in chlorophyll-fluorescence and optical backscatter measurements. Variability in suspended particle loads was well correlated with changes in significant wave height, whereas the occurrence of phytoplankton blooms was linked to advection and upwelling events, exemplifying the impacts of local versus remote controls on cross-shelf particle distributions. Conceptually, particle and phytoplankton distributions were characterized by the superposition of surface, intermediate and bottom nepheloid layers that intermittently dominate the inner and mid-shelves. The observations illustrate the processes regulating phytoplankton and particle transport in the innershelf and show the difficulty in establishing general connections between high-frequency changes in optical properties and potential environmental forcings in a complex coastal environment.

1. Introduction

The innershelf, considered here to be the region bounded by the surf zone to roughly 40m depth, can be thought as the interface between land and ocean environments and it hosts many of the most productive ecosystems on Earth [*e.g. Cloern et al*., 2014]. In upwelling-dominated systems such as the Santa Barbara Channel (SBC), California, the functioning of coastal ecosystems is controlled by the space-time variability in biological activities of the pelagic and benthic communities and the exchanges of ecological materials to and from the innershelf [*Rowe et al*., *1975*; *Miller et al*., 2011]. A variety of physical processes facilitate the cross-shelf exchanges of biogenic and abiotic materials. These include surface wave- and wind-driven circulation [*Lentz and Fewings,* 2012], internal wave breaking and dissipation [*Lamb,* 2014], meso- and submeso-scale eddies [*Bassin et al*. 2005; *Brzezinski and Washburn,* 2011], tides [*Chang et al.,* 2002], horizontal mixing and dispersal [*Romero et al.,* 2013] and terrestrial runoff [*Warrick et al*. 2004; *Otero and Siegel*, 2004]. Understanding the mechanisms that control the distribution of phytoplankton and suspended particles in the innershelf is essential to improve estimates of export and production of organic matter, and monitor the health of important ecosystems with a changing climate.

In-water constituents in these shallow environments include dissolved and particulate materials of various sizes and compositions. These include mineral sediments, dissolved organic matter, bacteria, phytoplankton, zooplankton and detritus of a variety of origins. Variations in the concentrations and characteristics of these materials lead to changes in the bulk optical properties of the water column [e.g., *IOCCG*, 2000; *D'Sa and Miller*, 2005;

Kostadinov et al., 2011]. Thus, optical properties of different particles can be used as proxies for biological and suspended sediment quantities. For example, chlorophyll-fluorescence can be used as a proxy for the presence of phytoplankton and, with caution, phytoplankton abundances [*Cullen* 1982; *Roesler and Barnard*, 2013]. Optical backscattering coefficients have been used as proxies for suspended particle [*Stramski et al*., 2004] as well as particulate organic carbon concentrations [*Stramski 1999*; *Babin et al*., 2003]; however, the quantitative relationship depends significantly on particle size, index of refraction, and shapes [*Stramski* 1999; *Antoine et al*., 2011]. These relationships are particularly complex in shallow coastal waters where algal blooms are patchy and can occur rapidly [*Omand et al.,* 2011], detritus and sediments contribute to the backscatter signal [*Boss et al.,* 2001], benthic communities are important transformers of organic matter [*Huettel et al., 2014*] and decoupling between abundances of autotrophs and hetereotrophs can occur on short time and space scales [*Lefort and Gasol*, 2013].

Vertical distributions of suspended particulates in the innershelf generally reveal layers that are known as surface (SNL), bottom (BNL) or intermediate nepheloid layers (INL), depending on where in the water column they occur [e.g., *Pak et al.,* 1980; *McPhee-Shaw and Kunze*, 2002; *McPhee-Shaw* 2006]. Biologically produced particles are thought to accumulate near the surface around the thermocline due to sufficient light, nutrient, temperature and mixing conditions, which also influences their cross-shelf distribution. These surface nepheloid layers can also be formed by detritus and other inorganic materials advected from shallower regions as a result of river runoff or intense mixing activity. Bottom nepheloid layers tend to resemble Rouse-like profiles where particle concentrations decrease roughly exponentially with height above the seafloor [*Rouse*, 1937; *Glenn et al*., 2008], and

are generally comprised of sediment and particulate materials released by the benthos. Variability in the shape and intensity of BNLs is largely dependent on how surface waves and currents control the stirring, vertical mixing and net gravitational settling rates of particles [*Glenn et al.*, 2008]. Intermediate nepheloid layers can be completely detached from the bottom or co-occur with BNLs [*Cacchione and Drake*, 1986; *Lamb*, 2014]. INLs are made up of materials of various sources and mechanisms that support their development include the breaking of internal waves along slopes and subsequent transport along isopycnals [*Pak et al*., 1980; *Cacchione and Drake*, 1986; *McPhee-Shaw and Kunze*, 2002; *Bogucki et al.,* 2005], as well as the splitting of near-bottom gravity currents [*Cortes et al*., 2014]. Thus, INLs are thought to be important in the offshore transport and delivery of nutrients, organic and inorganic materials from innershelf ecosystems.

Understanding the space-time distribution of these layers requires concurrent high-resolution observations of physical and bio-optical properties. Traditional ship-based measurements often fail to properly sample high frequency events due to typical cruise lengths and sampling strategies, providing information at only a few points in time and with multi-kilometer resolution. Moorings obtain temporally resolved observations, but usually with limited spatial coverage. Satellites have proven useful to examine bio-optical interactions over multi-km spatial and multi-day temporal scales [*Otero and Siegel,* 2004; *Kahru et al.,* 2009], but undersampling due to cloud cover, long sensor revisit times, as well as the biases resulting from daytime- and surface-only sampling, limit understanding of the complexity of ocean processes [*Wiggert et al.,* 1994; *Gregg and Casey*, 2007]. Autonomous vehicles such as gliders and floats have recently emerged as revolutionary approaches for

observing variability of in-water constituents over ecologically relevant space and time scales [*Webb et al.,* 2001; *Perry and Rudnick*, 2003; *Dickey et al*., 2008; *Rudnick*, 2015].

In this Chapter, high-resolution physical and bio-optical data obtained by an underwater glider are used to characterize the spatial and temporal variability of particle distribution across the inner and mid-shelf SBC, with the goal of identifying bio-optical signatures that determine the sources, fates and transport of phytoplankton and suspended particle distributions. Links between physical forcings and spatiotemporal patterns of particle distributions are discussed, including the role of waves, stratification and advection. Examples of high-frequency cross-shelf optical processes highlight the strength of underwater vehicles in characterizing the complexity of the inner and mid-shelves, but also illustrate the difficulties in establishing causality between short-term optical changes and physical forcings that interact over various time and space scales.

2. Methods

2.1. Study Site and Glider Deployments

The study site was the inner and mid-shelf Santa Barbara Channel (SBC; Figure 1), where an underwater 200m Teledyne Webb Research G2 Electric Glider (http://www.webbresearch.com/) sampled a top-to-bottom, 4.25-km long cross-shelf section between the 18 and 70 meter isobaths. The sampling transect was located south of the Mohawk Kelp Forest, a core Santa Barbara Coastal Long-Term Ecological Research site (SBC-LTER). Glider data presented here include conductivity, temperature and pressure

from a pumped CTD (SeaBird SBE-41); chlorophyll-fluorescence (excitation 465nm / emission 695nm; WETLabs ECO Puck FLBBCDSLK); and volume scattering function (VSF) at 650nm (θ=117°, 20nm spectral bandwidth, WETLabs ECO Puck BB3SLK). Data were collected in a saw-tooth pattern, from ~0.5m below the surface to ~1m above the bottom with a sampling rate of 0.25 Hz. Typical glider forward velocities were ~0.3m/s, resulting in an average horizontal resolution of 50m.

The glider flew repeatedly between two pre-determined waypoints, with each completed path defined as a section. The vehicle was programmed to surface every 3 hours to acquire its GPS position. When surfacing occurred between waypoints, segments were added together to form one section. GPS fixes and gliding displacement between surfacing events provided estimates of depth-averaged currents. Sections were completed in less than 3.5 hours 80% of the time, but on average four sections were completed each day since the glider was at times subjected to strong alongshore advection while on the surface. Data during periods when the glider adjusted positions were not included in the analysis. The effect of alongshore advection on the glider paths can be partially observed in Figure 1.

The glider was deployed in six 2-3 week long missions in March 2012 (hereafter Mission 4, or M4), July 2012 (M5), September 2012 (M6), December 2012 (M7), February 2013 (M8) and June 2013 (M9). In total, sampling spanned 92 days, and 404 final sections were selected. Missions 1 to 3 were test deployments and are not discussed here. Table 1 provides a summary of the six missions. Sampling occurred over a large range of environmental and oceanographic conditions. For example, M4 was dominated by an upwelling event while missions M5 and M6 occurred during summer, stratified conditions. The largest phytoplankton blooms were recorded during M5. Mission M7 occurred during a winter

storm, with interesting observations of particle re-suspension processes. M8 sampled weakly stratified conditions during upwelling and M9 showed a diverse mix of strong stratification, upwelling, blooms and re-suspension events.

2.2 Data Processing and Quality Control

A variety of quality control measures were applied to the glider data. Glider transects were excluded if paths were shorter than 2000 data points or if tracks spanned less than 0.01 degrees in latitude (~1km). Biofouling of the optical sensors was observed only during M9 (the longest mission) where the VSF data quickly drifted to saturation values. Data with these symptoms were removed. For the optical sensors, dark measurements obtained before each mission were subtracted from the raw optical data.

Mismatches between temperature measurements of the first dive after a surfacing event and the subsequent upcast data were observed and attributed to bubbles in the CTD pump, with discrepancies usually disappearing by the start of the second dive. All data with these issues were excluded from analysis.

Triplicate surface water samples at the inshore, mid-way, and offshore waypoints were collected and analyzed for the chlorophyll-a concentration during missions M5, M6 and M7 to calibrate the chlorophyll fluorometer. Comparisons between in-situ chlorophyll concentrations and dark-subtracted glider chlorophyll-fluorescence averaged over the top 5 meters yielded a linear correlation coefficient of r=0.82 (*p-value*<0.05; n=9; [Chl mg/m^3]=0.0159*(dark corrected chl counts)-0.0165). Dark-corrected chlorophyll fluorescence values are reported here as *chl-fl*, and are assumed to be to first order a proxy for phytoplankton abundance.

Conversion from scaled, dark-subtracted VSF to particle backscatter at 650nm was performed as described in the WETLabs manual (www.wetlabs.com). First, particulate VSF was obtained by subtracting the scattering by pure seawater as given by *Zhang et al.* [2009] for the corresponding *in situ* glider temperature and salinity. Particulate VSF from a single angle (θ = 117°) was converted to particle backscatter (b_{bp}) using the relationship $b_{bp} = 2\pi\chi\beta_p(\theta)$, where χ is an angle-dependent dimensionless factor equal to 1.1 based on *Boss and Pegau* [2001]. All particle backscatter data at 650nm is hereafter referred to as b_{bp}.

Values of b_{bp} are composed of both biotic and abiotic particulates. In the absence of phytoplankton, b_{bp} can be converted into total suspended matter units using independent data from the Plumes and Blooms Project (http://www.eri.ucsb.edu/research/groups/plumes-and-blooms; Stations on Figure 1). First, the slope of a regression line between concurrent surface lithogenic silica (LSi; from bottle measurements) and particle backscatter at 671nm (the closest spectral measurement to the glider's 650nm; from a Hydroscat-6 sensor) is obtained using data from the two Plumes and Blooms stations closest to shore, and during times with chlorophyll concentrations <1mg/m^3 (Estimated LSi = 228* b_{bp}; r^2 = 0.32; n=41). Given the reportedly nearly flat spectral slopes for b_{bp} [*Kostadinov et al*. 2009; 2012], the difference between $b_{bp}(650)$ and $b_{bp}(671)$ is considered to be negligible. Finally, LSi estimations can be converted into TSM using an average clay molecular weight of 110 gmol^{-1} Si (i.e. 1 µmol L^{-1} LSi = 0.11 mg L^{-1} sediment) as in *Warrick et al.* [2004].

2.3. Ancillary Data

Wind velocity data were obtained from NOAA's National Data Buoy Center (NDBC) 46053, 17-km South from the study area

(http://www.ndbc.noaa.gov/station_page.php?station=46053). Significant wave height, peak wave period and peak wave direction were obtained from NDBC buoy 46216 (http://www.ndbc.noaa.gov/station_page.php?station=46216), 8-km Southwest of the study area; see Figure 1). Significant wave heights and wave periods at buoys 46053 and 46216 showed very good correspondence (r=0.92 and r=0.86, respectively; p-value<0.001). No wind information was available at NDBC buoy 46216, and no wave direction was available at NDBC buoy 46053. Wind stress was estimated using algorithms described by *Edson et al.* [2013], and rotated into principal axis coordinates, such that by convention negative values refer to upwelling favorable winds that blow towards the east and parallel to the coast [*Brzezinski and Washburn*, 2011]. Tidal heights were obtained from the Santa Barbara's Stearns Wharf pier (3.6km from study area; maintained by the SBC-LTER, sbc.lternet.edu). Tide, wind, significant wave height, wave period and wave direction data were assembled as 3 hour averages around the mean timestamp of each glider section to allow direct comparison. Fifteen-minute resolution precipitation records were obtained from the Coal Oil Point Reserve coastal weather station (http://www.geog.ucsb.edu/ideas/), and were transformed into accumulated rainfall over a 3-hour period, after which the closest values to each glider section timestamp were selected.

High-frequency (HF) radar provided hourly surface vector current data (top 1m) over the SBC (with coverage including the mid-shelf portion of the glider sections) on a 2-km grid (CODAR Ocean Sensors, Ltd.; http://hfrnet.ucsd.edu/threadds/HFRADAR_USWC_hourly_RTV.html). Details about the HF methodology and data processing are found in *Paduan and Washburn* [2013]. The East-West component of HF radar data (sea surface alongshore velocities) at the HF radar grid-

point closest to the glider sections and glider depth-averaged alongshore velocities showed reasonable agreement (r=0.54). Additionally, relative vorticity (ζ) calculated from HF radar data at 120.1W/34.3N, near the typical center of the mean SBC eddy [*Nishimoto and Washburn*, 2002; Figure 1; small changes in the choice of eddy center yielded similar ζ temporal patterns (not shown)], were used as a measure of eddy strength. Values of ζ were estimated by finite differences over a 3x3 velocity grid field ($\zeta = \Delta V/\Delta x - \Delta U/\Delta y$, where Δx and Δy are twice the 2 km grid spacing in the east and north directions, respectively). Values of ζ were normalized by the local Coriolis parameter, and displayed as ζ/f. Positive values refer to cyclonic, counter-clockwise rotation.

2.4. Statistical Analyses

Ordinary krigging (GLOBEC Kriging Software Package v3.0) was used to spatially interpolate sections of physical and bio-optical glider data onto a common spatial grid of thirty-five 2m bins in depth and forty 100m bins in the cross-shelf direction, and also to extrapolate measurements to surface, bottom waters, and cross-shelf extremities when necessary. A common bottom mask was created based on the average glider altimeter data and overlaid on all final 4-km long gridded sections, resulting in a depth-range of 20m inshore and 68m in the offshore portion of the section. For a detailed view of the section-by-section snapshots of physical and optical properties, refer to the movie in Appendix A.

Variability of bio-optical glider data within the six missions was examined using empirical orthogonal function (EOF) analysis, a statistical technique that partitions the variability of a time evolving dataset into a set of uncorrelated spatial modes and independent, time varying amplitude functions [e.g., *Emery and Thomson,* 1997]. The first

modes explain more of the total variance compared with subsequent ones, and the sum of all EOF modes weighted by their amplitude functions reconstructs the original signal. The spatial / temporal EOF patterns provide useful means for describing the importance of various processes to the observed total variability. EOFs were performed on time-mean subtracted data [*Bjornsson and Venegas,* 1997].

Amplitude function values can be negative or positive, and values around the zero crossing suggest a weak importance of the corresponding spatial mode at those times. Therefore, extreme amplitude values potentially hold additional information on what drives each mode's variability. Following *Anderson et al.* [2008], tails of ranked histograms were used to identify sections corresponding to the 15 positive and 15 negative extremes in the amplitude time series for each dominant mode. Extremes were compared for similarity using the nonparametric two-tailed Wilcoxon-Mann Whitney test.

3. Results

3.1 Mean Cross-Shelf Patterns

Cross sectional means of temperature, *chl-fl* and b_{bp} and their variability highlight the bio-optical complexity of the water column and how particle distributions respond to mean physical ocean conditions (Figure 2). The overall mean temperature section for the periods sampled (Figures 2a) showed a general upward cross-shore tilt of the thermocline towards the coast over the top 20m, with temperatures on average higher in the offshore portions of the sections. Below 30m, the tilt is reversed. These features are consistent with the coastal setup and setdown due to winds, waves and geostrophic along-shelf flows that together

determine circulation patterns in shallow environments [*Lentz and Fewings*, 2012]. Standard deviations in temperature (Figure 2b) are larger near the surface, reflecting thermal changes over the seasons.

Cross-shelf averaged values of *chl-fl* in the top 30m were ~4 mg/m^3 (Figure 2c), consistent with the observations of *Goodman et al.* [2012] at the same location in 2008-2009, but variability in the upper 25 m of the water column was often larger than the mean (Figure 2d). On average, a subsurface *chl-fl* maximum was observed centered around 18m, which likely corresponds to a maximum in phytoplankton biomass. A fraction of the low *chl-fl* values observed just below the surface are attributable to non-photochemical quenching of phytoplankton fluorescence (NPQ), a process that acts to reduce stimulated fluorescence during daylight hours [*Cullen*, 1982; *Roesler and Barnard*, 2013]. Evidence for NPQ was observed during nearly all missions over the top few meters of the water column (see Appendix B). Although the importance of NPQ in interpreting short-term changes in near-surface *chl-fl* values is certainly acknowledged, it affected surface waters of fewer than 12% of the sections. Thus, no correction was attempted and the general statistical techniques used here are not believed to be significantly affected by these issues.

Optical backscatter determinations spanned over a four-fold variation throughout the water column over the six missions (Figure 2e-f). The highest b_{bp} values were observed along the bottom slope, consistent with the persistence of bottom nepheloid layers. Near the surface, a band of elevated b_{bp} values at ~15m likely represents a mixture between biogenic-origin particles and abiotic materials advected from shallower areas. The lowest b_{bp} values were found at mid-depth in the offshore portion of the section, away from scattering sources. Variability was the highest along the bottom and around the 40m isobath (Figure 2f),

depicting variations in the strength of near-bottom re-suspension and flow detachment events within intermediate nepheloid layers.

3.2 Co-variability between phytoplankton and particles

The relationship between co-occurring *chl-fl* and b_{bp} observations and their depth-distribution shown in Figure 3a provides additional information on the types of materials present in the water column. The b_{bp}:*chl-fl* relationship is generally clustered along two main axes, which explains the low overall correlation coefficient of r=-0.13 between the two parameters (or r=-0.23 if calculated on log-transformed observations). High b_{bp} - low *chl-fl* values characteristic of highly refractive and non-fluorescing particles such as mineralogenic materials and particulate detritus were roughly confined to deeper waters (Figure 3a), while elevated *chl-fl* - low b_{bp} values denoting phytoplankton populations were observed more often near the surface (see also Figure 2). Spatially, b_{bp} and *chl-fl* are only significantly correlated in the upper 10-20 m of the water column where b_{bp} is likely of biological origin (Figure 3b). At depth, insignificant correlations are observed, which is typical of shallow coastal systems where detritus, sediments and other materials make up a large part of the optical properties but do not co-vary with phytoplankton abundances.

Biologically, *chl-fl* signals are a direct indication that phytoplankton are present in the water sample; however the b_{bp} signal is made up of all water constituents that scatter light. Separating the biological component of b_{bp} from the mineralogenic components is essential to understand the space-time variability of phytoplankton and other (non-fluorescing) particles. A transformation of the b_{bp} vs. *chl-fl* relationship into suspended particles vs. phytoplankton was performed by first defining b_{bp} and *chl-fl* endmember vectors following the trend lines at

large b_{bp} and *chl-fl* values and linearly transforming all b_{bp} and *chl-fl* data pairs (see reference endmembers in Figure 3a). Thus, the new x axis, now called P_{sed}, is assumed to represent purely suspended particles, while values along the y axis, now called P_{bio}, are comprised exclusively of phytoplankton (Figure 3c). Data points in between the two axes naturally represent mixed samples where phytoplankton and inanimate particles co-exist. The b_{bp} to P_{sed} transformation shows a reduction in the contribution of biogenic particles to the pool of suspended materials near the surface (compare Figures 2e and 2g), although a near-surface residual P_{sed} signal potentially caused by non-photochemical quenching effects on *chl-fl* retrievals is still observed. The residual signal is only a small portion of the values observed (~5% above background values per section), and as such is likely negligible. Spatially, the linear transformation also led to a reduction in the correlation between P_{sed} and P_{bio} in surface waters (Figure 3d), while in deep waters the relationship is now weakly negative. To aid interpretations, P_{sed} was converted to TSM units (see Section 2.2), and generally referred here as "suspended sediments". P_{sed} and P_{bio} are used in all further analysis.

3.3. Physical setting and time-evolution of particle distributions

Understanding the physical and environmental conditions at the time of glider observations is important for assessing the causes of changes in the observed bio-optical properties. Figure 4 shows the time evolution of a profile of P_{bio} and P_{sed} at the 40m isobath, about 1.2km from shore, as well as several environmental factors at the time of each section that help determine particle distributions. All missions are concatenated into a single time series (see Table 1 for reference). Mission M4 was short but sampled the densest waters of

the sampling period; during M5, a narrow sub-surface phytoplankton bloom yielded the largest P_{bio} values of all missions (up to 37 mg/m^3); blooms during M6 occurred deeper in the water column, and SNLs appear dominated by suspended sediments; during M7, winter storm conditions led to intense mixing and rapid increases in particle concentrations throughout the water column, with maximum mapped P_{sed} values of ~2500 mg TSM / m^3; during M8 particles were generally confined within BNLs; during M9, the co-occurrence of a bloom and a large re-suspension event following an upwelling event exemplifies the optical complexity of the study area (Figure 4a-b). Cross-shelf mean water temperatures show the expected annual cycle where the lowest mean values were observed during M4 and the highest during M6 (Figure 4c).

Environmental conditions throughout the missions also showed seasonal and episodic patterns. Wind stress was predominantly upwelling-favorable, but strong upwelling conditions were only observed during M8 and M9 (Figure 4d). A wind reversal event during the storm of M7 accompanied the largest rainfall event of the year (Figure 4d). Large surface waves were observed during the same winter mission, and comparable wave conditions were observed in M8 during upwelling conditions (Figure 4e). Wind stress magnitude and waves at NDBC 46053 for the 2012-2013 period showed a positive correspondence (r=0.44). Cross-shelf mean MLD values (defined as the depth where potential density increased by 0.125 kg/m^3 relative to the potential density at 1m depth) ranged from 5.2m (± 2.0m) to 20.2m (± 7.8m) over time, deepening up to 50m in the offshore portion of the sections during M7 (Figure 4f). Glider depth-averaged velocities and surface currents from HF radar showed strong variability with a tendency of net westward flows, as expected [*Harms and Winant*, 1988; Figure 4g]. Relationships between water velocities and winds were only observed on

episodic time scales (e.g. upwelling event during M8). Values of ζ/f for the SBC eddy were nearly always positive (cyclonic), with the strongest values (~0.2) occurring during M5 and M9 (Figure 4h).

3.4. Modes of variability of suspended particles and phytoplankton

EOF analysis was used to distinguish the dominant spatial (EOF-P_{sed} and EOF-P_{bio}; Figure 5) and temporal (AF-P_{sed}, AF-P_{bio}; Figure 6) modes of variability of P_{sed} and P_{bio} across the shelf. Mean cross-shelf P_{sed} patterns during the 15 highest and lowest AF extreme values for each P_{sed} mode are shown in Figure 7 to support the analysis (see also table in Appendix C).

The first three EOF-P_{sed} modes describe over 75% of the variance in P_{sed} observations (Figures 5a-c). EOF1-P_{sed} (Figure 5a) accounts for 56.6% of the variance, and, at first glance, spatial patterns resemble the mean distribution of particles in the water column (Figure 2g). Indeed, AF1-P_{sed} (Figure 6a) and mean cross-shelf P_{sed} values (Figure 4e) are highly correlated (r=0.99), such that positive and negative AF1-P_{sed} illustrate above and below average particle load concentrations, respectively. However, there are important differences between the two patterns: EOF1-P_{sed} shows strong signatures of intermediate nepheloid layers and weaker BNL compared with the mean P_{sed} distribution shown in Figure 2g. Further, the water column can, at times, be almost devoid of particulates as shown in the case of spatial patterns from the extremely low EOF1-P_{sed} values (Figure 7a-b). Above-average particle load events during M7 and M9 dominated changes in this mode's temporal evolution.

The second EOF-P_{sed} mode explains 13.4% of the variability in P_{sed} and highlights changes in the vertical structure of sediment distribution. The dipole pattern shown in Figure 5b indicates that different processes dominate waters above and below 40m depth, with positive AF2-P_{sed} values in Figure 6b referring to P_{sed} concentrations that increase with depth, and negative values indicating the reverse. The spatial patterns of P_{sed} during extreme negative and positive AF2-P_{sed} periods (Figures 7c-d) thus suggest that AF2-P_{sed} depicts the transition in temporal dominance between BNLs (positive AF2-P_{sed}) and INLs (negative AF2-P_{sed}). Most prominent BNL features were observed during M7 and M8, when stratification was weak. In contrast, INLs (negative AF2-P_{sed} values) were most commonly observed during M5, M6 and M9, when stratification was strong.

The third EOF-P_{sed} mode explains only 5.7% of the variability, but illustrates the importance of episodically strong re-suspension events across the shelf to the overall variability in total particle load. Patterns in Figure 5c indicate that positive AF3-P_{sed} values (Figure 6c) occur when the highest P_{sed} values are observed at mid-depths, while negative values depict times when innershelf P_{sed} dominates the signal. M7 dominates the negative extremes in this this mode, when wave heights, MLD, and rain conditions were at their most intense, while M9 dominates the positive extremes. Mean P_{sed} sections during the extreme negative and positive AF values in Figure 7e-f highlight the difference between the main re-suspension events in the time series, with M7 variability concentrated in the innershelf, and M9 variability occurring within intermediate nepheloid layers. The co-occurrence of the negative extreme AF3-P_{sed} peak and the largest AF1-P_{sed} peak in M7 (Figure 6c) indicate that the largest particle load event in the time series occurred in waters below 30m.

The first four EOF-P_{bio} modes account for 76.3% of the variance in phytoplankton distribution (Figures 5d-g). As expected, AF1-P_{bio} (Figure 6d) resembles the cross-shelf mean P_{bio} observations (Figure 4h; r=0.93) and explains 51.6% of the variance. Positive peaks in AF1-P_{bio} denote large abundances of phytoplankton, with M5 and M9 dominating the variability of the mode.

EOF2-P_{bio} explains 12.3% of the variance and shows an out-of phase relationship between P_{bio} above and below ~15m depth (Figure 5e). This mode will lift or depress the location of the subsurface phytoplankton maximum. Indeed, good correlation was found between AF2-P_{bio} and the mean depth of the chlorophyll maximum across the shelf (r=0.57; Table 2). Thus, positive AF2-P_{bio} values indicate shallower subsurface maxima, with M5 driving the changes in this mode.

The third P_{bio} EOF mode (Figure 5f) accounts for 6.7% of the variance in the data, with missions M5 and M9 driving the extreme negative and positive loadings, respectively (Figure 6f). This mode depicts changes of the thickness of the phytoplankton maximum, with positive AF3-P_{bio} referring to narrow patches dominating phytoplankton distribution especially during M5, and negative AF3-P_{bio} referring to broad, thicker patches as the observed throughout M6 and M9 (see Movie S1).

The fourth P_{bio} EOF explains 5.7% of the variance in phytoplankton distribution, and the cross-shelf dipole in Figure 5g represents conditions where P_{bio} is higher either offshore of the section (negative values) or inshore of the section (positive values). Indeed, slopes of a linear regression using cross-shelf P_{bio} values averaged over the top 20m of the water column showed good agreement with this mode (r=0.92). Alterations in cross-shelf gradients were observed throughout all missions, and overall, patches were preferentially located 3-5 km

offshore than in the inner 2 km of the sampling area. This observation is contrary to studies in the innershelf Southern California Bight which observed persistently higher phytoplankton biomass at depths shallower than 30m [e.g. *Lucas et al*., 2011; *Goodman et al*., 2012].

A comparison between cross-shelf gradients obtained using only the top 5m of the water column – simulating surface-only sampling studies – and cross-shelf gradients using the top 20m as reference for P_{bio} averages during M5 shows how inshore stations might artificially suggest significant increases in phytoplankton towards the coast (Figure 8a-b). Instead, Figure 8c shows that phytoplankton is often located in higher abundances in deeper, offshore portions of the water column. Overall, surface-only sampling underestimated and biased cross-shore estimations of P_{bio} during this mission. This misrepresentation of cross-shelf gradients is especially apparent in areas where cross-shelf transport of phytoplankton occurs along isopycnal surfaces that are often tilted with respect to the surface, reaching shallower depths in the innershelf portion of the sections (e.g. see sections #55-64 in movie).

4. Discussion

Changes in cross-shelf bio-optical properties are determined by physical and environmental factors that act together or independently to affect water column conditions over a wide range of time scales. A Conceptual Model for particle variability at this coastal site is provided in Appendix D for reference. Links between high frequency changes in P_{sed} and P_{bio} and potential physical forcings controlling their variability are discussed in sections 4.1 and 4.2. In section 4.3, examples of circumstances where co-variability between P_{sed} and P_{bio} is strong or weak are highlighted. Statistical connections between the EOF temporal

patterns, cross-shelf mean P_{bio} and P_{sed} changes throughout the missions, and potential physical forcings are listed on Table 2.

4.1 Controls on suspended sediment distribution

Significant wave height (Figure 4e) was the environmental quantity that best correlated with temporal changes in mean cross-shelf P_{sed} (r=0.49; Table 2). The largest increases in particle load were associated with above-average wave height conditions during M7 (r=0.81 with a 12-hour lag). This correspondence was especially apparent during the initial onset of the wave events, when increases in wave-induced orbital velocities, leading to re-suspension of particles, are likely to occur [*Clarke et al*., 1982]. When wave heights decreased, mean water column particle loads decreased more slowly with about a 12-hour lag, reflecting particle settling processes. In addition to actively stirring the water column, it is thought that moderate surface waves (height >2m, periods >10s) can produce combined wave-current bed shear stresses that exceed critical conditions for internal wave breaking in the California coast, inducing sediment re-suspension [*Bogucki et al.,* 1997; *Bogucki et al*. 2005; *Cheriton et al*., 2014]. This might also determine how and if particles are maintained in suspension after the waves decline [*Glenn et al.,* 2008].

Examples of changes in P_{sed} concentrations during the first 10 days of M7 are shown in Figure 9a. From the beginning of the storm on November 29, 2012, the primary response to increased wave conditions was an increase in the magnitude of the bottom nepheloid layer. BNLs grew and dominated the entire slope by December 01, when wave heights were also at their highest (Figure 4c). Following a decrease in wave height conditions, increased stratification favored the establishment of prominent INLs that only get eroded by December

7, as a new set of large waves is registered in the area. After this time, the water column returns to its pre-storm state, with BNLs dominating the vertical distribution of particles below the mixed layer until the end of the sampling period, December 14th (see Movie S1 for a complete view of these events). The transitions between BNL and INL-dominated water columns during M7 (and other missions as well) are also clearly depicted in AF2-P_{sed} patterns (Figure 6b).

No simple statistical relationships between tide height or phase and mean changes in particle load quantities in the water column were observed (Table 2). However, the potential local effect of tidal activity on the spatial distribution of P_{sed} is shown in Figure 9b, where consecutive glider sections within a 21-hour period of M8 are shown along with tide height at the time of each section. Low tide conditions show increased turbidity in shallow waters and allow for detached particle layers to reach further offshore along selected isopycnals, while particles during high tide periods appear confined to the bottom slope. In the deeper portions of the water column, however, rapid increases in particle concentrations are observed following abrupt changes in density, resembling the effect of a tidal bore interacting with near bottom materials [e.g. *Bogucki et al.*, 1997]. It is important to note that the sediment concentration changes on the order of a few grams per cubic meter are not sufficient to affect density gradients, which are on the order of a few kilograms per cubic meter. Similar spatial changes in P_{sed} distribution according to tidal conditions were observed during other missions as well, but depth-resolved current information would be necessary to appropriately decouple tidal effects from local current and shear effects.

Surface alongshore advection partially explained changes in the mean P_{sed} per section (r=-0.36), indicating not only that increases in the total amount of materials in the water

column were associated with westward flows, but also that advection played an important role renewing waters between glider sections, limiting interpretation of the patterns as continuous observations. Relationships between mean P_{sed} estimates per section and the cross-shore component of currents were weak (Table 2). This is not surprising since near-bottom particle loads should be primarily affected by the state of near-bottom currents, which in the mid-shelf may vary independently of the surface currents. Depth-resolved velocity data would be necessary to appropriately resolve these processes.

4.2 Controls on phytoplankton distribution

The role of physical drivers in determining overall temporal changes in cross-shelf mean P_{bio} was less clear than for P_{sed}, confirming that it is the combination of several ideal conditions that lead to increases in P_{bio} distribution and not a single factor. The lack of strong correlations between EOF temporal patterns and environmental quantities (Table 2) also illustrates how a two-dimensional analysis can miss important processes related to the along-shore advection of phytoplankton patches that account for apparent increases in phytoplankton abundances. Nonetheless, the relationship between AF1-P_{bio} (which resembles the cross-shelf mean P_{bio} observations), and mean temperature (Figure 4c), although not strong (r=-0.25), suggests a relationship between the arrival of cold, nutrient-rich waters, and elevated amounts of phytoplankton across the shelf. A weak but significant relationship with wind stress also supports the role of upwelling in accounting for P_{bio} increases across the shelf (r=-0.21). Alongshore velocities explained little of the variability in P_{bio}. However while the cross-shore component of surface currents did not account for changes in P_{sed}, it partially explained variability in P_{bio} (r=-0.32), although this

correspondence is driven exclusively by relationships during M6 and M9 (r=-0.42 during M6 and r=-0.30 during M9; correlation coefficients were not significant for the other missions). This suggests that higher concentrations of phytoplankton during those missions were associated with offshore flows near the surface, consistent with the cross-shore setup of upwelling fronts.

Unique connections between physical forcings and biological response were observed during M5, when a large phytoplankton bloom in the first half of the mission was accompanied by cooler water temperatures and weak wind conditions throughout (Figure 4c-d; winds were also weak before the mission's start). This potentially indicates that processes other than the classic upwelling of nutrients controlled P_{bio}. Internal waves and tides have been shown to deliver nutrients and larval particles from offshore locations to the shelf to support primary production and benthic communities when upwelling is absent [e.g. *Pineda and Lopez*, 2002; *McPhee-Shaw et al*., 2007]. Internal waves could have helped displace cold water and nutrients to shallower depths during M5, but the aliasing inherent in the cross-shelf sampling strategy did not allow clearly resolving their activity. Alternatively, mean cross-shelf phytoplankton biomass is compared to ζ / f to explore the hypothesis that the strengthening of the SBC eddy amplifies the connections between the innershelf and offshore waters by advecting nutrient-rich waters or phytoplankton into shallower regions (Figure 4h). Elevated P_{bio} estimates were associated with stronger stratification, and stronger cyclonic circulation (more common during summer and spring) of the SBC eddy than the observed when mean cross-shelf P_{bio} was low (Table 2). Surprisingly, changes in the values of ζ / f explain 53% of the variability in mean P_{bio} during M5. Daily averages of HFR surface currents for the SBC region for July 27th (when the first bloom was detected along the glider

sections) and August 5th (when P_{bio} estimates were low) superimposed on MODIS-Aqua chlorophyll satellite images for the same dates supports the role of surface currents in advecting materials into shallower regions (Appendix E).

Cross-shore gradients in P_{bio} (i.e. AF4-P_{bio}) help support the overall role of offshore-origin advection of nutrients and/or phytoplankton in accounting for productivity on the innershelf. Figure 9c (or sections #62 to 66 of Movie S1) constitutes an example where a P_{bio} patch near the end of M5 appears to propagate into the innershelf over a 19h period (equivalent to a cross-shore propagation speed of 3cm/s; see also Figure 8c). This is a unique observation that would have been missed by ship, mooring and satellite observations. Cross-shore surface currents and P_{bio} gradients (AF4- P_{bio}) showed a significant relationship during M5 (r=-0.32), indicating that the appearance of patches offshore was associated with advection of offshore waters towards the innershelf. However, the role of alongshore advection of patches non-parallel to shore in accounting for the apparent cross-shelf propagations cannot be discounted.

4.3 Co-variability between P_{sed} and P_{bio} over time and space

The lack of statistical correspondence between cross-shelf P_{bio} and P_{sed} means (r=-0.01) reinforces the observation that sediments and phytoplankton are likely controlled by different mechanisms across the shelf. On a mission-to-mission basis, however, relationships are often clearer. Cross-shelf mean values of P_{bio} and P_{sed} are inversely correlated during missions M5, M6 and M7 (r=-0.38, -0.18 and -0.52 respectively), while a positive correspondence is observed during missions M4, M8 and M9 (r=0.26, 0.39 and 0.60 respectively).

The lack of positive correlation between P_{bio} and P_{sed} during missions M5 and M6 is not surprising since the strong stratification conditions experienced at those times likely led to different portions of the water column, with fundamentally different particle types, to be controlled by different mechanisms. Locally, however, co-variability between P_{bio} and P_{sed} is often observed within surface nepheloid layers. In Figure 10a, daily averages of P_{bio} and P_{sed} during a week-long period during M6 highlight the concurrent advection of phytoplankton and other materials from shallower areas. It is possible that the advection of P_{sed} (perhaps dominated by organic matter and nutrients) partially fuelled increases in P_{bio} across the shelf. Nonetheless, the observation of an apparent splitting of the P_{bio} layer into a near-surface innershelf patch and a deeper, offshore layer, is unique, and opens discussion regarding the potential role of particle settling within the mixed layer in determining quick changes in the vertical distribution of P_{bio}.

Studies in the SBC have indeed related phytoplankton growth to inputs of nutrients from streams and re-suspension of nutrient-rich materials [e.g. *Otero and Siegel*, 2004]. Increases in P_{sed} during the precipitation event during December 2012 (M7) are largely attributed to increased discharge from the nearby Arroyo Burro Creek (Figure 1), although only precipitation data were available. However, increases in P_{bio} associated with this event were not observed within the time and space scales of the mission. The inverse relationship between P_{bio} and P_{sed} during the first half of the mission was expected, since optical properties were overwhelmingly dominated by the presence of suspended sediments. Intense sediment re-suspension events and intense mixing might also have resulted in light-limited conditions for phytoplankton growth. However, increased water column stability after the storm did not correspond with increased cross-shelf mean P_{bio} determinations (Figure 4e-f). It

is possible that blooms fueled by storm-related processes occurred after the mission was concluded or occurred away from the study area. Nonetheless, the observation that re-suspension and discharge did not positively affect phytoplankton distributions over short time scales is important because it suggests that local nearshore planktonic ecosystems might rely less on allochtonous nutrient inputs than previously considered. Alternatively, it might indicate an important role of turbidity in creating light-limiting conditions for phytoplankton production.

Potential links between processes that lead to sediment re-suspension and those that lead to increases in phytoplankton abundances were observed during the late winter to spring missions M4, M8 and M9. Excellent temporal co-variability is seen during the second half of M9, when phytoplankton blooms and sediment re-suspension events were not only intense, but their developments were remarkably synchronized (Figure 4e and 4h). These observations are in accordance with studies that report the co-occurrence of large phytoplankton blooms and suspended minerogenic materials as an inherent optical feature of the SBC [*Kostadinov et al*., 2012; *Antoine et al*., 2011]. Contrary to M7, increases in particle load during M9 occurred largely independent of wave conditions (see the short wave periods in Figure 4e). Instead, upwelling-favorable winds preceding the main sediment load event (see Figure 4d) likely favored the intrusion of an upwelling front, inducing mixing and re-suspension [*Lentz and Fewings*, 2012] and supporting increases in P_{bio} following possible nutrient advection. A 2.5-day gap in the glider data, however, prevented comprehensive observation of the water column evolution. Daily averages of P_{sed} and P_{bio} for the 5 days following the upwelling intrusion are shown in Figure 10b and illustrate how, despite simultaneous temporal increases in overall P_{bio} and P_{sed} loads and unlike M6, their cross-shelf

distributions did not overlap significantly over space. Phytoplankton remain well distributed in the top 20m of the water column, and minerogenic materials are generally constrained within bottom and intermediate nepheloid layers. Overall, these observations suggest that it is the combination of nutrient availability in the euphotic zone and significant mixing associated with upwelling-favorable conditions that allow for P_{bio} and P_{sed} to co-vary over time.

5. Future cross-shelf studies

The repeated cross-shore sampling in this study provided unique characterization of the changes in bio-optical properties over scales of ~3 hours to ~2 weeks. However, the passage of internal waves, diurnal cycles, vertical migration and short wind bursts (acting over much shorter time scales) resulted in aliasing of the patterns observed. Additionally, the lack of depth-resolved velocity information concurrent to glider observations limited interpretation of the effects of advection on physical and optical changes. Thus, future studies should consider using multiple gliders or similar depth-resolving instruments (e.g. wirewalkers; *Pinkel et al.* 2011) equipped with velocity meters in a control volume setting to decrease aliasing issues and account for changes due to alongshore advection, thus improving understanding of local versus global controls on bio-optical properties. Integrated approaches for ocean sampling such as RaDYO [*Dickey et al.*, 2012], and LEO [*Schofield et al*., 2002] have proven the importance of fully sampling processes that affect oceanographic properties. In this study, the availability of local meteorological stations measuring local wave conditions and cross-shore wind stresses, for instance, would certainly provide more

appropriate ways to relate quick changes in ocean conditions to changes in bio-optical properties. Likewise, the ability to differentiate species composition and size would be invaluable for future determinations of cross-shore transport and export of organic matter. For instance, discrete water samples collected by SCCOOS (http://www.sccoos.org/data/habs/) at a location 3.6-km away from the glider site provided evidence that the two larger blooms sampled during M5 might have been dominated by different phytoplankton groups, namely diatoms and dinoflagellates. In the future, high-frequency sampling of species composition will allow determining if different species are preferably advected from the nearshore or offshore waters at different times, with important implications for cross-shore transport and understanding of drivers of coastal productivity.

6. Conclusions

The data presented here provide for the first time a highly resolved in time, 2-D view of the physical and optical oceanographic properties of the coastal Santa Barbara Channel. Waves were found as a proximate control on suspended sediment variability for both inner and mid-shelves, while episodic increases in phytoplankton abundances were attributed to advection and upwelling events. Decoupling bio-optical signals from their controlling processes in coastal zones is challenging. In the SBC, nearshore and offshore phytoplankton, detritus and suspended sediments often occupy the same portion of the water column, but different physical forcings control their temporal distribution. Furthermore, these same forcings interact with each other over different time and space scales in non-predictable ways. Nonetheless, high-frequency glider observations provided a unique view on particle

distributions in shallow areas and showed the importance of obtaining depth-resolved information of physical and bio-optical quantities to properly resolve bio-physical interactions in productive regions.

Tables and Figures

Table 1: Overview of glider missions.

Mission	Start-End Dates	Days of good data [total]*	No. of sections	Mission Characteristics
M4	Mar 7 – Mar 14 2012	6 [8]	18	Mixed + Upwelling
M5	Jul 27 – Aug 12 2012	18	58	Strongly strat.; Large bloom
M6	Sep 9 – Sep 27 2012	19	92	Stratified
M7	Nov 27 – Dec 14 2012	17	85	Mixed + storm
M8	Feb 5 – Feb 17 2013	13	64	Weakly stratified
M9*	May 22 – June 16 2013	19 [21]	87	Stratified + Upwelling; bloom
Total		92	404	

* A 1.5-day data gap in M4 and a 2.5-day data gap during M9 occurred. Also during M9, only downcast data was recorded, which explains the longer than average mission length.

Table 2: Correlation coefficients between P_{bio}, P_{sed}, Amplitude Functions and physical forcings. These are overall relationships. Mission-specific correlations are shown in text, when necessary. Bold values are discussed in text. Alongshore velocities are denoted by U, cross-shore velocities by V. B53 = NDBC 46053; B54 = NDBC 46054.

	% expl var	Interpretation	*Psed (mg/m3)*	*Pbio (mg/m3)*	*Tau (B53; Pa)*	*Tau (B54; Pa)*	*Wind speed U (B53; m/s)*	*Wind speed U (B54; m/s)*	*rain (mm/3h)*	*V/f*	*SWH (m)*	*glider U (m/s)*	*glider V (m/s)*	*radar U (m/s)*	*radar V (m/s)*	*T (oC)*	*Chl max (m)*	*MLD (m)*	*Tide (m)*
Psed		Mean *Psed*		n.s.	n.s.	0.10	n.s.	-0.17	0.28	0.23	**0.49**	-0.12	-0.29	**-0.36**	n.s.	0.25	-0.35	0.22	0.11
Pbio		Mean *Pbio*	n.s.		n.s.	-0.21	n.s.	0.19	-0.12	**0.43**	-0.25	n.s.	-0.14	0.12	**-0.32**	-0.10	n.s.	-0.38	n.s.
AF1-Psed	62.7	Particle load	**0.99**	n.s.	n.s.	0.14	n.s.	-0.20	0.30	0.21	0.47	-0.12	-0.27	-0.37	n.s.	0.29	-0.31	0.25	n.s.
AF2-Psed	10.7	Vertical structure	n.s.	-0.23	0.23	0.29	-0.22	**-0.30**	0.13	n.s.	n.s.	n.s.	0.10	n.s.	0.18	n.s.	n.s.	**0.42**	n.s.
AF3-Psed	4.4	Episodic events	n.s.	n.s.	0.15	n.s.	-0.19	n.s.	n.s.	n.s.	-0.16	n.s.	n.s.	n.s.	n.s.	n.s.	n.s.	n.s.	n.s.
AF1-Pbio	50.6	Phyto biomass	n.s.	**0.93**	n.s.	-0.18	n.s.	0.15	-0.12	0.39	-0.19	n.s.	-0.11	0.15	-0.24	**-0.25**	-0.12	-0.34	n.s.
AF2-Pbio	12.1	Chl max	-0.21	n.s.	n.s.	n.s.	n.s.	n.s.	n.s.	-0.13	-0.13	n.s.	n.s.	0.18	0.13	0.22	**0.56**	-0.26	0.14
AF3-Pbio	7.4	Vertical shape	n.s.	0.33	n.s.	-0.14	0.12	0.17	n.s.	0.11	-0.18	n.s.	n.s.	n.s.	-0.17	0.16	0.23	-0.11	n.s.
AF4-Pbio	5.7	Cross-shelf grad	-0.23	n.s.	n.s.	n.s.	n.s.	n.s.	n.s.	n.s.	n.s.	n.s.	n.s.	n.s.	-0.15	n.s.	0.15	n.s.	n.s.

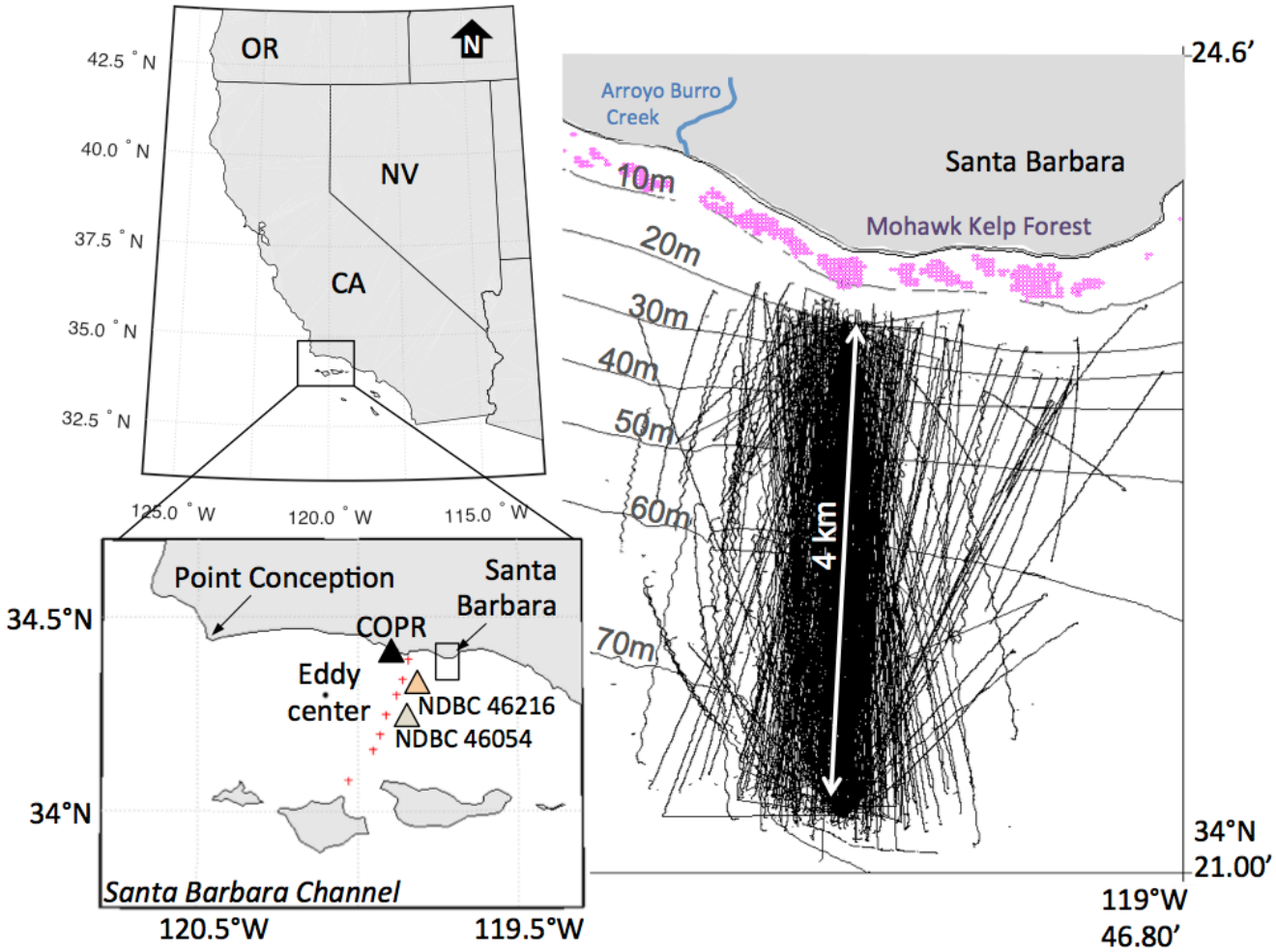

Figure 1. Map of study area. Glider paths and location of main data sources used in this study are highlighted: NDBC buoys 46053 and 46216, Coal Oil Point meteorological station (COPR), Plumes and Blooms stations (red crosses), eddy center, and average extent of the nearby kelp forest as derived from long-term Landsat imagery [*Bell et al*., 2015]. The white 4-km long arrow marks the limits of the final mapped sections bounded by the latitudes 34.3901N and 34.3551N.

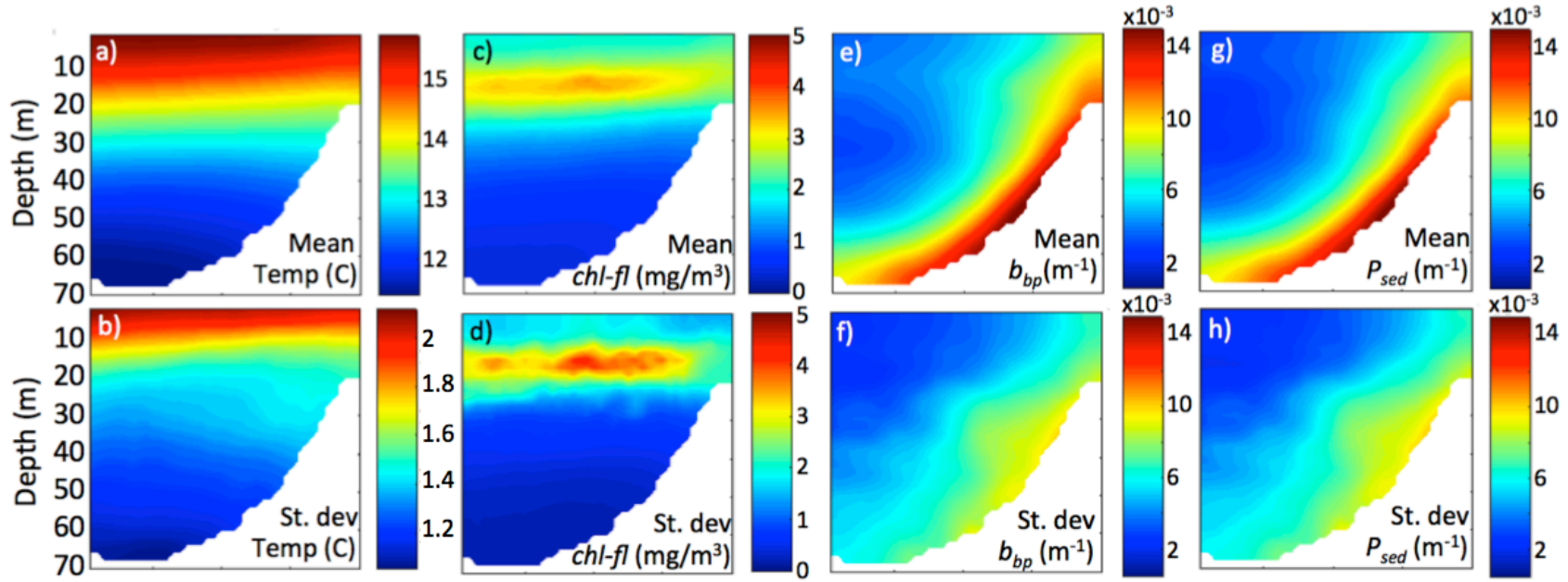

Figure 2. Section means and variability (standard deviations) of physical and bio-optical properties. (a-b) Temperature, (c-d) *chl-fl,* (e-f) $b_{bp}650$, (g-h) P_{sed}. Means and standard deviations are taken over all missions (n=404). Units of P_{sed} are shown as inverse meters to allow direct comparison with b_{bp} distributions. Throughout the analysis, however, P_{sed} was presented in TSM units (see Section 2.2).

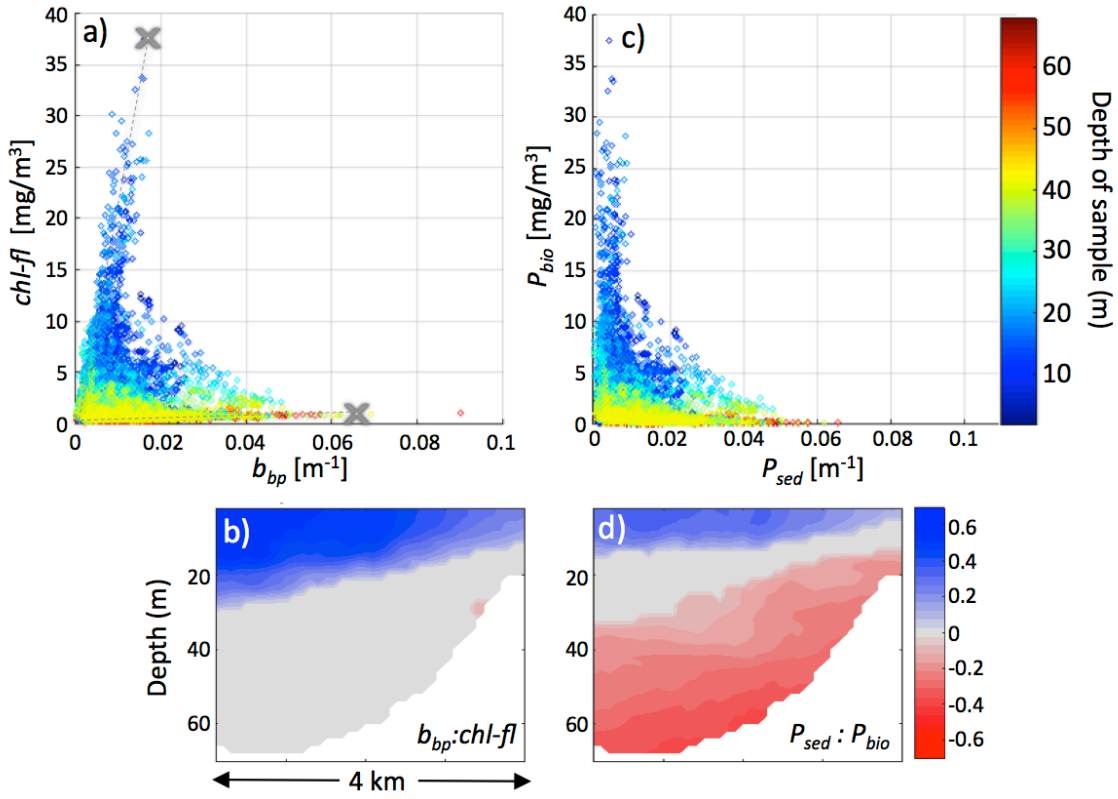

Figure 3. Co-variability between b_{bp} and *chl*-fl and transformation into P_{bio} and P_{sed}. (a) Relationship between b_{bp} and *chl-fl*. Colorbar indicates the depth of origin of each sample; (b) Spatial correlation map between b_{bp} and *chl-fl* (grey values are non-significant); (c) Result of linear transformation between b_{bp} and *chl-fl* using the endmember vectors represented by the grey "x" on a); (d) Spatial correlation map between P_{bio} and P_{sed} values. Only a small subset of datapoints (7.5%) is used in top panel scatterplots to allow clearer visualization.

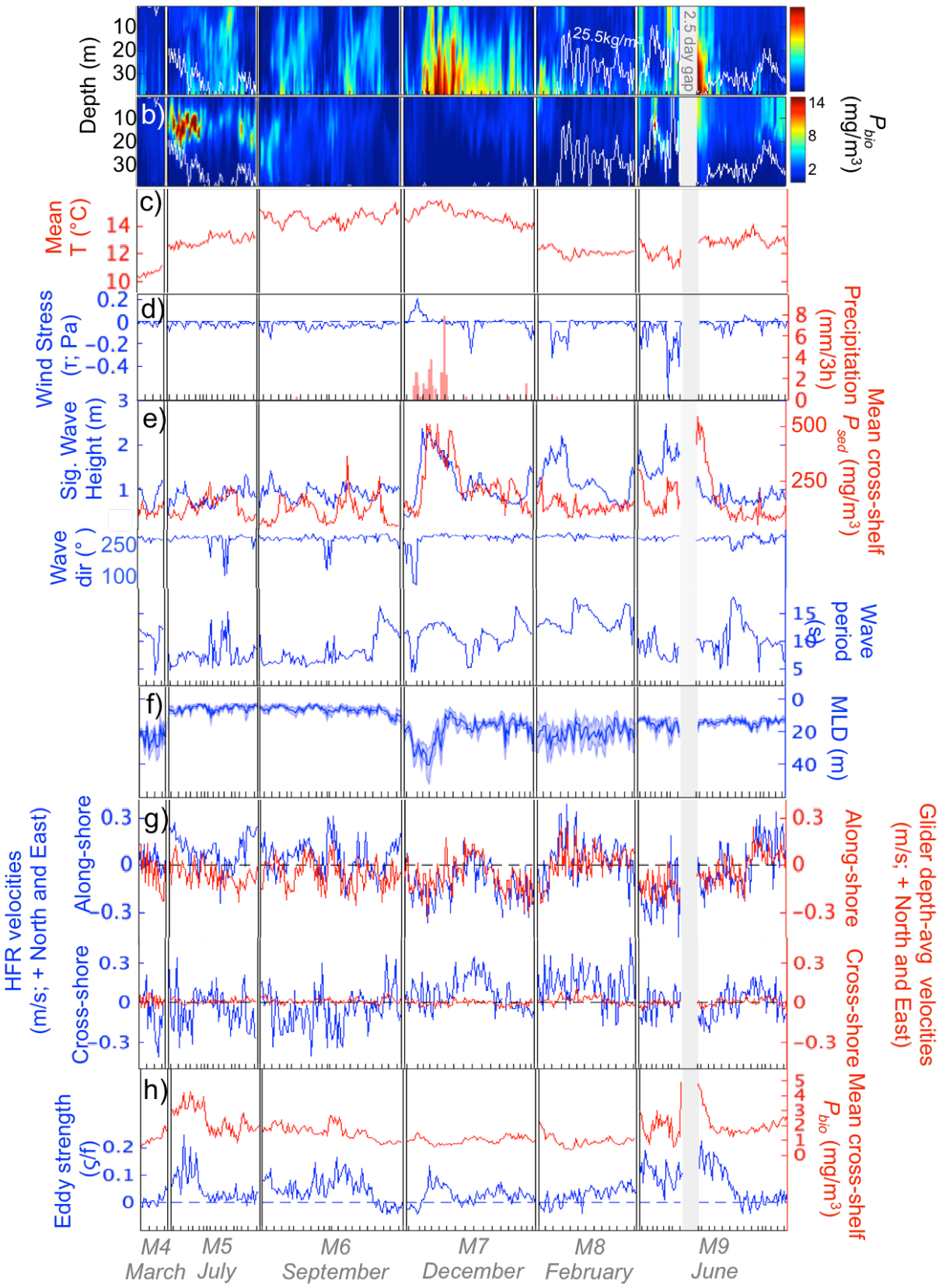
Depth (m)
10
20
30
25.5kg/m³
2.5 day gap
b)
14
8
2
P_bio (mg/m³)
c)
Mean T (°C)
14
12
10
d)
Wind Stress (τ; Pa)
0.2
0
−0.2
−0.4
Precipitation (mm/3h)
8
6
4
2
0
e)
Sig. Wave Height (m)
3
2
1
Mean cross-shelf P_sed (mg/m³)
500
250
Wave dir (°)
250
100
Wave period (s)
15
10
5
f)
MLD (m)
0
20
40
HFR velocities (m/s; + North and East)
g)
Along-shore
0.3
0
−0.3
Cross-shore
0.3
0
−0.3
Along-shore
Cross-shore
Glider depth-avg velocities (m/s; + North and East)
h)
Eddy strength (ζ/f)
0.2
0.1
0
Mean cross-shelf P_bio (mg/m³)
M4 March
M5 July
M6 September
M7 December
M8 February
M9 June

Figure 4: **Time-series of optical and environmental properties throughout the missions**. All missions are concatenated into one time-series, and temporal gaps between missions are omitted. Tick marks are presented in one day increments for convenience (a) time-depth evolution of P_{sed} and (b) P_{bio} at the 40m isobath. White contours are the depth of the 25.5kg/m^3 potential density estimates. The location of the 40m isobath in context to the cross-shelf section is shown in Figure 9c; (c) Section-mean glider-derived temperature estimates per section; (d) Wind stress from NDBC 46053 and accumulated precipitation from COPR; (e) Significant wave height, wave period and wave direction from NDBC 46216 along with mean cross-shelf P_{sed} estimates; (f) Mean and mixed-layer depth variability across the shelf; (g) Surface HFR currents (blue) and glider depth-averaged currents (red); (h) Eddy strength from HFR data and mean cross-shelf P_{bio} estimates. Environmental data were assembled as 3 hour averages around the mean timestamp of each glider section to allow direct comparison. The relationship between these environmental forcings and mean changes in particle distribution across the shelf are shown in Table 2.

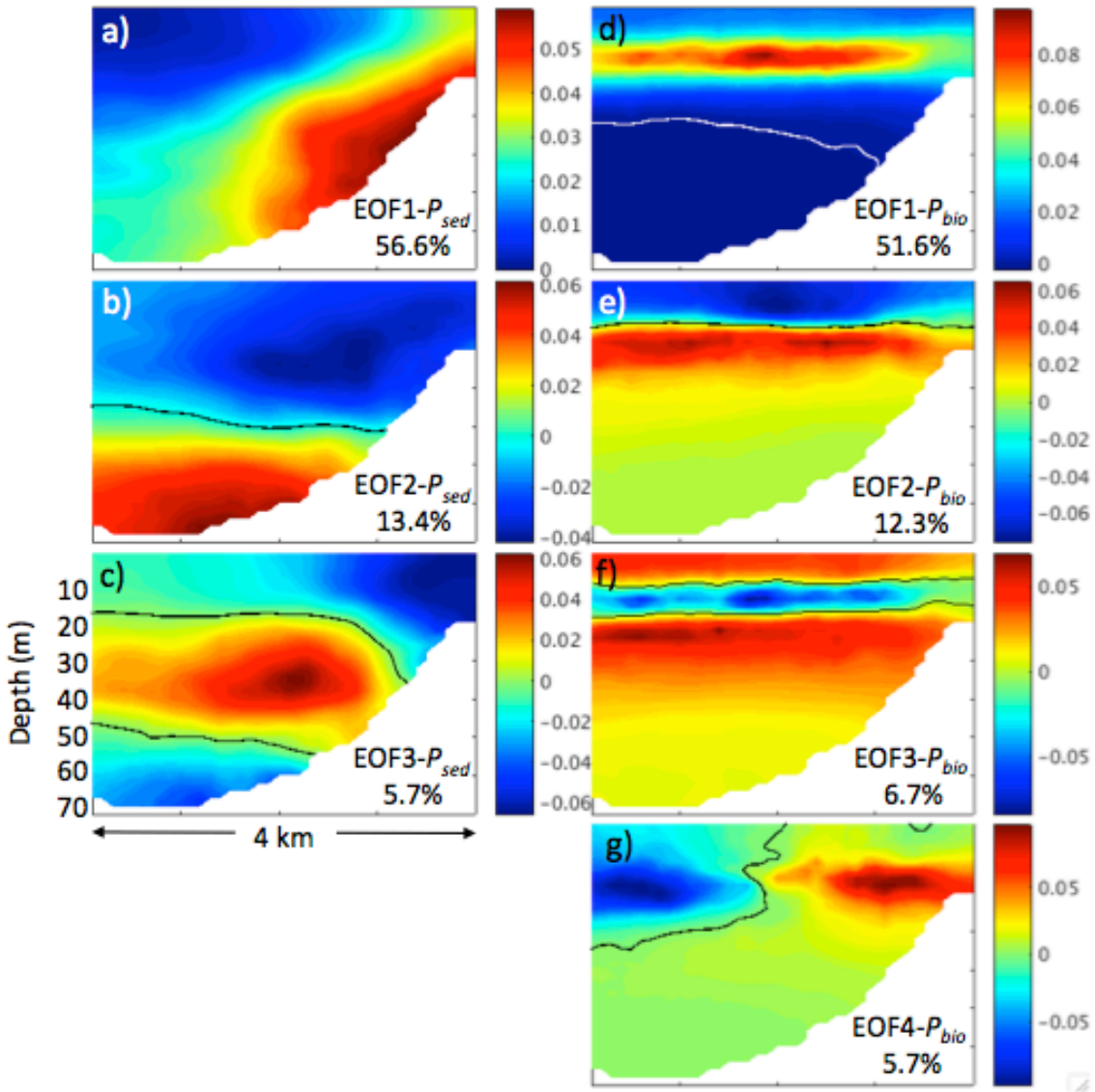

Figure 5: Dominant Empirical Orthogonal Function maps for (a-c) P_{sed} and (d-g) P_{bio}. The percent of explained variance per mode is shown along with each EOF. Contour line refers to the zero-crossing region where EOF signs flip.

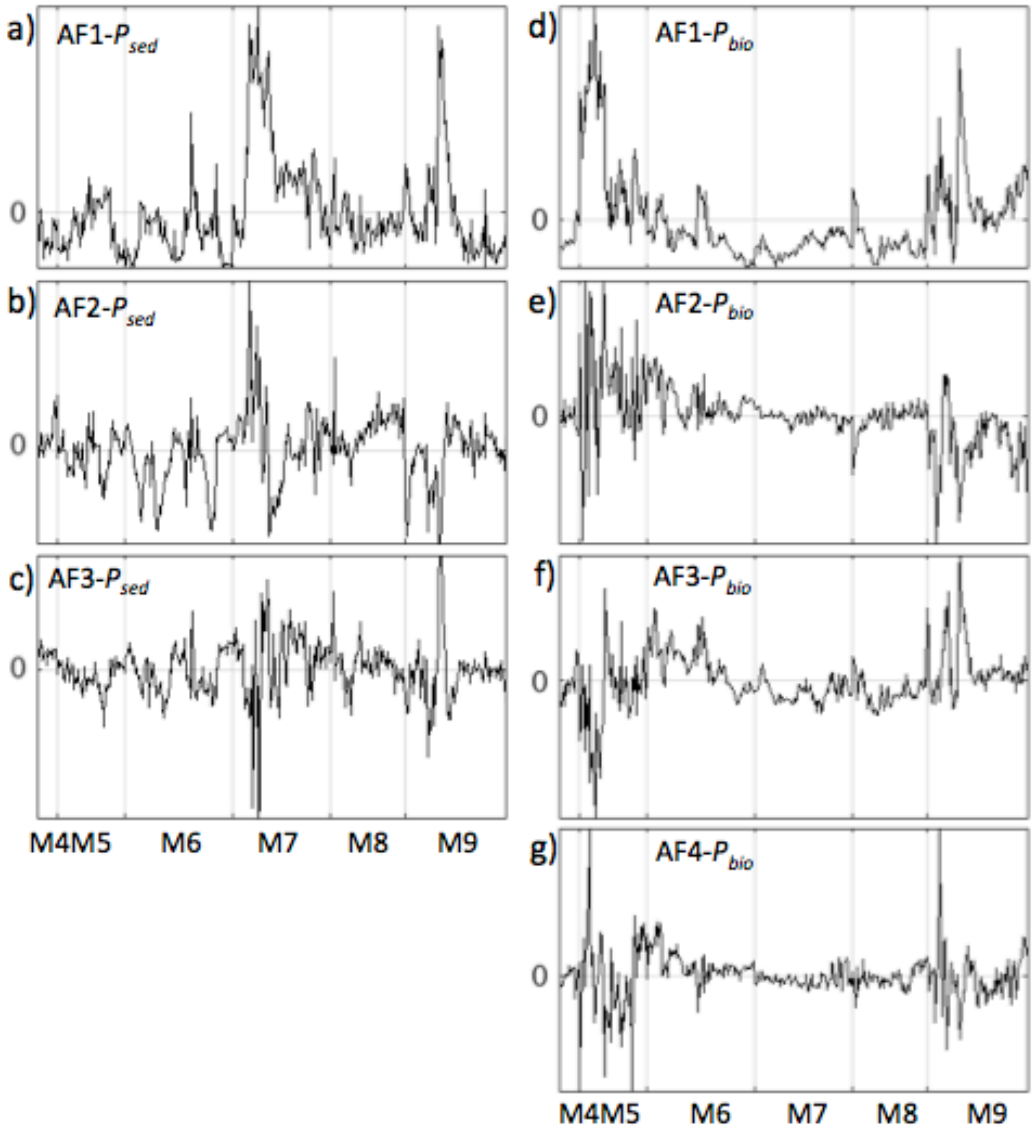

Figure 6. Amplitude Functions for (a-c) P_{sed} and (d-g) P_{bio} for the dominant EOF modes (as in Figure 5). All missions were concatenated in one time series, and gaps between missions are omitted. The zero-crossing mark is highlighted.

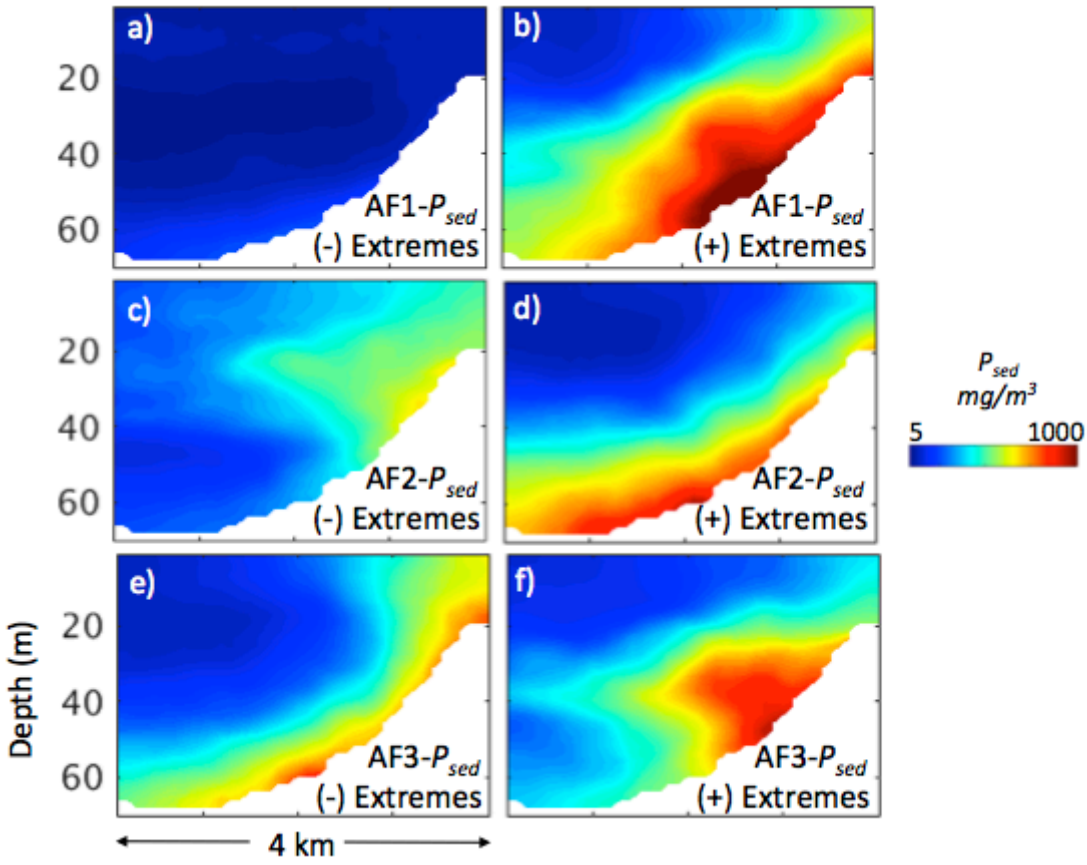

Figure 7. Mean P_{sed} estimates during the 15 extreme negative (left panels) and 15 extreme positive (right panels) EOF-P_{sed} values for each of the three dominant modes.

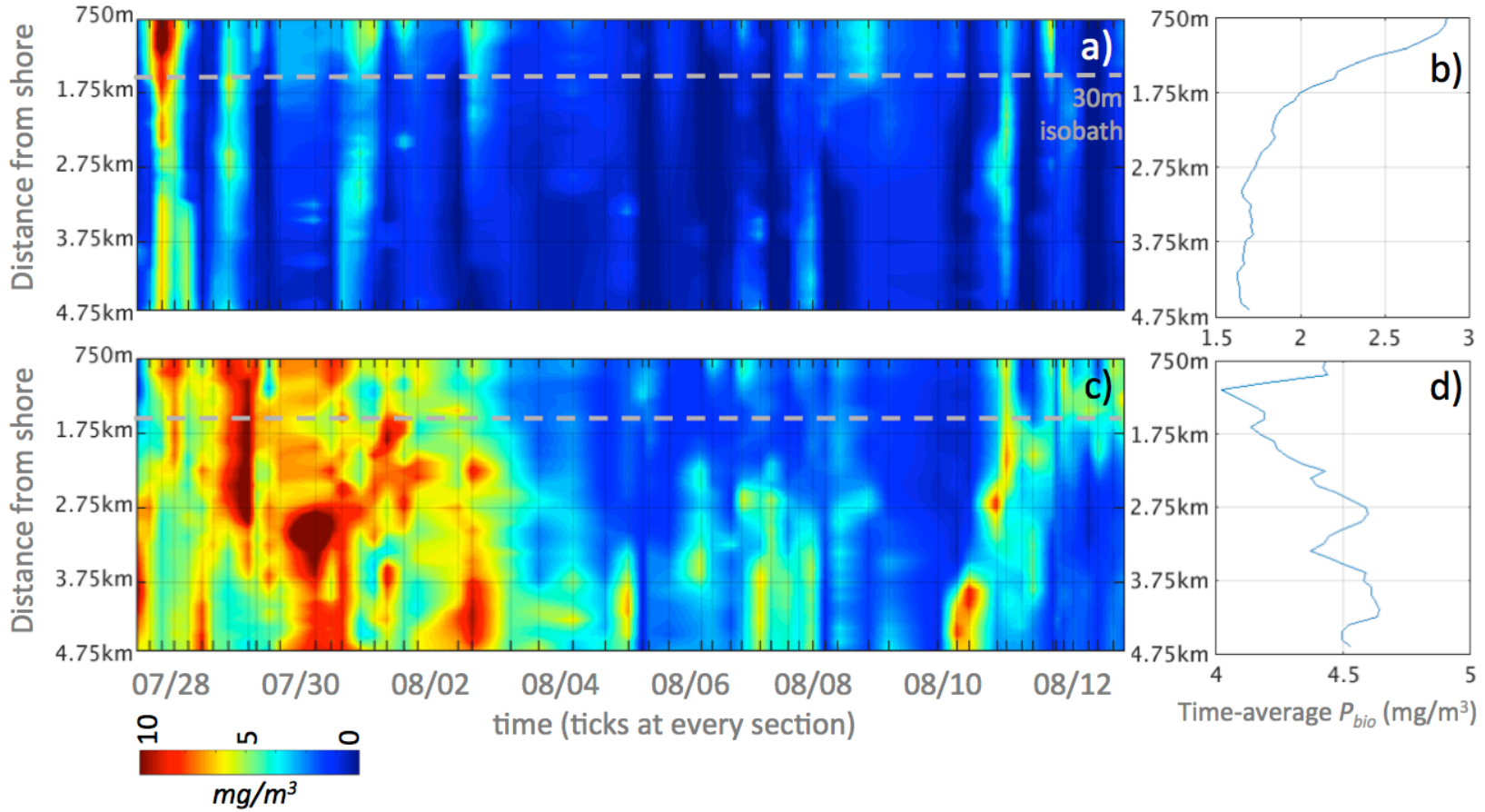

Figure 8. Cross-shelf P_{bio} distributions during the M5 mission (July 2012) showing how a surface-sampling perspective underestimates and biases cross-shelf estimations of phytoplankton. (a) Time – latitude (cross-shelf extent) P_{bio} distributions averaged over the top 5m of the water column; (b) Integrated P_{bio} estimates in (a) over time. (c) Time-cross-shelf P_{bio} distributions averaged over the top 20m of the water column. (d) Integrated P_{bio} estimates in (c) over time. The location of the 30m isobath, marking the offshore limit of the innershelf, is highlighted.

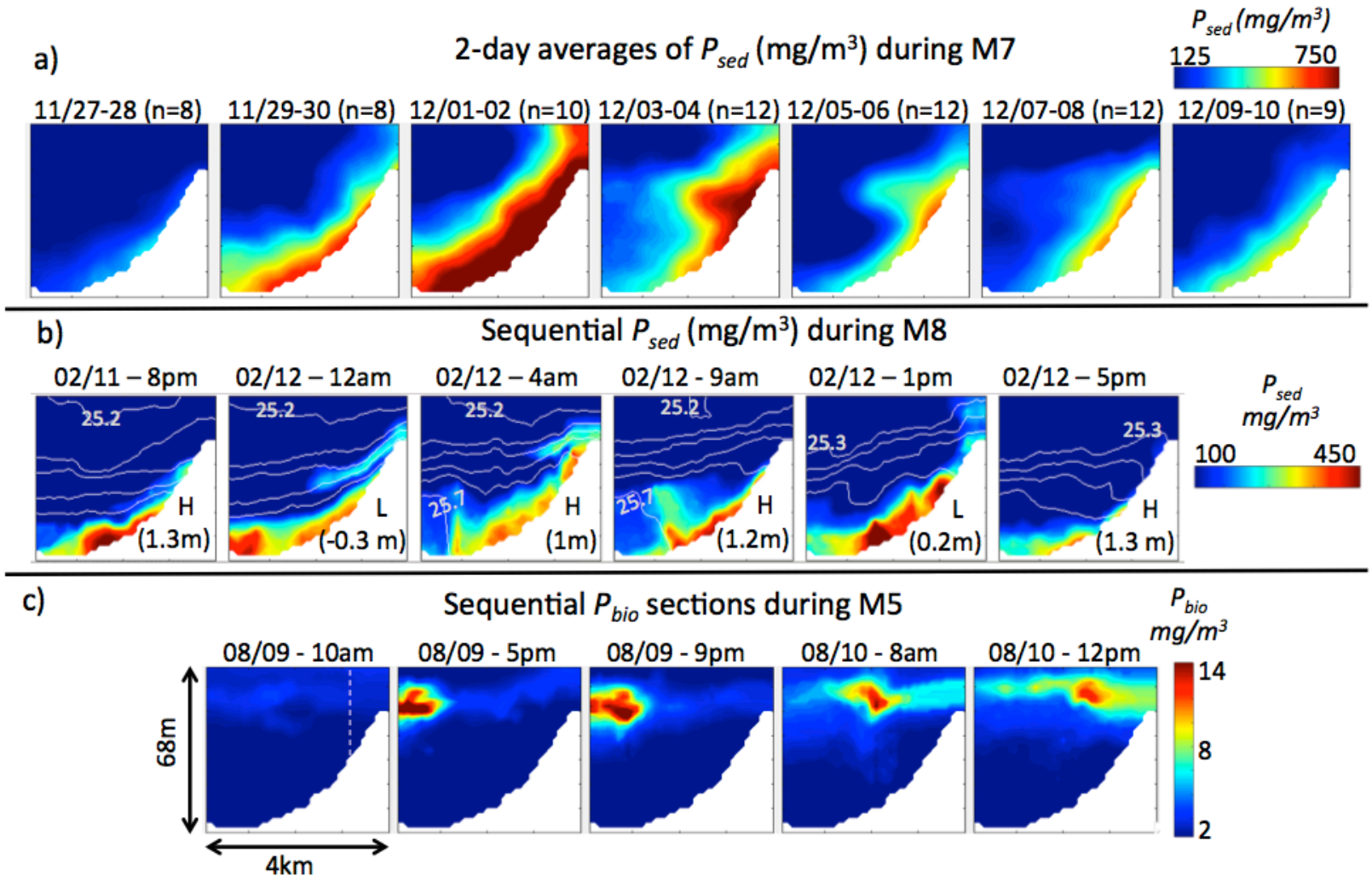

Figure 9. Examples of high-frequency changes in P_{sed} and P_{bio}. (a) 2-day averages of P_{sed} during the first portion of M7 (n=number of sections used in the averaging process); (b) A series of P_{sed} sections during M8 and the respective tidal height at the time of each plot (H = high tide; L = low tide). White contours of potential density are shown in 0.1kg/m^3 increments; (c) A series of P_{bio} sections during a M5 bloom. The white vertical dotted line on panel c refers to the 40m isobath used in Figure 4a-b. The mean time/date of each section is shown over each plot.

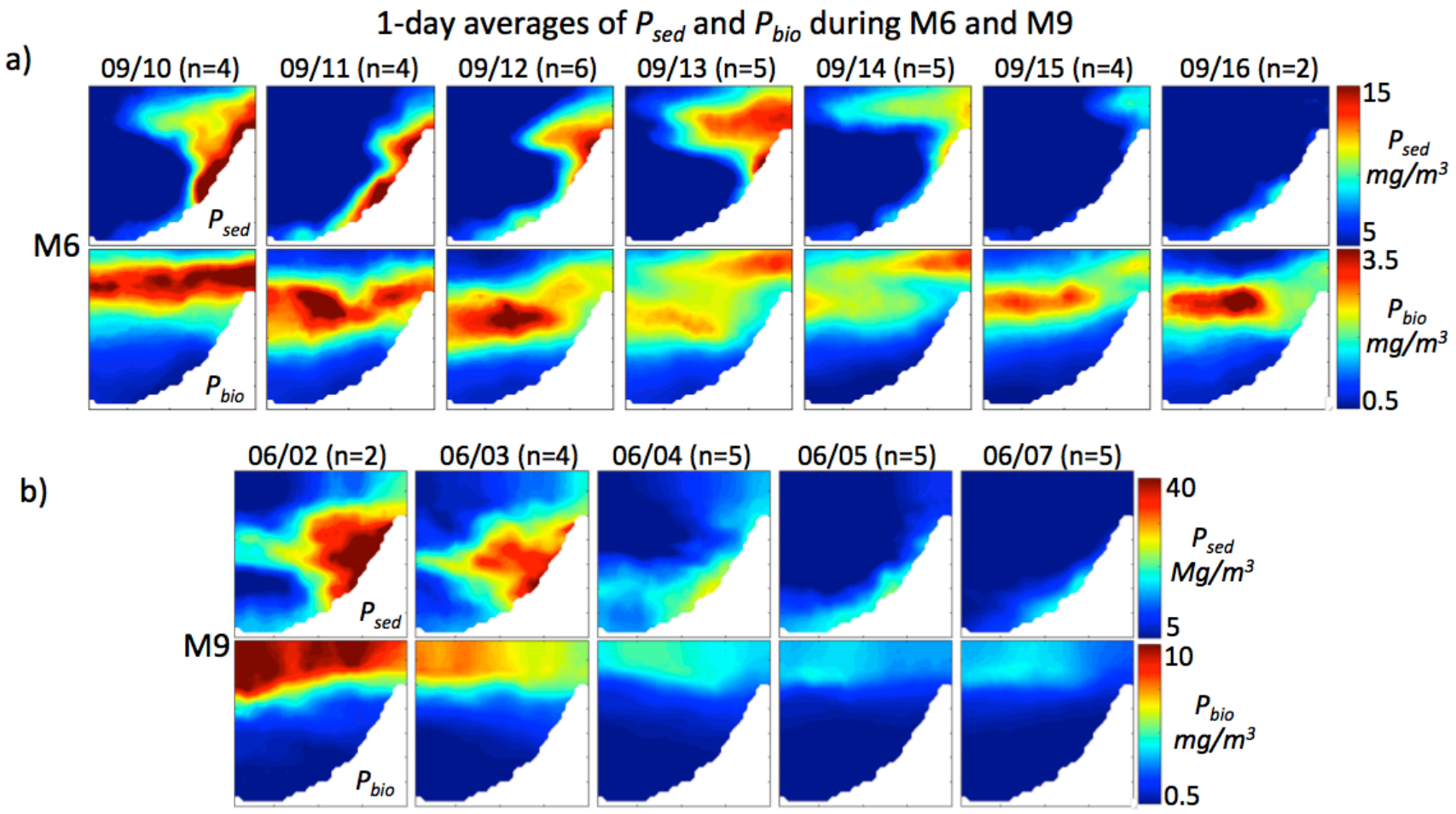

Figure 10. Examples of the space-time co-variability between P_{bio} and P_{sed}. (a) Daily averages of P_{sed} and P_{bio} during a portion of M6; (b) Daily averages of P_{sed} and P_{bio} during a portion of M9. Mean times and number of sections used in the averaging process are shown above each figure. Note that Colorbar scales are different for the different missions.

APPENDICES

APPENDIX A

The MOVIE (Movie_S1.mov in http://people.eri.ucsb.edu/~fernanda/GLIDER_MOVIE/) shows the time-space evolution of the bio-optical features observed in each of the 404 krigged sections of temperature, P_{bio} and P_{sed}. Occasionally, very short sections were included in the analysis to guarantee temporal continuity, which resulted in extrapolation of glider data to large areas of the section during the krigging process. However, these extrapolations did not affect the results negatively. Removing those sections in the EOF analysis yielded virtually identical results. Dragging the .mov file into powerpoint is an one easy way to step through each frame.

APPENDIX B

The figure below characterizes NPQ for each mission. In order to determine if/when NPQ occurred, near-noon profiles were tested with the following equation: NPQ = chl(noon) / [2*_chl_(evening)+_chl_(morning)], where chl(noon) was chosen as a *chl-fl* section with mean timestamp around noon (+/- 1.5 hours); *chl*(evening) as section timestamp 18:00 +/- 1.5 hours; and *chl*(morning) as section timestamp 6:00 +/- 1.5 hours. If *chl*(noon), *chl*(evening) and *chl*(morning) did not conform to these time guidelines NPQ was not calculated. NPQ values >1 indicate that NPQ did not occur, and NPQ values <1 indicate that NPQ did occur. Only a small percentage of sections per mission satisfied the criteria for NPQ calculation: for M4: 1% of sections; M5: 26% of sections; M6: 20% of sections; M7: 14% of sections; M8: 17% of sections; M9: 20% of sections. Thus, even if a large reduction in *chl-fl* values near the surface seems important and significant, it only affected a small portion of the sections. Figure shows:

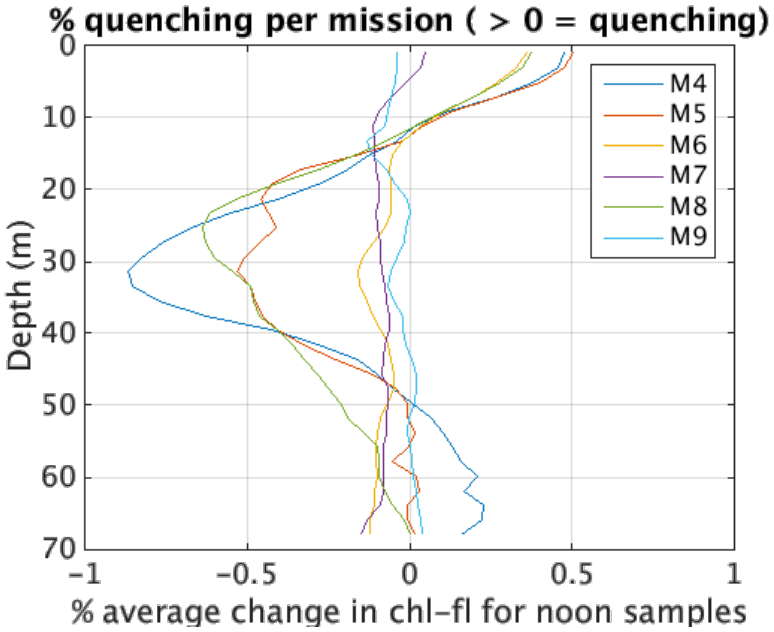

Figure B. Mean % NPQ in noon profiles during each mission. Positive values near the surface indicate NPQ (1 = 100% NPQ). Positive values further down in the water column are due to other processes such as advection.

APPENDIX C

Table C shows the results using the two-tailed Wilcoxon-Mann-Whitney test similarity analysis between the 15 extreme negative and 15 positive EOF loadings for each variable (Pbio and Psed). The positive and negative extreme loadings are significantly different from each other for all EOFs except for EOF2-Pbio.

Table C. Mean Psed and Pbio values for the 15 positive and negative extremes of the dominant principal components of P_{sed} and P_{bio} , respectively, with the correspondent two-tailed Wilcoxon-Mann-Whitney test results. AF2- P_{sed} and AF4- P_{bio} show no significant difference between extremes, which is expected since their spatial EOF patterns simply denote that different parts of the water column, at times, have the greatest amounts of materials. N= 15 for each parameter.

	Psed (mg/m3)			*Pbio (mg/m3)*			
	AF1	*AF2*	*AF3*	*AF1*	*AF2*	*AF3*	*AF4*
mean neg extremes	46	296	305	0.6492	2.9465	3.2513	2.8431
mean pos extremes	465	338	374	3.8368	2.7462	3.1485	2.6554
p-value	0.0000	0.5307	0.0000	0.0000	0.0043	0.0000	0.0984

APPENDIX D

Conceptual model for particle variability and the main forcings that drive cross-shelf changes in particle distribution.

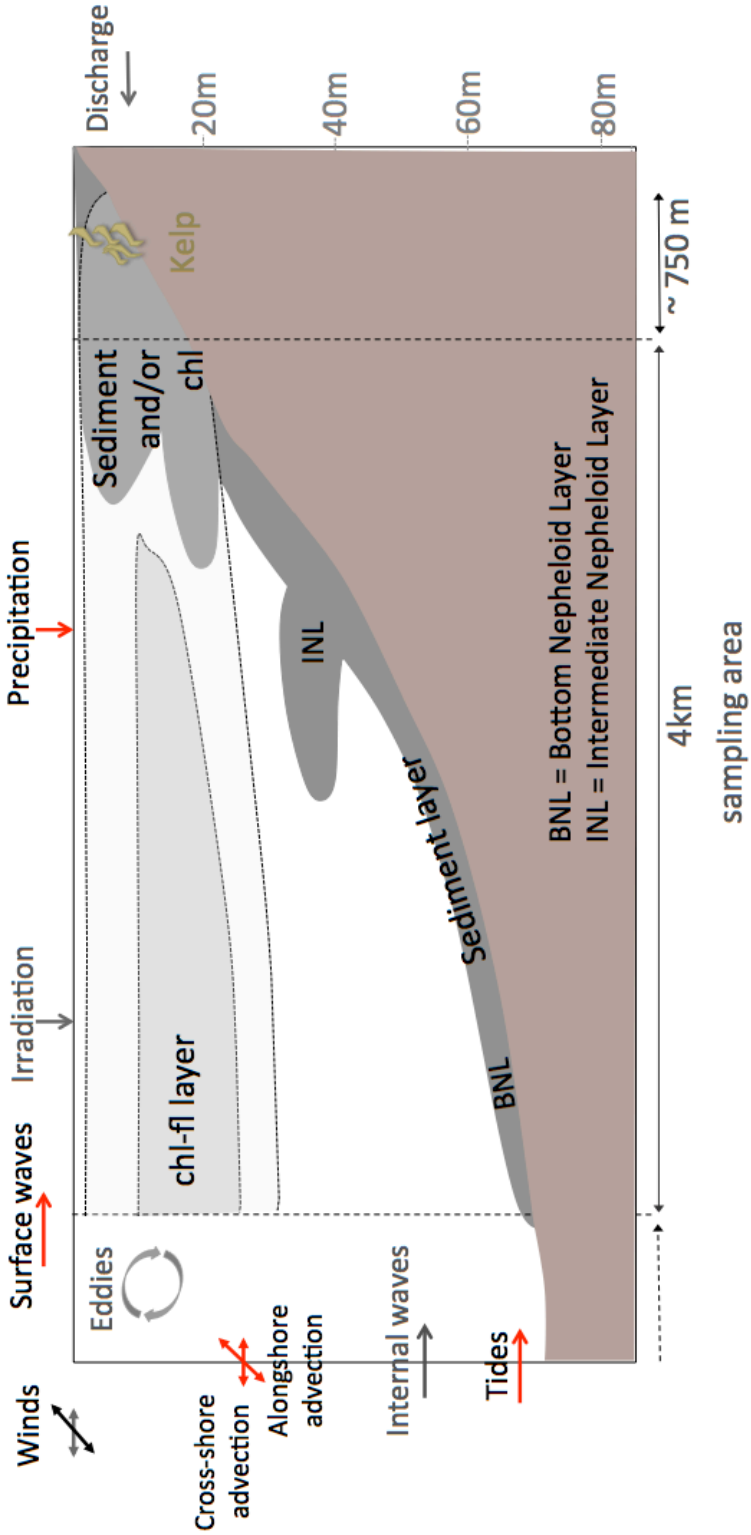

APPENDIX E

Figure E shows the large scale patterns of surface currents and satellite chlorophyll fluorescence estimates during two dates in M5. Satellite Images are Level-2 MODIS-Aqua chl-fl data obtained from http://oceancolor.gsfc.nasa.gov/cgi/browse.pl?sen=am. HF Radar hourly data are obtained from http://hfrnet.ucsd.edu/threadds/HFRADAR_USWC_hourly_RTV.html, daily averages are constructed around the time of each satellite image. This supports the connection between eddy strength in the channel and increases in phytoplankton presence in the innershelf.

Figure E (below). HFR and Aqua Modis chl-fl for 2 dates during M5.

MODIS Aqua imagery and
Daily means HF Radar surface currents
Jul 27
Study area
0.3 m/s
Aug 5
clouds
[mg/m³ chl]
5
4
3
2
1
0

CHAPTER 2

Transport and Fate of Phytoplankton, Suspended Particles & Dissolved Oxygen in the Nearshore Santa Barbara Channel, California

Abstract

Chapter One of this dissertation provided a large summary of the patterns and processes sampled by the underwater glider, and interesting connections between bio-optical variability in the water column and physical process acting over several space scales were found. In this chapter, the capabilities of the dataset are further explored to ask questions that are in the very core of the studies in upwelling environments: How important is the cross-shelf exchange of materials to the health of nearshore ecosystems? Is the nearshore zone a source or a sink for particles/heat/salt? Is the nearshore zone net autotrophic or net heterotrophic? And, do source/sink patterns change over time? Physical and bio-optical data from the coastal Santa Barbara Channel and velocity data from the Mohawk Kelp Forest mooring are used to calculate heat, salt, phytoplankton, oxygen and sediment material fluxes across this shallow productive zone. Reynolds decomposition is used to separate the mean and time-varying components of fluxes, allowing observation of, among others: the heterotrophic conditions of the nearshore zone during summer months; the offshore export of sediment particles by surface and intermediate nepheloid layers; and the weak net transport of sediments during weakly stratified periods despite high suspended sediment concentrations. The analysis provides important insights into future experiments that can be designed to characterize and further understand the cross-shore balances in community production.

1. Introduction

The inner portion of the continental shelf is a dispersal corridor between intertidal and offshore habitats [*Garland et al.*, 2002] that often hosts very high diversity of marine species [*Graham et al.*, 2007]. Although the innershelf is often characterized as the region where bottom and surface boundary layers together occupy the entire water column (roughly from the surf zone to about 30 m depth; *Lentz and Fewings*, 2012), strong stratification conditions often decouple boundary layers and allow cross-shelf flows in these shallow areas to display mid-shelf dynamics [*Cudaback et al.*, 2005; *Fewings et al.,* 2015]. Contrary to open ocean dynamics, cross-shelf circulation in the innershelf is not primarily driven by geostrophic flows. Instead, circulation is driven by along and cross-shore winds, surface gravity waves, tides and buoyant plumes [*Lentz and Fewings*, 2012]. Thus, physical processes such as wind-driven upwelling and downwelling, thermal fronts, eddies, tides, internal waves, tidal bores, surface waves, and storms, which operate over various time and space scales, are key to the distribution and variability of heat, salt, nutrients, oxygen, larvae, pollutants and particles in coastal ecosystems [*Nittrouer and Wright*, 1994].

The innershelf Santa Barbara Channel (SBC), in the Southern California Bight, is an ecologically productive and diverse coastal environment, lined with kelp forests that support a wide variety of benthic and pelagic ecosystems [*Mann and Lazier*, 1991; *Graham et al.*, 2007]. Circulation inshore of the 15m isobath displays innershelf characteristics about 50% of the time, and mean depth-averaged alongshore flow is poleward throughout the year, consistent with a cyclonic recirculation of the flow within the SBC and poleward pressure gradients during equatorward wind stresses [*Fewings et al.*, 2015]. Mean cross-shore

circulations show a C-shaped form, with a tendency for offshore flow near the surface and bottom and onshore flow in the middle of the water column [*Fewings et al.*, 2015]. This is consistent with a response to cross-shore and alongshore wind stresses during upwelling-favorable conditions. Although mean cross-shore flows in the region are generally weak (~1 cm/s), they do not imply weak transport [*Fewings et al.*, 2015]. The estimated flushing time onshore of the 15m isobath is 0.5-2 days, indicating that transport is not necessarily related to mean velocity [*Fewings et al.*, 2015]. Thus, depending on the vertical distribution of heat, salt, nutrients, oxygen, larvae, pollutants, sediment and phytoplankton in the water column, the cross-shelf circulation patterns will determine the quality and quantity of water properties and materials delivered to and from the shallower regions [*Nittrouer and Wright*, 1994].

Understanding the transport of these various properties across coastal zones is critical to assess what drives productivity and sustains the health of important coastal ecosystems. It is not known, for instance, whether the innershelf SBC is a source or a sink for salt/heat/particles, and if these patterns change throughout the year or on much shorter time scales (e.g., due to wind events, diurnal forcing, tides), or how important the mean flow is in transporting materials across the shelf, in contrast with time varying changes in flow. Furthermore, it is not clear when/if the innershelf is net autotrophic or net heterotrophic over different time scales. Questions regarding net-autotrophy have been the subject of considerable controversy in the past few years for the open ocean [e.g. *Ducklow and Doney*, 2013; *Duarte et al.*, 2013; *Williams et al.*, 2013], and although the importance of oxygen and carbon budgets in coastal environments is widely recognized [e.g. *Cai*, 2011], regional patterns are just as inconclusive. Changes in oxygen concentrations in upwelling systems over the past few years and decades have been the focus of many studies that aim to

understand the impact of decadal variability and climate change on benthic and pelagic ecosystems [*Bograd et al.*, 2008; *Chan et al.*, 2008; *Frieder et al*., 2012; *Booth et al*., 2014]. In these regions, oxygen-poor waters often get advected into productive continental shelves where respiration further reduces dissolved oxygen concentrations, subjecting coastal ecosystems to hypoxic conditions [*Chan et a*l., 2008].

Here, depth-resolved glider measurements of temperature, salinity, density, dissolved oxygen, chlorophyll-fluorescence and optical backscatter provide the biogeochemical state of the innershelf SBC, just outside the Mohawk Kelp Forest, over various stratification conditions. Acoustic Doppler Current Profile data from a mooring located near the glider observations (maintained by the SBC Long-Term Ecological Research program) provides the depth-resolved velocity measurements necessary for transport and flux calculations (armed with important assumptions such as the definition of a control volume inshore of the 10m isobath even though data was not collected within a control volume, and alongshore homogeneity), with important implications to the nearshore ecosystems. This chapter is intended as an exploration exercise to test the feasibility of gliders in extracting cross-shelf fluxes of important biogeochemical properties, with the goal of inspiring future cross-shore flux experiments.

Background on flux calculations

In cross-shore studies, cross-shore *Flux* is defined as the product of a cross-shelf velocity u and a scalar property c (heat, salt, oxygen, or particle concentrations), acting over determined space and time scales, yielding concentration or energy units per unit time. A 2-D model for mass/energy transport assumes dependency on cross-shore and depth changes in velocities and quantities passing through a cross-sectional area dA (Figure 1). Alongshore

homogeneity and lack of transport at the land/ocean interface are also assumed, thus characterizing the inshore region as a control volume.

At a long-enough time scale *T,* vertically-integrated, cross-shore volume flux of water needs to be insignificantly different from zero to satisfy principles of volume conservation. Thus, if properties are homogeneously distributed in the water column, no transport of any scalar will occur at those scales. Deviations from this will indicate biological sources and sinks and/or atmospheric exchanges within the innershelf region.

The time scale *T* where net cross-shelf volume transport of water approaches zero is represented by the following equation:

$$\int_{t_0}^{T}\int_{0}^{Z} u\,(z,t)\,dz\,dt \sim 0$$

where *u* is the cross-shore velocity, *z* is depth and *t* is time. Thus, for each time scale *T*, the total amount of materials or energy being transported through a cross-section *dA* can be estimated by integrating *u* and *c* over depth *z*, alongshore distance *l* and time *t*:

$$F_c(t_0 + T/2) = \int_{t_0}^{T}\int_{l_0}^{L}\int_{0}^{Z} u\,(z,t)\,c\,(z,t)dz\,dl\,dt$$

This numerical integration can be re-written as the summation of *u* times *c* at all depths multiplied by their bin sizes *dz*, *dt*, and *dl*. Since the length *L* where properties are conserved in this 2-D cross-shore model is unknown, the alongshore integration may be omitted and F_c can be reported simply as "mass (energy) per unit-length of coastline".

2. Data and Methods

The study area is the nearshore/innershelf Santa Barbara Channel region shown in Figure 2. For the purposes of this work, waters shallower than 10 m depth are called "nearshore", while waters deeper than 10 m are called "innershelf" or referred to simply as the area "offshore" of the 10 m isobath.

An underwater 200m Teledyne Webb Research G2 Electric Glider (http://www.webbresearch.com/) sampled a top-to-bottom, 4.25-km long cross-shelf section between the 18 and 70m isobaths, where the shallower measurements were directly south of the Mohawk Kelp Forest, a core Santa Barbara Coastal Long-Term Ecological Research site (SBC-LTER). The LTER maintains an Acoustic Doppler Current Profiler (ADCP) at the reef site (MHK mooring), on the 10m isobath, and about 350 meters north of the shallowest glider observations (Figure 2). The glider did not sample waters shallower than 18m due to maneuverability and energy efficiency constraints [e.g. *Rudnick et al.,* 2004]. Since the goal of this analysis is to use both ADCP measurements and glider data to retrieve flux estimates for the nearshore zone, all glider data for waters deeper than 30m were excluded from the analysis (see Figure 2).

Glider data presented here include conductivity, temperature and pressure from a pumped CTD (SeaBird SBE-41), from which density and salinity are obtained; chlorophyll-fluorescence (excitation 465nm / emission 695nm; WETLabs ECO Puck FLBBCDSLK), a proxy, with caution, for phytoplankton abundances; volume scattering function (VSF) at 650nm (θ=117◦, 20nm spectral bandwidth, WETLabs ECO Puck BB3SLK), which is calibrated to optical backscattering units and serves as a proxy for suspended particulate

materials; and dissolved oxygen from an oxygen optode (AANDERA 3830), which provides data on the balance between supply through circulation and biological production and loss through respiration [*Kortzinger et al*., 2004]. Data were collected in a saw-tooth pattern, from ~0.5m below the surface to ~1m above the bottom with a sampling rate of 0.25 Hz. Typical glider forward velocities were ~0.3m/s, resulting in an average horizontal resolution of approximately 50m. The glider was deployed in six 2-3 week long missions in March 2012 (hereafter Mission 4, or M4), July 2012 (M5), September 2012 (M6), December 2012 (M7), February 2013 (M8) and June 2013 (M9). In total, sampling spanned 92 days.

The ADCP data at Mohawk Reef is a Work Horse 600kHz (RDI Instruments), and collects velocity estimates from 1.5m above the bottom to ~1m from surface, at 0.5m vertical bins, every 20 minutes (data is available at http://sbc.lternet.edu/data/). The data available are pre-processed and a quality control procedure to remove data that do not meet certain error thresholds is already applied (i.e. artifacts such as side-lobe reflection are already removed). These corrections resulted in the exclusion of data from the top 2-3m of the water column during portions of M7, likely due to the large waves incident at those times.

Tidal changes in the region vary between 0.5 and 1.5m, and a pressure sensor located at the bottom of the mooring provided information on the height of the water column at the same times as the ADCP retrievals. Due to the near-surface and near-bottom gap in velocity estimates, velocities were assumed to be constant from the top good bin to the surface (calculated from the pressure sensor), and from the bottom good bin to the bottom. *Fewings et al*. [2008] showed that using this method or other extrapolation techniques to fill in data gaps yield similar results. A CTD (SeaBird SBE-37) mounted at ~4.5m from the bottom at the MHK mooring provided the only temperature/density measurements at the nearshore site.

2.1. Processing and calibration of glider chlorophyll, backscatter and oxygen data

Glider chlorophyll fluorescence and VSF measurements were converted into chlorophyll-a concentrations and particle backscattering at 650nm (and further conversion into total suspended matter – TSM - units) as detailed in Chapter One. Here they are referred to as P_{bio} (mg/m^3) and P_{sed} (in TSM units of mg/m^3).

The oxygen optode has a comparatively long sensor response time than the other sensors on the glider (up to 40 seconds), which resulted in significant offsets between upcast and downcast profiles. Optode data also need to be corrected for salinity changes, since the instrument is tuned for fresh water studies. A Matlab script that corrects glider oxygen data is provided in Appendix A, and all calibration steps and information on optode data artifacts are available in much more detail in *Bishop* [2008]. In summary, the glider's optode outputs oxygen data in concentration units (μM), which is computed as a function of temperature (measured internally by the optode) and phase data (phase of the received red luminescent light, in degree units; more information on the luminescence quenching principles used by the optode can be found in the Aandera's TD218 Operating Manual). However, dissolved oxygen data from the optode and the optode's temperature sensor have long and different response times, such that they are out of sync with one another and with the glider CTD data. Moreover, optode temperature was observed to be considerably different from CTD temperatures, here considered to be the "true" temperature (up to 3°C difference). Thus, dissolved oxygen data need to be first back-calculated into phase units using the provided manufacturer's sensing foil calibration coefficients. Phase information is calculated by

finding the roots of a polynomial provided by the manufacturer. Then, a time-lag correction is applied so that all variables (CTD and phase data) correspond. This is done using a recursive filter that adds a time shift to the CTD data, minimizing the temporal mismatching between CTD and phase data. Then, oxygen concentrations are re-calculated using CTD temperatures instead. Finally, a salinity correction is applied to the final data (per manufacturer's recommendation). In this study, the salinity correction reduced O_2 concentration values by about 38 μM, which is crucial to obtain better saturation estimates. These steps were performed for each mission separately, and different time shift constants were applied to different missions (ranging from 25 to 50 seconds). No validation with other oxygen measurements is available. Specifications for this optode indicate that its accuracy is ± 8 μM (around 5%).

Apparent Oxygen Utilization (AOU), the difference between the saturation oxygen concentration and observed oxygen concentration, was calculated to infer respiration processes in the ocean, attempting to decouple the variability of dissolved oxygen due to physical processes from biological processes [*Ito et al*., 2004]. AOU was calculated using the Gibbs SeaWater Oceanographic Toolbox for Matlab (www.teos-10.org).

Dissolved oxygen and AOU concentrations were converted from μmol/l to mg/l by dividing concentrations by 31.25 g/mol, the molar mass of O_2, and then multiplying the result by 1000 to achieve mg/m^3. Temperature was converted to heat by multiplying temperature units by the specific heat of seawater (3850J/kgC) and its mean density (1025kg/m^3), yielding units of Watts. Salinity in psu units (g of salt per kg of seawater) was converted into kg of salt to m^3 of seawater by dividing salinity by 1000 and multiplying it by a scaling density (1025kg/m^3).

2.2. Coordinate system definitions

Raw ADCP data need to be rotated in order to represent alongshore and cross-shore estimates. A principal axis rotation is usually the chosen method for such transformation. Raw ADCP data at MHK, however, show a boomerang pattern in the distribution of U (East-West) and V (North-South) velocity components (Figure 3a). The pattern suggests that there is a bathymetric steering that causes waters travelling East to deflect Southeast, while not deflecting waters that travel in the opposite direction. High-resolution bathymetry information within this area would be necessary to explore this hypothesis. In order to correct for this effect, high-frequency ADCP data from March 2012 to June 2013 were split into two groups of positive and negative U velocities (Figure 3b; U velocities are positive towards East), and the principal axis rotation was applied to each group separately (Figure 3c). In this case, sample U-V pairs with positive U velocities were rotated by ~26 degrees, and pairs with negative U were rotated by ~4.8 degrees. This resulted in alongshore and cross-shore estimates that are now uncorrelated with each other over time, as expected. The double-rotation likely generated unwanted artifacts, especially for the smallest velocities. Sign definitions are such that alongshore velocities are positive to the East (or Equatorward), while cross-shore velocities are positive towards the shore. Here, the analysis focuses on cross-shore velocities and cross-shore fluxes, so, unless otherwise noted, all velocity data discussed refers to cross-shore estimates.

2.3. Spatial matching of glider and ADCP data

One of the main assumptions in this study is that velocity and optical profiles at the ADCP location (~10m isobath) relate to the seawater property profiles at the glider location (18 to 30m isobaths) via density surfaces, even though they are typically 350-500m apart. This assumption is somewhat supported by *Cudaback et al.* [2005], who showed good correlation and similar seasonality between mid-shelf and innershelf currents near this region. Thus, it is theoretically possible to estimate what the water column profile at 10m should look like based on the water column properties at 18-30m by linking isopycnals at both locations. However, while the glider provided depth-resolved density profiles, only one density measurement from a CTD at 4.5m depth was available at the mooring. Thus, a density profile at the mooring site had to first be constructed to allow propagation of values.

The surface-most and bottom-most glider density values for each glider profile were used as the baseline for the top-most and bottom-most density values at the mooring site (see Figure 4). This assumes that bottom density from the glider matches the bottom density at the mooring. Then, density values at the mooring were interpolated from bottom to mid-depth, and from mid-depth to surface every 0.5m to match the ADCP bins. Profiles from all other biogeochemical properties were also averaged to match each bin, effectively creating new profiles at the 10m isobath. Profiles were excluded if mid-depth density at the mooring was larger than the deepest glider densities. Assuming both density measurements at the glider and mooring are reliable, this indicates those cases when different water masses were present at the two locations. Overall, ~2000 profiles of physical and optical data for the nearshore region were re-created. The errors related to the creation of these profiles are unknown.

Certainly, velocity and bio-optical data should ideally be obtained simultaneously in time and space.

2.4. Temporal matching of glider and ADCP data: limiting the contributions of high frequency processes

The sampling strategy for the original glider work (highlighted in Chapter One) required the glider to travel four km in about 3.5 hours. This resulted in the glider only visiting the innershelf region for about 1.5 hours at a time, with a revisit time (i.e. the time to travel offshore and back) of 7 hours at best. Thus, innershelf data are aliased to tidal changes and other smaller scale disturbances. In order to increase the level of confidence in the innershelf profiles, glider data were averaged over many casts (~18-30m) at each inshore glider pass to reduce high frequency variability due to internal waves and other disturbances on the order of ~ 1.5 hours. In order to allow appropriate depth binning, each of the ~2000 glider profiles were first interpolated every 0.1m in depth. Then, glider profiles that were obtained within 1.5 hours of each other were averaged together to form one profile. This approach acted as a low pass filter on the data and resulted in 206 depth-resolved profiles of physical and optical glider data for the nearshore region, roughly spaced ~9 h apart within each mission. These mean data were considered to be the "true" depth-resolved profiles for that time.

Mean ADCP velocity data for the time spans of each of the 206 glider profiles were also computed to allow direct comparison between optical and velocity data, thus acting as a low-pass filter on the velocity data. Standard error of velocity estimations were small, and these profiles were used as "true" velocity profiles over time.

2.5. Cross-shelf flux calculations

Here it is assumed that the 206 mean profiles reliably represent the water column properties at those time scales. In order to assess at what time scale T the average flow field obeyed to volume conservation per mission, the longest continuous portion of data for each mission whose mean integrated cross-shelf volume (including uncertainties) over time reached zero were selected (see Table 1). Out of the 206 initial profiles, 154 were chosen as adequate to represent this condition, and the number of profiles available for each mission is highlighted in Table 1. M6 never quite reached a zero cross-shelf transport estimate during the mission time, even though 38 profiles were available (nearly the greatest number of all of the missions). This might indicate a persistent onshore flow acting at those times, making it difficult to differentiate physical advection from biological changes. Data from M4 were excluded from the analysis since only four profiles obeyed the zero cross-shore volume condition, and are not discussed further.

An alternative approach to calculating total fluxes is used here to retrieve additional information on the space-time variability of transports across the shelf. Time-averaged transports of a concentration c are often assumed to have a contribution from the averaged correlations between velocity and heat/salt/oxygen/particle anomalies [*Treguier et al.,* 2012]. These terms are referred to as turbulent or eddy transports in ocean-atmosphere [e.g. *van Loon*, 1979; *Treguier et al*., 2012] and benthic-ocean flux studies [e.g. *Lorke et al*., 2013], as well as in nutrient advection ocean models [e.g. *Levy et al*., 2012]. Reynolds decomposition can then be used to break velocity and concentration estimates into means and deviations from the means, such that:

$$u(t) = \bar{u} + u'(t)$$

and

$$c(t) = \bar{c} + c'(t)$$

where overbars indicate temporal averages over the time scale T where cross-shore volume flux approaches zero and are calculated as

$$\bar{u} = \frac{1}{N} \sum_{i=1}^{N} u_i$$

$$\bar{c} = \frac{1}{N} \sum_{i=1}^{N} c_i$$

and primes denote fluctuations about the mean according to:

$$u' = u_i - \bar{u}$$

$$c' = c_i - \bar{c}$$

Thus, for each time period T, the ensemble average of u times c ($i.e.\,\overline{uc}$) can be re-written as:

$$\overline{uc} = \overline{(\bar{u} + u')(\bar{c} + c')} = \overline{\bar{u}\bar{c} + \bar{u}c' + u'\bar{c} + u'c'}$$

and since the average deviation from the average ($\overline{u'}$) is zero, *Flux* becomes

$$Flux = \bar{u}\bar{c} + \overline{u'c'}$$

which has units of *mass(energy) / m^2s*. The first term $\bar{u}\bar{c}$ describes the transport of c due to mean currents within the time-scale T ($Flux_{mean}$), and the second term $\overline{u'c'}$ refers to the net effect of time-varying transports (on sub-inertial time-scales) on c ($Flux_{var}$). Here, these fluxes were analyzed separately to address the impacts of the mean and time-varying flows on total transport across the shelf. The mean, time-varying and total fluxes crossing the 2-D plane (in units of *mass/s per m* of coastline) can be expressed as:

$$Total\ Flux_{mean} = \int_0^Z Flux_{mean}\ dz$$

$$Total\ Flux_{var} = \int_0^Z Flux_{var}\ dz$$

$$Total\ Flux = \int_0^Z Flux\ dz$$

Uncertainties in $\bar{u}, \bar{c}$, *u' and c'* were assessed as standard errors (SE), e.g.:

$$\bar{u}_{se} = u_{se}' = \frac{\sqrt{\frac{1}{N}\sum_{i=1}^{N}(u_i - \bar{u})^2}}{\sqrt{N}} = \frac{stdev(u)}{\sqrt{N}}$$

Standard errors for the terms 1) $\bar{u}\bar{c}$, 2) $\overline{u'c'}$, 3) *Total Flux*$_{mean}$, 4) *Total Flux*$_{var}$ and 5) *Total Fluxes* were propagated according to the following:

1) SE $\bar{u}\bar{c}$ (*Flux*$_{mean}$)= $\bar{u}\bar{c}\sqrt{\left(\frac{\bar{u}_{se}}{\bar{u}}\right)^2 + \left(\frac{\bar{c}_{se}}{\bar{c}}\right)^2}$

2) SE *u'c'* = $u'c'\sqrt{\left(\frac{\bar{u}_{se}}{\bar{u}}\right)^2 + \left(\frac{\bar{c}_{se}}{\bar{c}}\right)^2}$

SE $\overline{u'c'}$ (*Flux*$_{var}$) = $\sqrt{\frac{1}{N}\sum(SE\ u'c')^2}$

3) SE *Total Flux*$_{mean}$= $\sqrt{\sum(SE\ \bar{u}\bar{c})^2}$

4) SE *Total Flux*$_{var}$ = $\sqrt{\sum(\text{SE}\ \overline{u'c'})^2}$

5) SE $Total\ Flux$ = $\sqrt{(SE\ Total\ Flux_{mean})^2 + (\text{SE}\ Total\ Flux_{var})^2}$

2.7. Environmental Forcings

Selected local/regional forcings are used to provide the general environmental context to the bio-optical data during the glider experiment. Wind speed/direction were obtained from NDBC buoy 46053 (http://www.ndbc.noaa.gov/station_page.php?station=46053), located 17km south of the study area. Wind stress was calculated following *Edson et al*. [2013], and rotated into principal axis coordinates, such that by convention negative values refer to upwelling favorable winds [*Brzezinski and Washburn*, 2011]. Tidal heights were obtained from the Santa Barbara's Stearns Wharf pier (3km from study area; maintained by the SBC-LTER, sbc.lternet.edu). Significant wave height data was obtained from NDBC buoy 46216 (http://www.ndbc.noaa.gov/station_page.php?station=46216), ~8km southwest of the study area. Tide, wind and significant wave height data were assembled around the time interval of each glider profile. Fifteen-minute resolution precipitation records were obtained from the Coal Oil Point Reserve coastal weather station (http://www.geog.ucsb.edu/ideas/), and were transformed into accumulated rainfall over a 9-hour period, after which the closest values to each glider profile timestamp were selected. Environmental data obtained closer to the innershelf study area would undoubtedly provide more direct ways to relate *in situ* patterns and fluxes observed to possible physical forcings.

3. Results

3.1. Environmental setting

The wind, wave, precipitation and tidal conditions around the mean time of each profile used in this analysis are shown in Figure 5. Hourly observations within each mission are also provided for comparison. Observations are similar to the ones highlighted in Chapter One for the full glider time series. Wind stress was predominantly upwelling-favorable, but strong upwelling conditions were only observed during M8 and M9 and end of M7 (Figure 5a). Cross-shore winds show very large variability, as well as apparent ~6-day cycles during M5 and M6 (Figure 5b). A wind reversal event during the storm of M7 accompanied the largest rainfall event of the year (Figure 5a and 5d). Large surface waves were observed during the same winter mission, and comparable wave conditions were observed in M8 during upwelling conditions (Figure 5c). Tidal variability is better captured during M7 (Figure 5e), when the interval between profiles was more evenly distributed. Averaging the environmental variables around the mean time of each glider profile resulted in many scales and patterns of variability being missed, such as the diurnal cycles in winds and waves, and the different tidal phases (see right panels in Figure 5).

3.2. Time-depth distribution of properties at the 10m isobath

The time-evolution of all 154 profiles of velocity and estimated bio-optical properties at the 10m isobath are shown in Figure 6. Missions are concatenated into one single time series and daily tick marks are highlighted. Cross-shelf velocities are small and highly variable over time and space and two-layer flows characterizing upwelling and downwelling-like patterns are often observed (Figure 6a). Alongshore velocities are presented in Figure 6b, showing reversals in direction consistent with tidal motions, and confirming the poleward

tendencies of the flow during summer and winter and equatorward flows during periods of strong upwelling [*Harms and Winant*, 1988; *Fewings et al*., 2015].

The warmest waters are observed during M6, while the coldest are observed during M8, in agreement with stratified summer and upwelling/winter conditions of the nearshore region, respectively (Figure 6c). The lowest salinities were observed closer to the surface during M7 during a rainfall event (Figure 6d). Salinity inversions were observed during M6, with oscillating saline surface layers following pulses of warmer temperatures. P_{bio} appears confined to the bottom layers of the water column, especially during M5 and M9, when the biggest blooms were observed (Figure 6e). M8 showed the lowest overall P_{bio} estimates. Cross-shelf P_{bio} observations in Chapter One found that these phytoplankton patches oscillate across the shelf on episodic time scales, and that wind stress, stratification conditions and the strength of the SBC eddy partially explain changes in the magnitude of P_{bio}. P_{sed} dominated a large portion of the water column at these shallow areas, with M7 showing the strongest nepheloid layers associated with mixing, discharge and re-suspension (Figure 6f). Indeed, variability in the intensity of suspended particle loads was linked to the occurrence of large surface waves in Chapter One, but processes such as Stokes drift and return flows, upwelling fronts and tides likely control vertical particle distribution during periods of low wave activity. Oxygen (and AOU) patterns are complementary to temperature changes, with notable short-term changes, especially during M5 and M8 (Figure 6g-h). Near-surface AOU values are close to zero (and often negative) especially during the more stratified missions M5, M6 and M9, indicating saturation or super-saturation of these surface waters. Near-zero surface AOU values are indeed expected and indicate an ocean-atmosphere equilibrium state, increasing the confidence in the optode data.

3.3. Mean vertical distribution of cross-shore velocities and glider variables

3.2.1 Cross-shore velocities

Mean velocity profiles for each mission are shown in Figure 7, allowing characterization of general patterns of cross-shelf flow variability. Although mean cross-shelf velocities per mission are small (Figure 7a), variance about the mean is large on a profile-to-profile basis. Mean flows are generally C-shaped, with offshore or weak flow near the surface and bottom and onshore flow in the middle of the water column, as previously observed for the area [*Fewings et al*., 2015].

The variability of cross-shore velocities is assessed through EOF analysis, which partitions patterns of a time evolving dataset into a set of uncorrelated spatial modes (Figure 7b) and independent, time varying amplitude functions [Figure 7c; *Emery and Thomson,* 1997]. The top meter of the water column is not included in the EOF analysis due to temporal differences in sea-level height (visible in Figure 6). The first 3 EOF modes explain 93.6% of the variability in the cross-shelf velocities. The first mode explains 60.6% of changes in cross-shore velocities and corresponds to the first baroclinic mode of current variability. It shows the typical 2-layer flow that give rise to upwelling and downwelling flows in the innershelf. The barotropic-like mode is seen in the second mode, explaining 21.4% of the variance in the data. The shape of its amplitude function resembles the mean cross-shelf current estimates ($r=0.94$, p-value<0.001). The second baroclinic mode is shown in the third mode, explaining 11.6% of the variability in cross-shore velocities. To help determine the

drivers of the cross-shelf flow patterns, Table 2 shows correlation coefficients among the velocity amplitude functions and mean velocity measurements and wind stress, significant wave height, and near-surface and near-bottom temperature estimates. Little of the velocity variance is explained by regional winds, as also reported by *Cudaback et al*. [2005] and *Fewings et al*. [2015]. The poor correlations may be related to the large spatial separation between the buoys used and the ADCP location.

High-resolution ADCP data at the MHK mooring (sampling interval = 20 min) for the 2012-2013 period is used to better characterize the main temporal scales of velocity variability using power spectra analysis (Figure 7d), and reveal clear diurnal and semi-diurnal peaks. Within the duration of each mission, diurnal and semi-diurnal peaks are resolved during all missions but M9 (see Appendix B).

3.2.2 Glider variables

The variability of vertical profiles of estimated glider parameters at the 10m isobath are shown in Figure 8, summarizing observations in Figure 6. Seasonal effects on temperature profiles are easily observed (Figure 8a), with the coldest waters observed near the bottom in M8 (winter), and the warmest temperatures registered near the surface in the summer-spring months (M6 and M9). Depth-profiles were relatively homogeneous during M7 and M8 due to strong mixing conditions. Temperature profiles during the remaining missions showed a thermocline around 5m depth.

Salinity profiles were relatively constant throughout the water column (Figure 8b), and the largest top-to-bottom gradients are observed in M7, reflecting the advection of a surface buoyant plume, and in M6, due to the previously mentioned inversions. Even though

the rain event lasted 2-3 days, only one profile during M7 shows very low near-surface values, exemplifying the difficulty in sampling these episodic events with a single moving glider. M9 shows the most saline water columns, in agreement with winds that induce upwelling during spring-time (see Figure 5).

A sub-surface P_{bio} maximum is observed mid-water column during all missions (Figure 8c), and often much closer to the bottom as is the case of M5. This is not surprising since the water column in this region is shallow and likely well illuminated throughout the seasons. Variability is large over depth and time, with observed concentrations of up to 20mg/m^3.

Mean P_{sed} profiles show that sediment concentrations generally increase with depth (Figure 8d), with high homogeneity on the top 4m of the water column. The largest concentrations were observed during M7 during the storm event. Maximum P_{sed} values are found near the bottom and ~1-3m above the bottom, denoting the presence of bottom and intermediate nepheloid layers throughout the time series.

Mean dissolved oxygen profiles are generally lower at the bottom, as expected from the intrusion of low O_2 waters through upwelling and degradation of organic matter in the water column and sediments [*Connoly et al.*, 2010; Figure 8e]. Dissolved oxygen concentrations are higher near the surface with occasional sub-surface maximums such as during M5 and M9 (the missions with the highest P_{bio}), suggesting production of oxygen by phytoplankton. Weakly stratified missions M7 and M8 show relatively homogeneous dissolved oxygen concentrations within the water column. On a mission-to-mission basis, a correspondence between overall dissolved oxygen concentrations and the mean temperature of the water column is apparent, with colder waters showing lower dissolved oxygen

concentration, indicating the likely upwelling-origin of the cooler water masses. The minimum of 150 μmol/l and maximum of 250 μmol/l over the seasons are consistent with previous studies near kelp forests [*Frieder et al*., 2012; *Booth et al*., 2014]. Dissolved oxygen concentrations during the sampled period never reach hypoxic conditions [i.e. O_2 below ~60μM; *Deutsch et al.*, 2011].

The role of respiration or biological activity in controlling dissolved oxygen changes in the water column is assessed through AOU profiles in Figure 8f. A reverse pattern from oxygen is observed, with values increasing with depth for all missions. This indicates that oxygen use is higher deeper in the water column than in the surface, due to low ventilation and/or use by heterotrophic organisms.

3.3 Total cross-shore transport of salt, heat and particles

The total estimated fluxes [i.e. $\bar{u}\bar{c} + \overline{u'c'}$] of heat, salt, P_{bio}, P_{sed}, oxygen and AOU vertically integrated throughout the entire water column and for each mission are shown in Figure 9 (recall that the duration of each mission was determined by the time scales when integrated cross-shore volume transport reached zero). The depth-distribution of these total fluxes is shown in Figure 10. Positive values denote the net accumulation of materials/heat/salt/oxygen/AOU in the nearshore region (i.e. the nearshore region is a sink for these quantities), and negative values denote export out of the nearshore (i.e. the nearshore region is a source). It is important to note that these fluxes suggest conditions at this specific nearshore site only, or at best may apply only to a narrow portion of the coastline. Thus, fluxes up or downcoast might show different or reverse patterns. Clearly, full 3-D observations would be necessary to better constrain the results.

Many of the observed fluxes are centered around zero with large uncertainty estimates. This is especially the case for the variables heat, salt, oxygen and AOU (Figures 9a-d), with only M6 and M9 showing significant net fluxes for some of these quantities. During these two missions, the nearshore is considered a net sink of heat, salt and oxygen. However, the M6 flux estimates need to be interpreted with care since the cross-shore volume transport never quite reaches zero throughout the missions' duration (see Table 1).

The nearshore serves as a net sink for phytoplankton during the more stratified missions M5, M6 and M9, although uncertainties during M5 are not significantly different from zero (Figure 9e). During the winter mission M7, the nearshore region shows a tendency to export phytoplankton offshore. During M8, another weakly stratified mission, net fluxes are small and not different from zero. Fluxes (and uncertainties) are in general higher for the stratified missions than for the mixed condition missions.

Net export of sediments offshore of the study area is observed during missions M5 and M8, while for the remaining missions uncertainty values are not different from zero (Figure 9f). In general, the nearshore acts as a source of sediment, exporting materials offshore. This makes sense since the inner and mid-shelf tend to receive land and beach materials over time, and intense surface and intermediate nepheloid layers have been shown to transport materials along isopycnal surfaces away from the coast (e.g. Cortes et al., 2014). Again, the tendency for net accumulation of sediments in the nearshore region of the study site during M6 might be an artifact related to the non-neutral cross-shore volume flux for the period.

The depth-distribution of total heat, salt and dissolved oxygen fluxes generally follows the C-shape of the mean currents, with the largest transports occurring in the middle

of the water column (Figure 10a-c). With the exception of M8, AOU fluxes are small and more pronounced near the bottom, which might indicate the importance of benthic activity in determining oxygen variability (Connolly et al., 2010; Figure 10d). P_{bio} and P_{sed} fluxes also deviate from the shape of the cross-shelf currents, especially during missions M5, M7 and M9 (Figure 10 e-f). This is because the time-varying component of the fluxes makes up a very large portion of the total fluxes, as discussed below.

3.4. Importance of time-varying transport to total material transport

The relative importance of the time-varying and mean flows in transporting heat/salt/particles/oxygen/AOU across the shelf varies throughout the missions, as does their depth-distribution over time. Figure 11 partitions the total fluxes into temporal mean and time-varying components of the total flux. The depth-distributions of these fluxes (in units of material mass (energy) / second per meter of coastline) are shown in Figure 12, for each variable and mission.

Mean advection controls the transport of heat, salt and oxygen in the system, while advection due to the time-varying flows is very small over all missions (Figure 11a-c). Although uncertainties are large, net oxygen fluxes into the nearshore region are observed during M9 through both mean and time-varying flows (Figure 11c). AOU mean fluxes are centered around zero for all missions (Figure 11d), and time-varying fluxes makes up a large portion of total fluxes.

Time-varying fluxes may provide insights into the biological components changing oxygen concentrations over time. Assuming there is a balance between oxygen consumed by heterotrophic organisms (e.g. bacteria, benthic invertebrates, fish, etc.) and produced by

autotrophic organisms (e.g. phytoplankton, giant kelp, understory algae, etc.), deviations from zero flux may indicate whether the nearshore is exporting or receiving excess oxygen. Time-varying fluxes show that the nearshore acts as a sink for oxygen during M5, M8 and M9 (Figure 11c). This indicates that the nearshore is consuming more oxygen than it is creating, thus suggesting heterotrophic conditions. However, oxygen fluxes reflect the combination of both dissolved oxygen concentrations and the oxygen saturation state. Thus, AOU estimates provide a better estimate of biological consumption in the water column, with the offshore fluxes of AOU during missions M5, M8 and M9 also suggesting heterotrophic conditions of the nearshore zone (Figure 11d). During M7, oxygen and AOU fluxes average zero, in agreement with the high mixing conditions at those times and low phytoplankton abundances observed.

The depth-distribution of the mean fluxes of heat, salt and oxygen shown in Figure 12(a-c), follow the general pattern of cross-shore currents, with offshore transport occurring close to the surface (except for M9), and onshore fluxes occurring in the middle of the water column. Time-varying fluxes of these properties are small, but show tendencies of acting in opposite directions to the mean fluxes in different portions of the water column. These flux cancellations are often observed (and expected) in ocean/atmosphere heat flux experiments [*van Loon*, 1979]. Time-varying AOU fluxes during M5, M6 and M8 show strong offshore flow in the upper half of the water column, with fluxes during M8 distributed in a well-developed 2-layer flow. Near the bottom, AOU is transported offshore by the mean currents and onshore by the time-varying flows during missions M5, M6 and M8. During M7 and M9, all flows are generally small. Time-varying fluxes of oxygen/AOU near the bottom may be associated with benthic heterotrophic activity.

Mean advection dominates phytoplankton fluxes during the stratified missions M5 and M6 (Figure 11e). During M9, both mean and time-varying fluxes make a substantial contribution to the overall budget in phytoplankton distribution, with a tendency of the nearshore acting as a sink for particles. Mean advection of phytoplankton during the weakly stratified missions M7 and M8 is nearly negligible and time-varying fluxes out of the nearshore zone dominate the variability.

Figure 12e illustrates that different portions of the water column control the distribution of P_{bio} differently. Transport towards the nearshore zone generally occurs in the middle of the water column due to the mean flow, while offshore export of phytoplankton occurs closer to the surface and bottom by both the mean and time-varying flows. Cancellation of time-varying and mean fluxes (i.e. similar magnitudes but opposite directions) is a common feature determining overall phytoplankton net transports (e.g. near the bottom during M5 and near the surface during M9).

P_{sed} fluxes due to mean advection are near zero during all missions except during M6 and M9 (Figure 11f). Interestingly, during M9, mean and time-varying fluxes contribute with equal portions of the P_{sed} flux but in opposite directions (mean flux onshore; time-varying flux offshore). This explains the near zero total P_{sed} fluxes during M9 shown in Figure 9d. Time-varying fluxes are significant, larger than the mean flux, and offshore during missions M5, M8 and M9. Time-varying fluxes during M7 are also out of the nearshore zone, but uncertainties are large.

The depth-distribution of these P_{sed} fluxes in Figure 12f shows that the P_{sed} transported away from the nearshore zone due to the time-varying fluxes occur in different portions of the water column during different missions. For instance, during M5, when the

largest overall P_{sed} net fluxes were observed (see Figure 10f and Figure 11f), time-varying fluxes acted over the middle 6 meters of the water column. During M8, the offshore transport of P_{sed} due to the larger time-varying flux occurs in the upper half of the water column, while the bottom half shows transport towards the nearshore. During M9, offshore transport occurs near the bottom.

4. Discussion

The relative importance of the time-varying and mean fluxes of heat, salt, oxygen and particles varies throughout the missions as do their depth-distribution over time. While in this 2-D study mean cross-shelf flow dominates transport of physical properties, mean and time-varying flows appear to be equally important for the transport of phytoplankton and sediments across the shelf. In general, stronger fluxes are observed during stratified conditions (M5, M6, M9), while cross-shore transport is reduced during weakly stratified conditions, as expected when surface and boundary layers overlap (M7 and M8; Lentz, 1995). In the following, fluxes of oxygen, phytoplankton and sediment are summarized in the context of general seasonal oceanographic states of the water column. A schematic is presented in Figure 13. The potential artifacts introduced by the use of aliased datasets are discussed, and a case study using high-frequency glider observations is presented as a proof of concept for future cross-shelf flux studies in the area.

4.1. Conceptual Model for particle and oxygen transports

Previous studies at this site have shown that phytoplankton production in the summer and spring tends to be higher than consumption [e.g. *Miller et al*., 2011]. Thus, 1) significant net cross-shelf fluxes of phytoplankton, oxygen and AOU should be observed, and 2) the nearshore region should show net-autotrophy during these seasons. Significant fluxes (at least for P_{bio} and oxygen) were indeed seen during the late spring mission M9 and, to a lesser extent, during summer missions M5 and M6. However, the nearshore zone is presented here as a sink for these properties, and not a source. During winter, respiration should make up a larger portion of the oxygen balance, such that net fluxes of phytoplankton should be small or negligible. Weakly stratified missions M7 and M8 indeed show this tendency.

The net flux of phytoplankton (and oxygen) during spring and summer shown in this study, which resulted in the nearshore zone presenting heterotrophic conditions, is in agreement with a scenario where offshore waters are exporting materials into the nearshore zone through upwelling and upwelling fronts [e.g. *Franks*, 1992; Figure 13a]. In the wintertime, although fluxes were small, the nearshore zone is shown to export phytoplankton offshore. It is possible that the weaker circulation in the nearshore zone acts to retain particles for longer periods of time. Despite the relatively robust C-shape pattern of mean water velocities, the direction of transports will undoubtedly depend on where in the water column phytoplankton populations are located. In these shallow regions, phytoplankton can be present anywhere in the water column. Thus, it is possible that a slight change in the configuration of the water column along and cross-shelf velocities or the position of the phytoplankton layers may significantly affect the direction of the flux and the role of the nearshore in exporting or receiving excess materials and oxygen throughout the seasons.

The expected cross-shore patterns of sediment distribution are more easily hypothesized, as intermediate and bottom nepheloid layers have previously shown to transport sediments and other particles along and across the shelf [*Warrick et al*., 2005; *Lorenzoni et al*., 2009; *Cortes et al*., 2014; *Chapter One* of this dissertation]. Since shallower waters are the natural source of sediments for the open ocean, sediment fluxes should primarily occur from the nearshore zone. As a result, strong mixing and re-suspension, as well as the development of intermediate nepheloid layers during stratified conditions should lead to net transport of sediments out of the nearshore zone. This is indeed observed during M5, M7 and M8 missions (Figure 9f and 11f), even though uncertainties during M7 were large and onshore transport during M8 was also observed (Figure 13a-b). Offshore transport at this site is shown to occur preferentially through the time-varying fluxes that might sustain along-isopycnal advection, rather than by the mean fluxes. These transports generally occur in the top ~6m of the water column, in agreement with the probable location of surface and intermediate nepheloid layers.

The flux patterns observed here agree with many of the expected effects of stratification on particle transport. Although the profiles selected are likely good representatives of the water column structures at those 1.5-hour time scales (since they were averaged over many casts to reduce high frequency variability), large uncertainties in the results are likely related to the aliasing of glider observations, since the average interval between profiles was between 9 and 11 hours. Thus, the number of profiles used per mission (~30) is not enough to assertively eliminate aliasing issues due to tidal motions, diurnal and larger scale circulation patterns and settling of particles. Conclusive insights into the general cross-shelf fluxes and their distribution within the water column would require additional

data collected at similar stratification conditions and for longer periods of time (or by multiple gliders) at several locations along the coast. Moreover, only an analysis that integrates changes in these biogeochemical properties in a control-volume setting (for instance with data collected around a box where fluxes are measured from all sides) would allow separating flux divergence effects from non-conservative processes such as phytoplankton growth and grazing. Nonetheless, the conceptual model presented here highlights the potential information that could be gained about cross-shelf oxygen and particle balances if appropriate experiments were designed.

4.2 Case-study using glider observations collected as a virtual mooring

From March 12 to March 20 2013, three weeks after the conclusion of mission M8, a different glider experiment was conducted at the 40-50m isobath immediately south of the Mohawk kelp forest. The glider was deployed as a virtual mooring by specifying two waypoints ~300m away from each other and having the glider travel within this limited region (see Figure 2). This resulted in the glider sampling approximately the same vertical profile continually for 8 days. This high frequency glider data is used here along with the high-frequency ADCP data at the 10m isobath as a "proof-of-concept" for the future development of more complete cross-shelf flux studies. This mission is hereafter referred to M8b (Table 1).

Ordinary krigging was used to create a dataset spaced every one hour in time, and every two meters in depth at the 42m isobath (1h = sampling of around 10 profiles). The binning reduced the effects of aliasing due to high-frequency changes in water column properties such as high frequency internal waves. ADCP data were binned every one hour to

match the times of glider profiles. Water column properties at the 10m isobath were estimated from mean glider properties at 42m by linking density surfaces at the glider and mooring locations, and applying the same exclusion criteria as in the previous analysis (see Figure 4). It is clear that the larger physical separation between mooring and glider data (~1km instead of ~500m of the original experiment) may imply that actual velocity and water column profiles at the two locations are less coherent. Certainly, bio-optical and velocity profiles need to be obtained at the same location. Alternatively, water properties at the 10 m isobath were also estimated by simply linking the 20 glider bins at the 42m isobath to the 20 ADCP bins at the mooring site. These results are shown in Appendix C-D, and the method of choice did not significantly affect the flux calculations.

Similar to the main analysis, the appropriate duration or time-scale of M8b for flux calculation was selected by finding the longest continuous portion of the time series where the mean cross-shore volume flux approached zero. A 4-day long period of data satisfied these conditions (7 a.m. March 13 – 9 a.m. March 17). Depth-averaged cross-shore and alongshore velocities for this period, as well as the wind, wave and tidal conditions at the time of the sampling (and two days before) are shown in Figure 14. Mean cross-shore velocities are small and much smaller than mean alongshore velocities, as often described (Lentz and Fewings et al., 2012; Figure 14a). Mean alongshore velocities show a tendency for equatorward flows (Figure 14b), as expected during upwelling conditions that are strong enough to reverse the poleward currents in this region. Winds are upwelling favorable during the first half of the selected period, when diurnal oscillations in wind stress are also visible (Figure 14c-d). During the second half of the mission, winds become weaker and reverse, and surface wave heights increase (Figure 14e). The depth-distribution of cross-shore

velocities, temperature, P_{bio} and P_{sed} for this time length T are shown in Figure 15. Note the hourly tick marks, highlighting the dense sampling of vertical water property profiles collected in a short period of time (N=89, ~22 profiles per day).

The effect of tidal variability in changing cross-shore velocities is seen in Figure 15a. An EOF analysis on this velocity data (Figure 15g) agreed with previous observations (Figure 7b). A two layer flow (EOF Mode 1) explains more than 70% of the variability in cross-shore currents, and a C-shaped water column profile describes EOF Mode 2, with stronger velocities in the middle of the water column. Short-term oscillations in temperature (Figure 15b) and P_{bio} (Figure 15c) are clearly observed, as well as great correspondence between temperature and P_{bio} changes (the clear shape of the diurnal cycle of these properties can be seen in the original glider profiles in Appendix C). The shallow depths of the 1025.5kg/m^3 isopycnal (plotted along temperature estimates), in addition with the upwelling-favorable winds and tendency for equatorward flows shown in Figure 14b-c, indicate that the water column experienced upwelling-conditions during at least the first 2 days of the sampling period. P_{sed} shows strong bottom nepheloid layers that oscillate at short time scales (Figure 15d; near-bottom P_{sed} only correlates weakly with depth-averaged cross-shore velocities (r=-0.25) and depth-averaged alongshore velocities (r=-0.14), but suggests a correspondence between offshore flows and westward flows and increased near-bottom P_{sed} values. In contrast, near-bottom P_{sed} is also significantly correlated with inshore depth-averaged cross-shore flows (r=0.19)). Oxygen changes (Figure 15e) mimic temperature and P_{bio} variations, and low AOU values (Figure 15f) in places where P_{bio} is high indicate high production of O_2 from autotrophs.

Total fluxes of heat, P_{bio}, P_{sed}, dissolved oxygen and AOU and their depth-distributions, as well as the contributions of mean and time-varying terms and their depth-distributions are shown in Figure 16. Fluxes for the case where glider data was not extrapolated to the 10 m isobath are shown in Appendix D for comparison. Again, positive fluxes indicate transport towards the coast. Total heat fluxes average around zero, as expected for physical variables (Figure 16a). The mean flux is dominant and the time-varying flux is small but non-zero (Figure 16b), showing offshore heat export from the surface layers (Figure 16c), as expected for a 2-layer flow during upwelling periods.

Strong offshore export of phytoplankton (P_{bio}) is observed during M8b (Figure 16a). Both mean and time-varying fluxes contribute with a large portion of this export (Figure 16b), which occurred primarily over the top few meters of the water column (Figure 16c-d). This agrees with the expected effect of upwelling fronts in transporting materials offshore close to the surface. Total transport of P_{sed} averages zero throughout the time series (Figure 16a). Time-varying P_{sed} fluxes however are positive and relatively large (Figure 16b), indicating that the nearshore waters are acting as a sink for sediments at those scales. Figure 16c shows that the onshore transport due to time-varying fluxes occurs almost exclusively within the bottom 2.5m of the water column. Interestingly, this pattern was also observed during M8 (Figure 12f), which increases confidence in the observed patterns for that mission.

Similarly to heat fluxes, total dissolved oxygen fluxes are not significantly different from zero (Figure 16a), and the mean flow dominates the total transport (Figure 16b). The non-zero time-varying flux shows offshore transport of O_2, which is the opposite from the observed during M8 in the original experiment (see Figure 11c). Another distinction between the two missions occurs in the AOU patterns. AOU fluxes from mission M8b show inshore

fluxes that are carried by the mean currents within the middle of the water column (Figure 16b-d), and by the time-varying flow over the top two meters of the water column (in agreement with the depth of the P_{bio} offshore export). Certainly, differences between missions M8 and M8b might be due to natural variability of the water column and not only due to the effects of aliasing in the calculation of cross-shelf fluxes during M8. Overall, M8b observations indicate net-autotrophy of the nearshore zone during an upwelling-favorable period of March 2013, with shallow waters exporting excess oxygen and phytoplankton offshore.

Even though four days of high-frequency data are not enough to extrapolate results and analyze the long-term implications of the observations, it is clear from these examples that accurate flux measurements require high frequency bio-optical observations obtained simultaneously (in time and space) to high frequency velocity measurements. Future experiments should consider using multiple gliders or wirewalkers equipped with bio-optical and velocity instruments deployed in a control volume setting in these shallow regions. A control volume experiment would also serve to evaluate the potential effects of alongshelf inhomogeneity and the existence of persistent cross-shore flows such as eddies that might affect volume conservation assumptions at different portions of the coast. Repetition over various seasons or mixing conditions would be critical to assess the role of stratification and environmental properties in driving fluxes throughout the water column. In situ calibration and validation of the data (especially for the fluorometer and oxygen sensors) remains vital, and would allow estimating net community production and other relevant parameters. Finally, a supporting network capable of sampling along and cross-shore winds, local wave

conditions and light availability at the sampling locations would allow a better understanding of the physical vs. biological controls on particle and oxygen transport.

5. Conclusions

Depth-resolved glider bio-optical data and mooring velocity data were used to assess the cross-shore fluxes of phytoplankton, oxygen and sediment materials over seasonal time scales and to quantify the fate of organic matter and patterns of productivity outside of a productive kelp forest. The total, mean and time-varying components of these fluxes were described for different stratification conditions of the nearshore zone. During stratified seasons, the nearshore zone showed heterotrophic conditions, serving as a sink for phytoplankton and oxygen produced offshore. Net-autotrophy was observed instead during weakly stratified conditions. Although concentrations of sediment in the water column were higher during winter, transport of sediments was larger during spring and summer. This is in agreement with stronger circulation patterns of the innershelf during these seasons, when surface and intermediate nepheloid layers are likely important pathways for offshore sediment transport. Results from a case study using high-frequency glider observations showed the need for repeated and simultaneous collection of bio-optical and velocity data to obtain accurate flux estimates.

Tables and Figures

Table 1. Statistics per mission.

Mission	Date	General conditions	number of profiles (N)	number of days sampled	Mean N/day	Median time between profiles (h)	Mean cross-shore volume
M5	Jul-12	stratified + bloom	39	18	2.16	10.27	0.00114 ± 0.00996 m^3/s
M6	Sep-12	strongly stratified	38	18	2.11	9.53	0.01319 ± 0.01289 m^3/s
M7	Dec-12	weakly strat + storm	28	12	2.33	8.76	0.00013 ± 0.02227 m^3/s
M8	Feb-13	weakly stratified	23	10	2.3	8.64	-0.00104 ± 0.01075 m3/s
M9	Jun-13	stratified + bloom	26	13	2	10.68	0.01082 ± 0.01539 m^3/s
M8b	Mar-15	upwelling	89	4	22.25	1	0.0054 ± 0.0060 m^3/s
Total*			**154**	**71**	**2.18**	**9.576**	

* Does not include M8b

Table 2. Correlation coefficients between EOF amplitude functions for cross-shore velocity estimates and wind, wave and temperature data. *AF1* to *AF3* = first three amplitude functions for velocity estimates; *Pax V* = principal axis of wind stress, roughly alongshore; *Pax U* = cross-shore component of wind stress; *SWH* = significant wave height from Goleta Buoy 46216; *surf temp* = mean estimated glider temperature data over the top-most 2m of the water column at the 10m isobath; *bot temp* = mean estimated glider temperature data over the bottom-most 2m of the water column at the 10m isobath; *surface U* = mean cross-shore velocities at the top 2m of the water column; *bottom U* = mean cross-shore velocities over the bottom 2m of the water column; *middle U* = mean cross-shore velocities within the middle 6m of the water column. **Correlation coefficients that are significant at the 95% confidence interval are shown in bold.**

	AF1	*AF2*	*AF3*	*surface U*	*bottom U*	*middle U*
Pax V	-0.1289	**0.1577**	**0.1844**	**0.2248**	0.0044	0.1212
Pax U	0.0058	0.0702	-0.0782	-0.0512	-0.0048	0.0877
SWH	0.1208	-0.0589	0.052	-0.0962	0.1169	-0.0952
surf temp	0.0183	0.0357	0.0125	-0.002	0.0333	0.0281
bot temp	-0.1037	0.0372	0.088	0.1163	-0.0273	0.0562

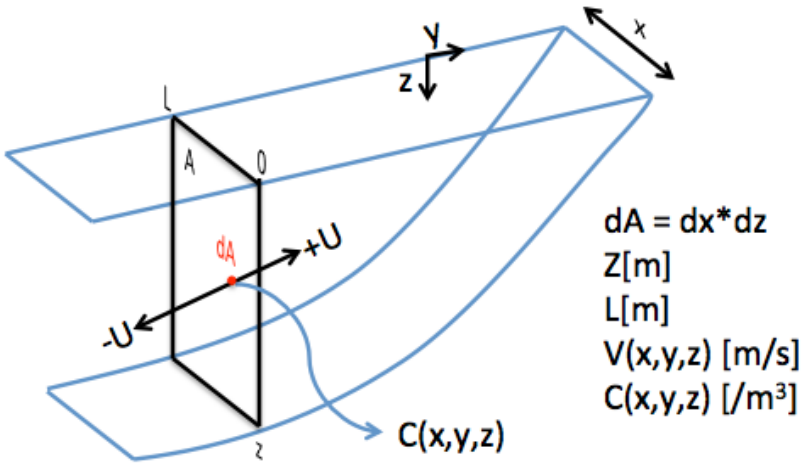

Figure 1. Schematics of cross-shelf fluxes.

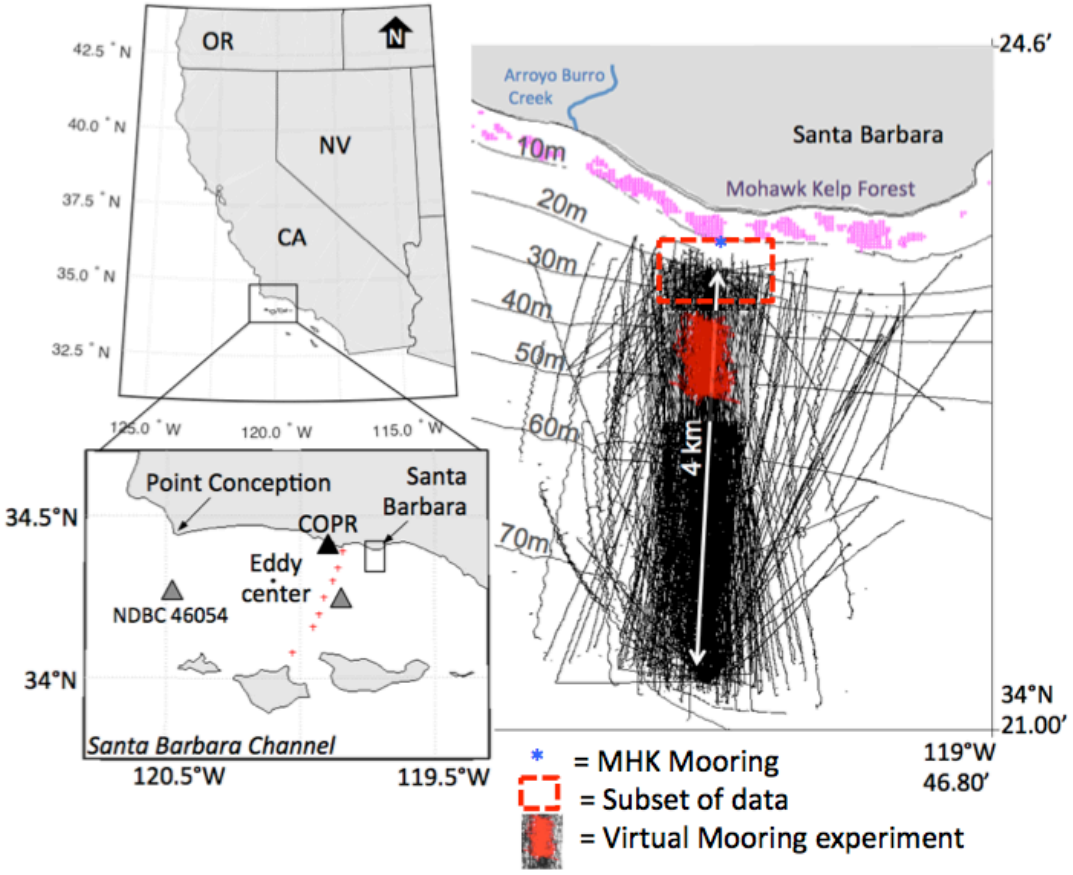

Figure 2. Study area and innershelf glider data used in the study. The location of the MHK mooring and ADCP is represented by the * at the 10m isobath. Glider tracks during mission M8b where the glider was deployed as a virtual mooring is shown in red.

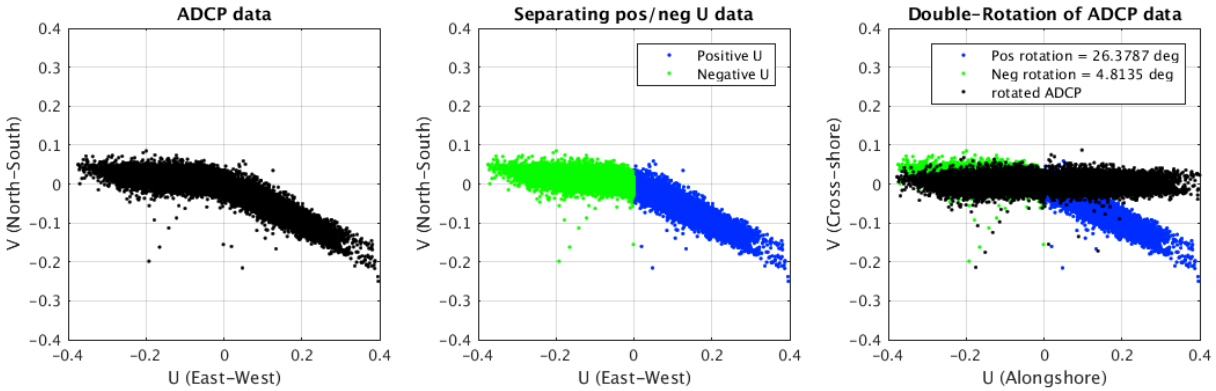

Figure 3. Rotation of ADCP data into principal components. Sample U,V pairs with positive U velocities were rotated by ~26 degrees, and pairs with negative U were rotated by ~4.8 degrees. The rotated pairs result in uncorrelated U and V estimates.

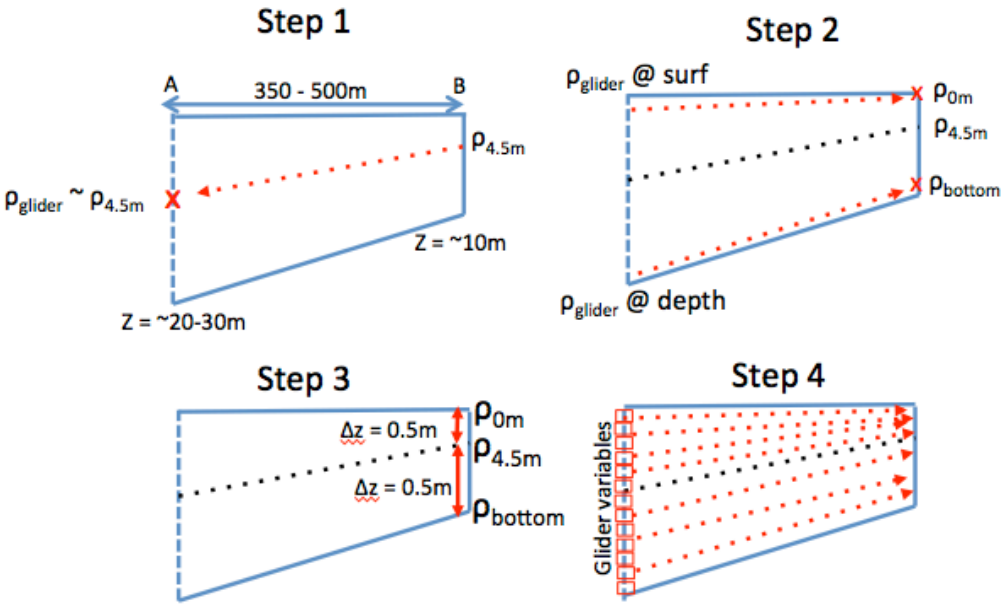

Figure 4. Estimating glider profiles at 10m depth based on density distribution at MHK and glider isobaths.

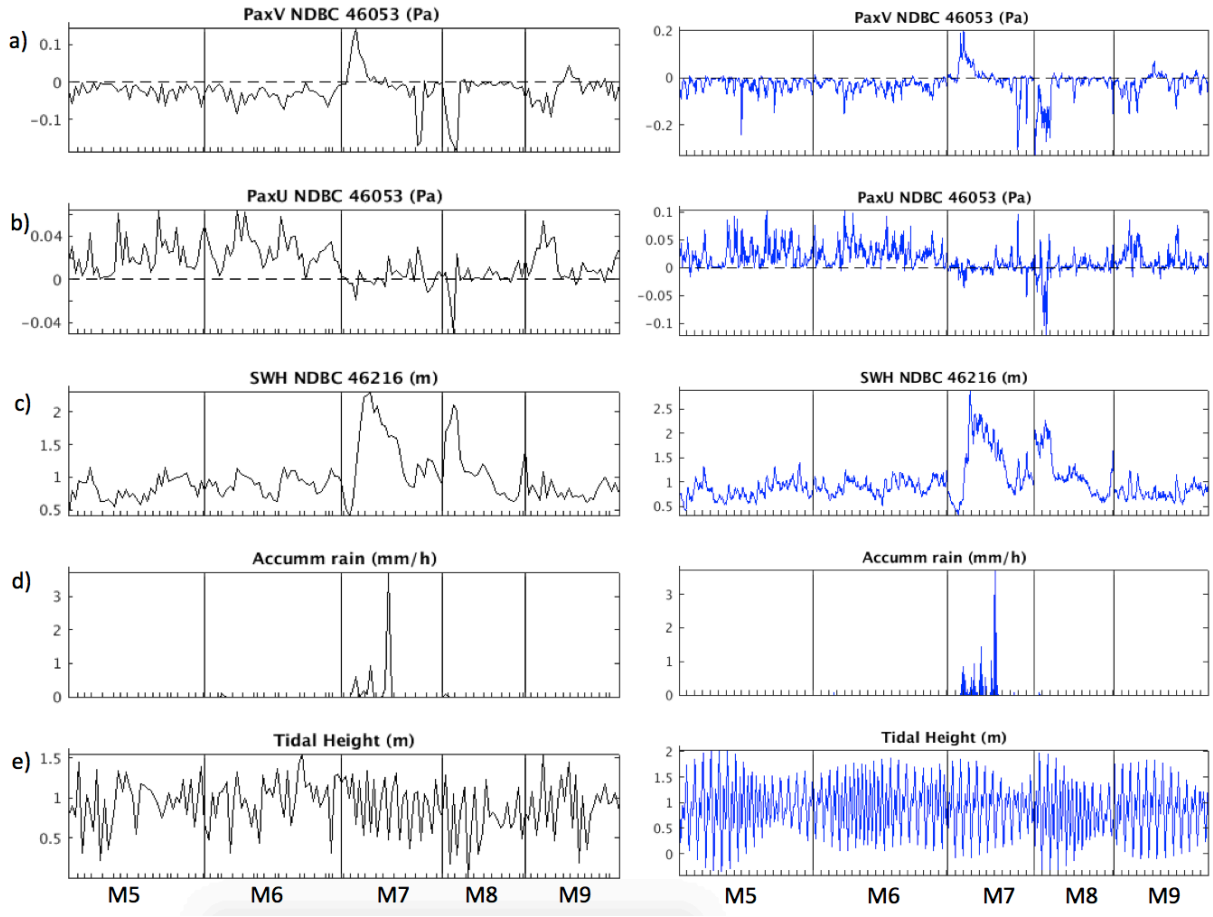

Figure 5. Left panels: Environmental setting at the mean time of each nearshore profile (i.e. every ~9h apart). Right panels: the same forcings obtained every one hour during the period of each mission. Note how information is missed when averaging over long periods of time, leading to aliasing. a) Principal axis of wind stress (along-channel); b) secondary axis of wind stress; c) significant wave height at buoy 46216; d) Precipitation at Coal Oil Point Meteorological station; e) Tidal heights. Sequential profiles are plotted, and daily tick marks are highlighted.

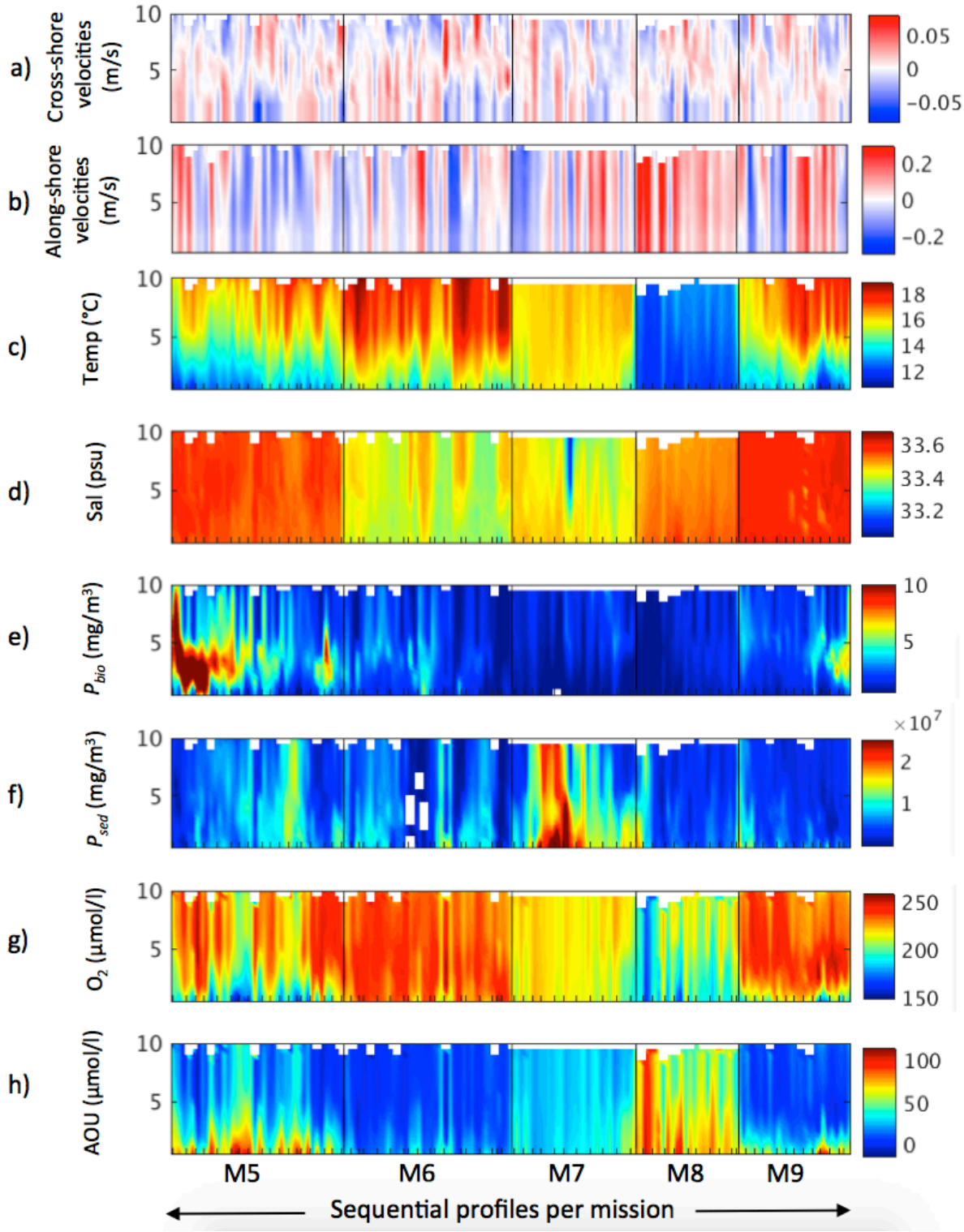

Figure 6. Mean Cross-shelf velocities from ADCP at the Mohawk Mooring (a), and estimated temperature (b), salinity (c), P_{bio} (d), P_{sed} (e) and dissolved oxygen (f) at the nearshore site from innershelf glider data. All missions were concatenated into a single time series, with a thin black vertical line separating them. Daily tick marks are shown.

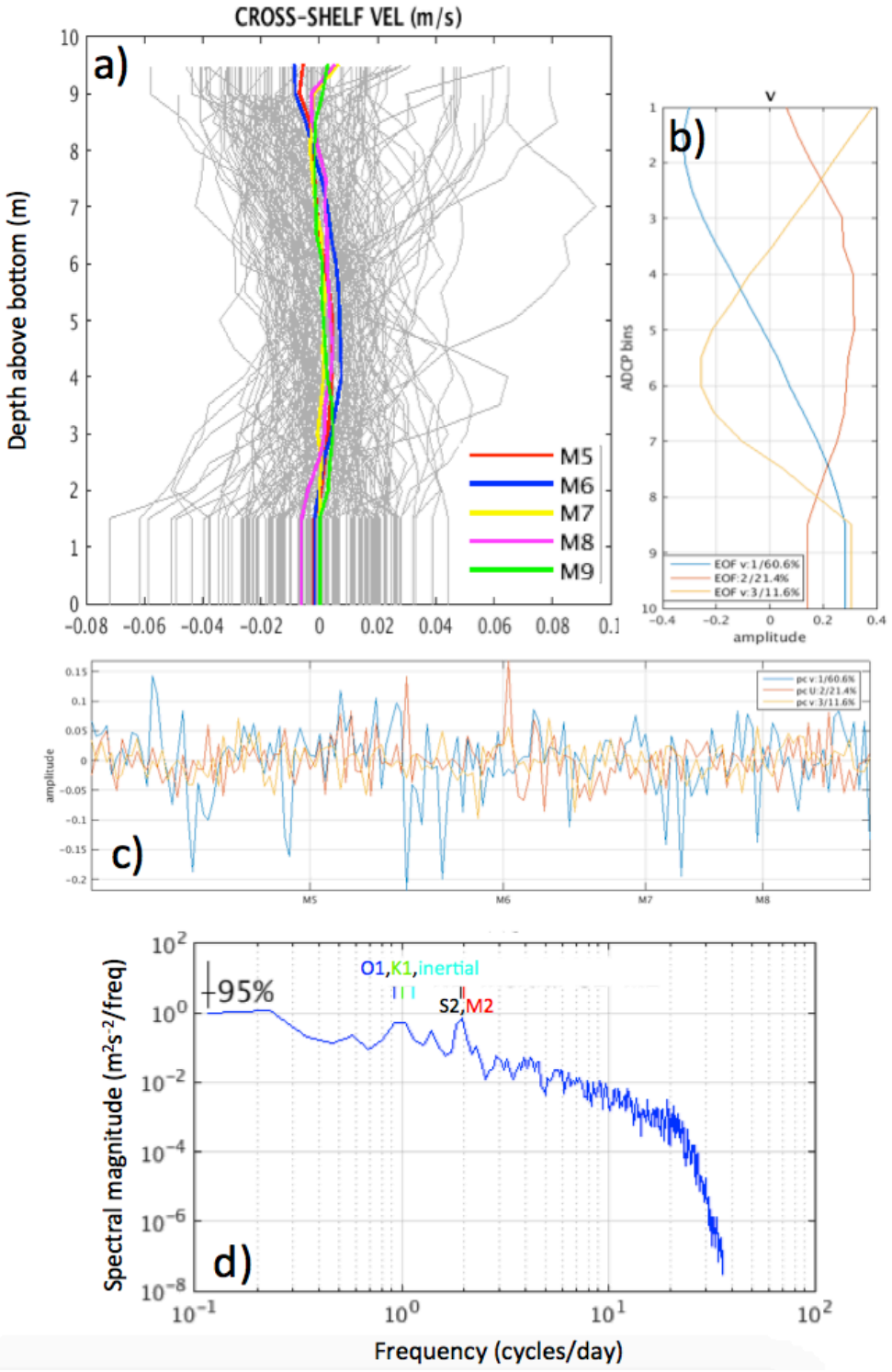

Figure 7. a) Mean cross-shelf velocities per mission (color) and variability (grey); b-c) EOF and amplitude functions for cross-shelf velocities; d) Frequency Spectra of velocity data (from high-resolution ADCP data) for the sampling period. The location of solar and lunar tidal frequencies and inertial frequencies are highlighted in d for reference.

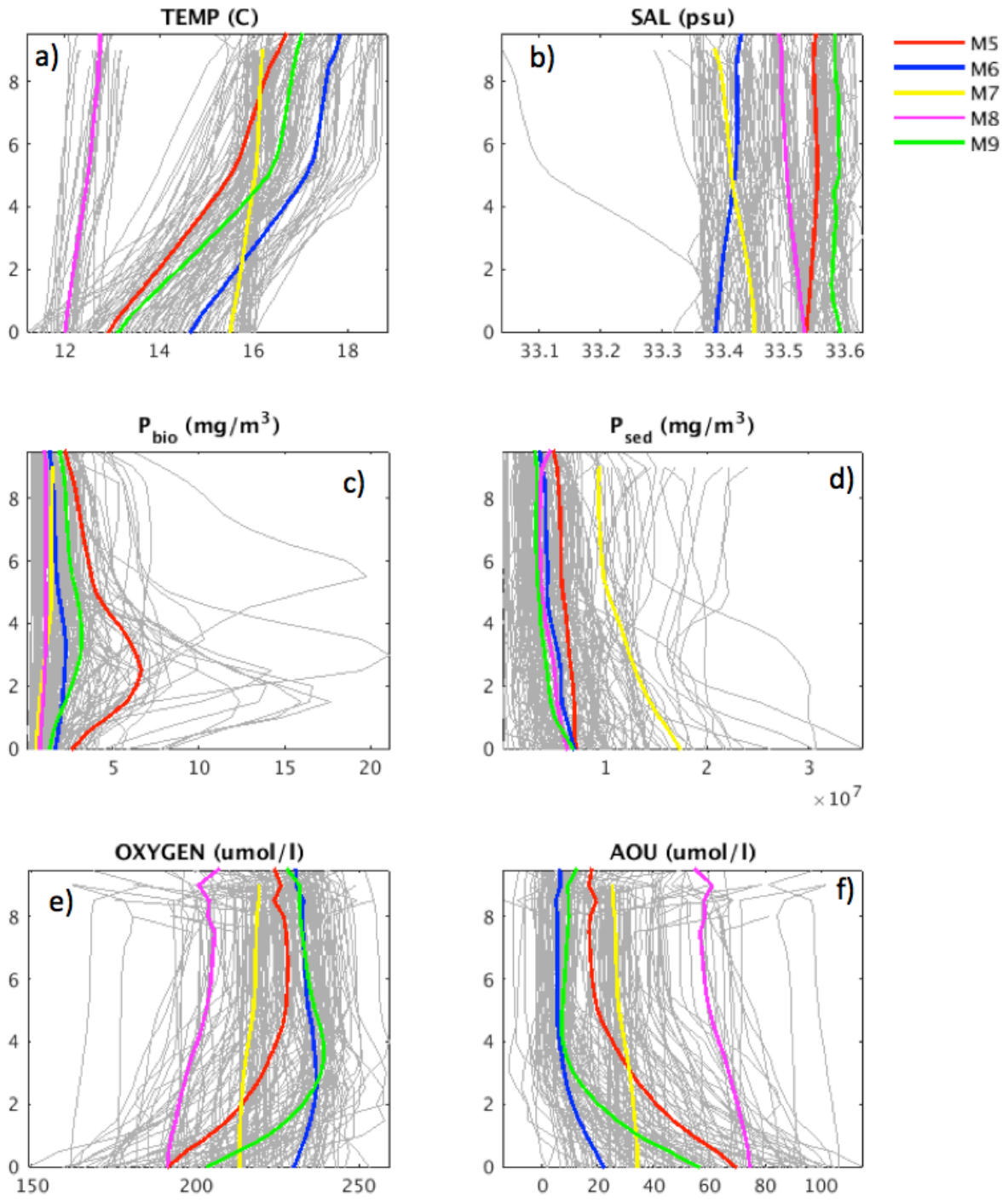

Figure 8. Vertical distribution of estimated profiles of a) temperature, b) salinity, c) P_{bio}, d) P_{sed}, e) dissolved oxygen (O_2), and f) apparent oxygen utilization (AOU) at the 10m isobath. Grey profiles are each of the 154 profiles used here, and colored lines denote mission-means. Y-axis is distance from bottom in meters (surface = 10m).

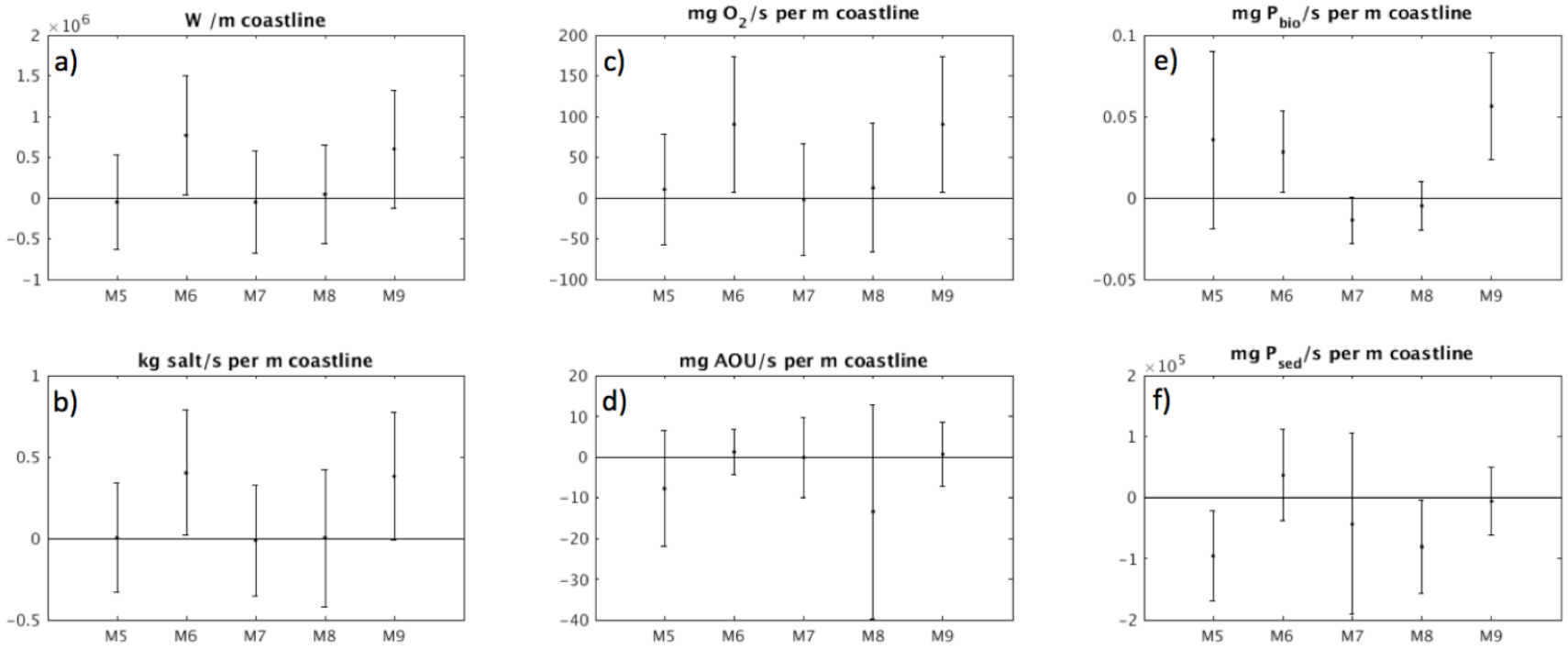

Figure 9. Total fluxes ($\overline{u}\overline{c} + \overline{u'c'}$) of a) heat; b) salt; c) dissolved oxygen; d) AOU; e) phytoplankton; f) sediments. A positive signed covariance represents net particle/oxygen/heat/salt transfer into the nearshore zone, and a negative value denotes the reverse. Errorbars show the standard error.

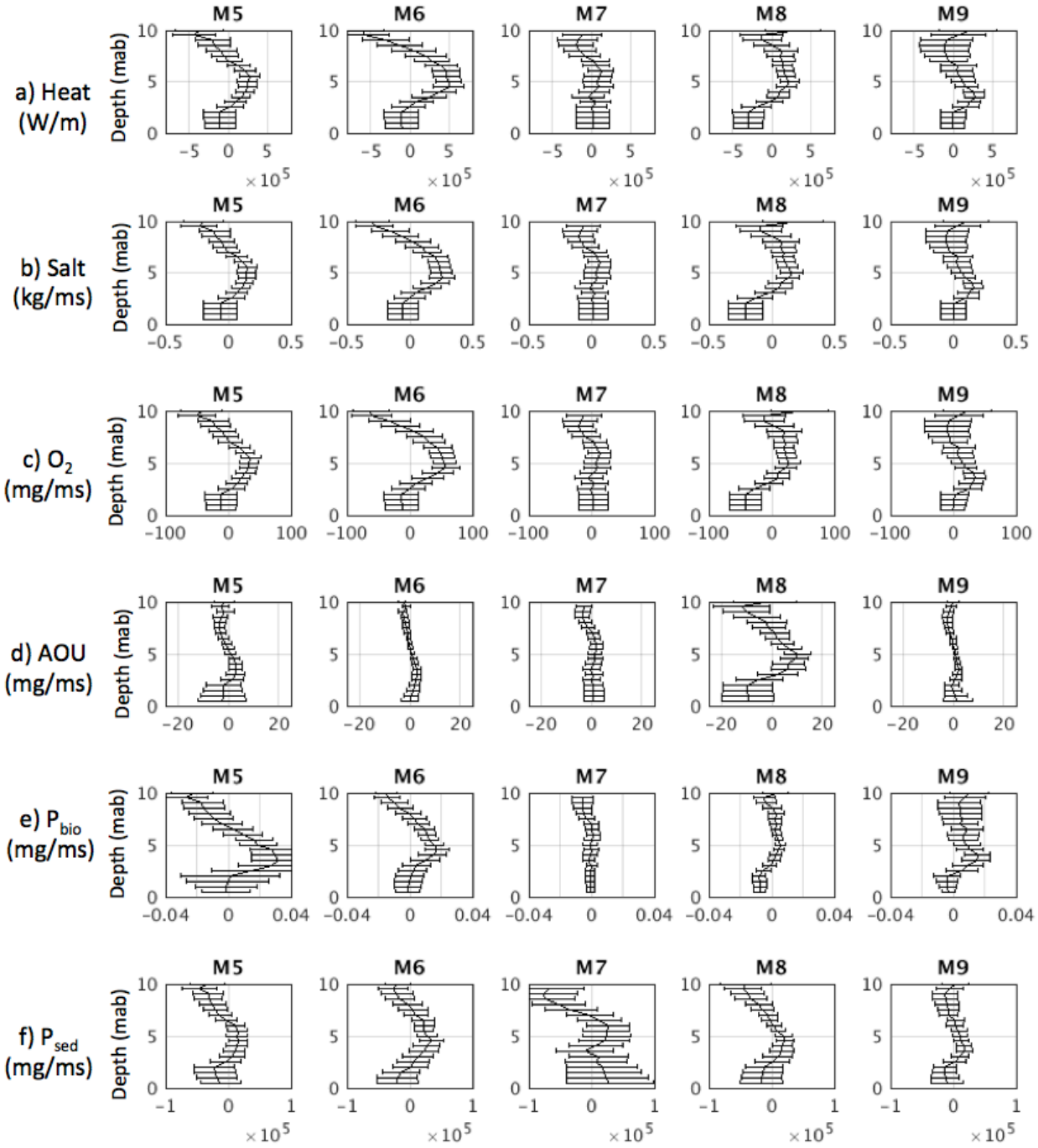

Figure 10. Depth-distribution of total fluxes ($\overline{u}\overline{c} + \overline{u'c'}$) for each mission. a) heat (W/m); b) salt (kg/s per m of coastline); c) dissolved oxygen (mg/ms); d) AOU (mg/ms); e) phytoplankton (mg/ms); f) sediments (mg/ms). A positive signed covariance represents net particle/oxygen/heat/salt transfer into the nearshore zone, and a negative value denotes the reverse. Errorbars are standard errors.

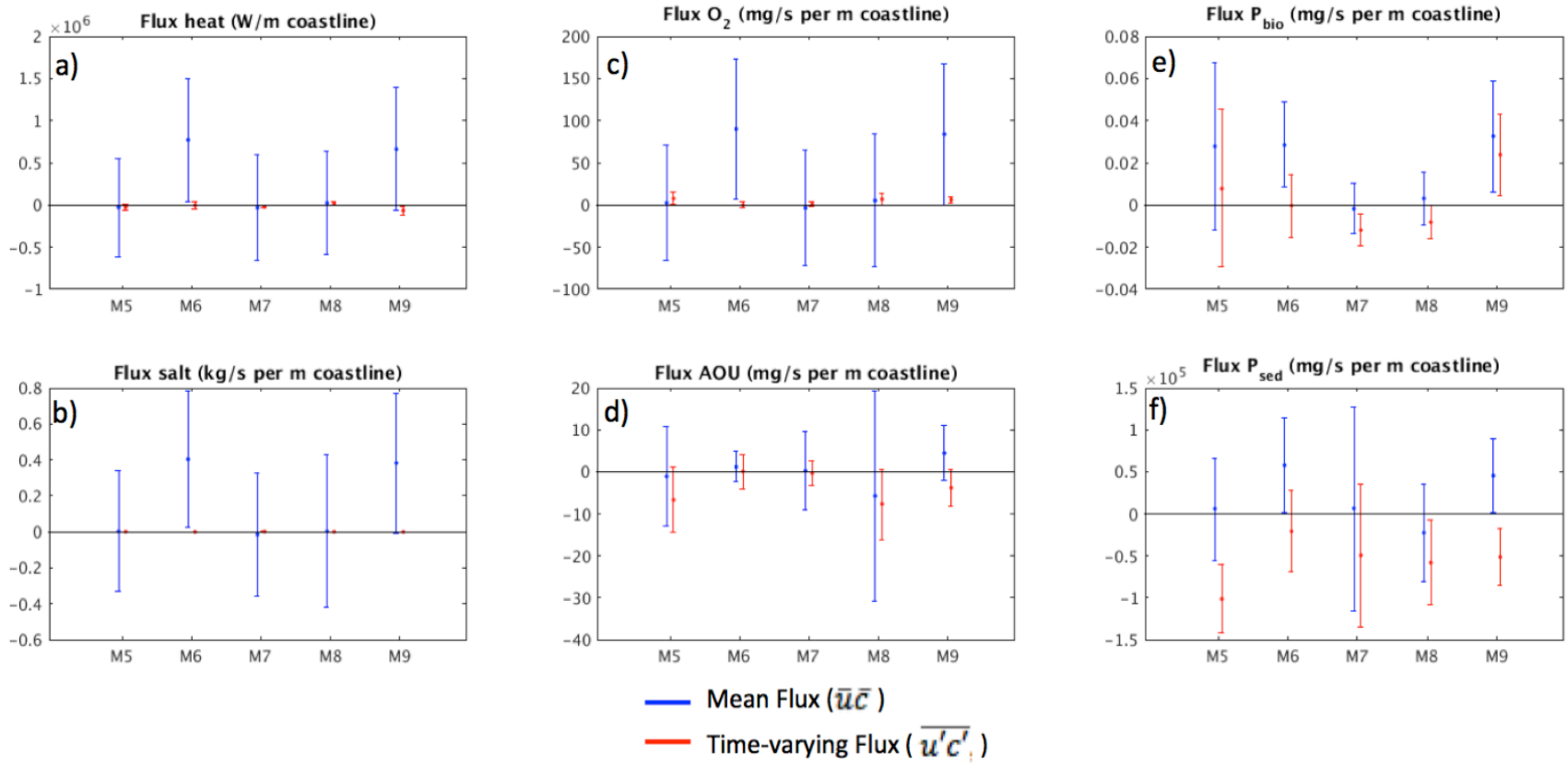

Figure 11. Contribution of mean and time-varying fluxes to total fluxes of a) heat; b) salt; c) dissolved oxygen; d) AOU; e) phytoplankton; f) sediments. A positive signed covariance represents net particle/oxygen/heat/salt transfer into the nearshore zone, and a negative value denotes the reverse. Errorbars show the standard error.

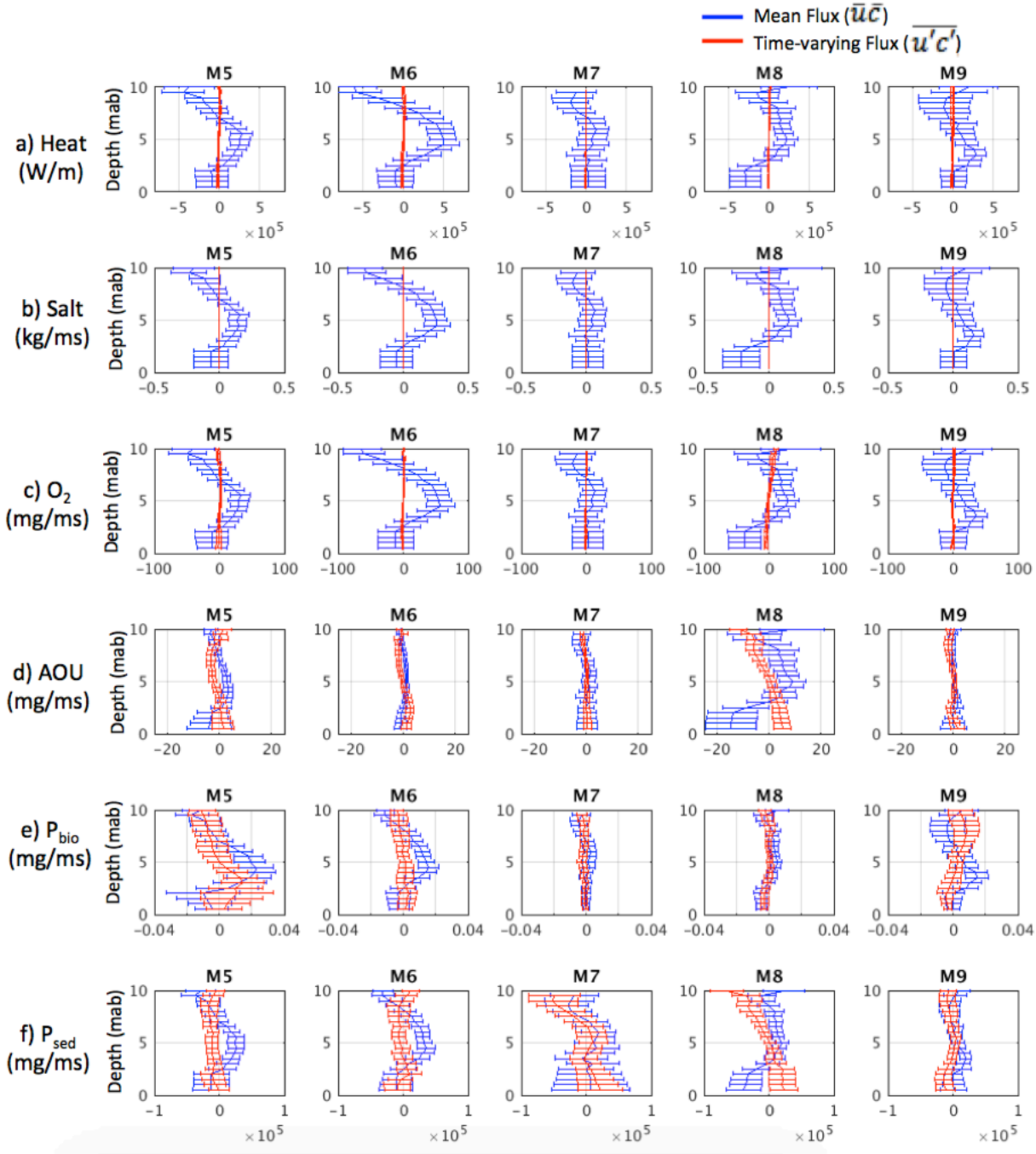

Figure 12. Depth-distribution of mean (blue) and time-varying fluxes (red) for each mission. a) heat (W/m); b) salt (kg/s per m of coastline); c) dissolved oxygen (mg/ms); d) AOU (mg/ms); e) phytoplankton (mg/ms); f) sediments (mg/ms); A positive signed covariance represents net particle/oxygen/heat/salt transfer into the nearshore zone, and a negative value denotes the reverse. Errorbars are standard errors.

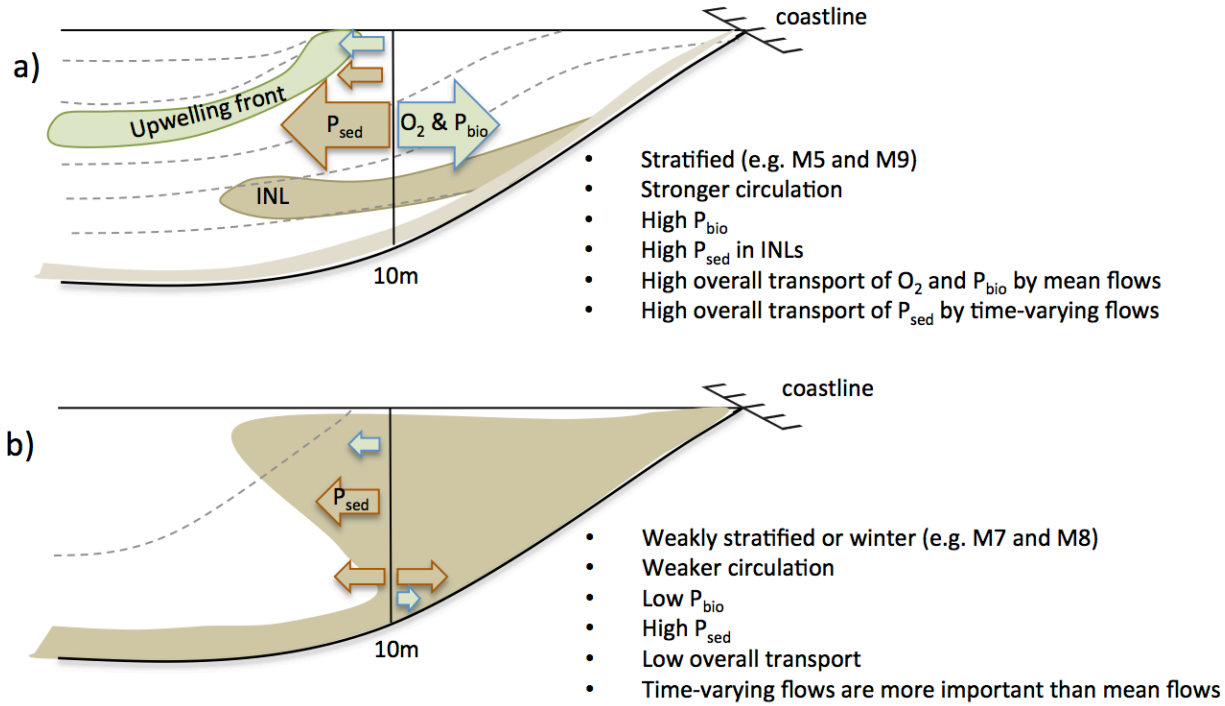

Figure 13. Schematic for cross-shelf transport of sediments, phytoplankton and oxygen during two contrasting ocean states: a) stratified and productive conditions like the observed during M5 and M9; b) weakly stratified conditions characteristics of winter such as the observed during M7 and M8. The size of the arrows represent differences in the magnitude of fluxes, and are for illustration purposes only.

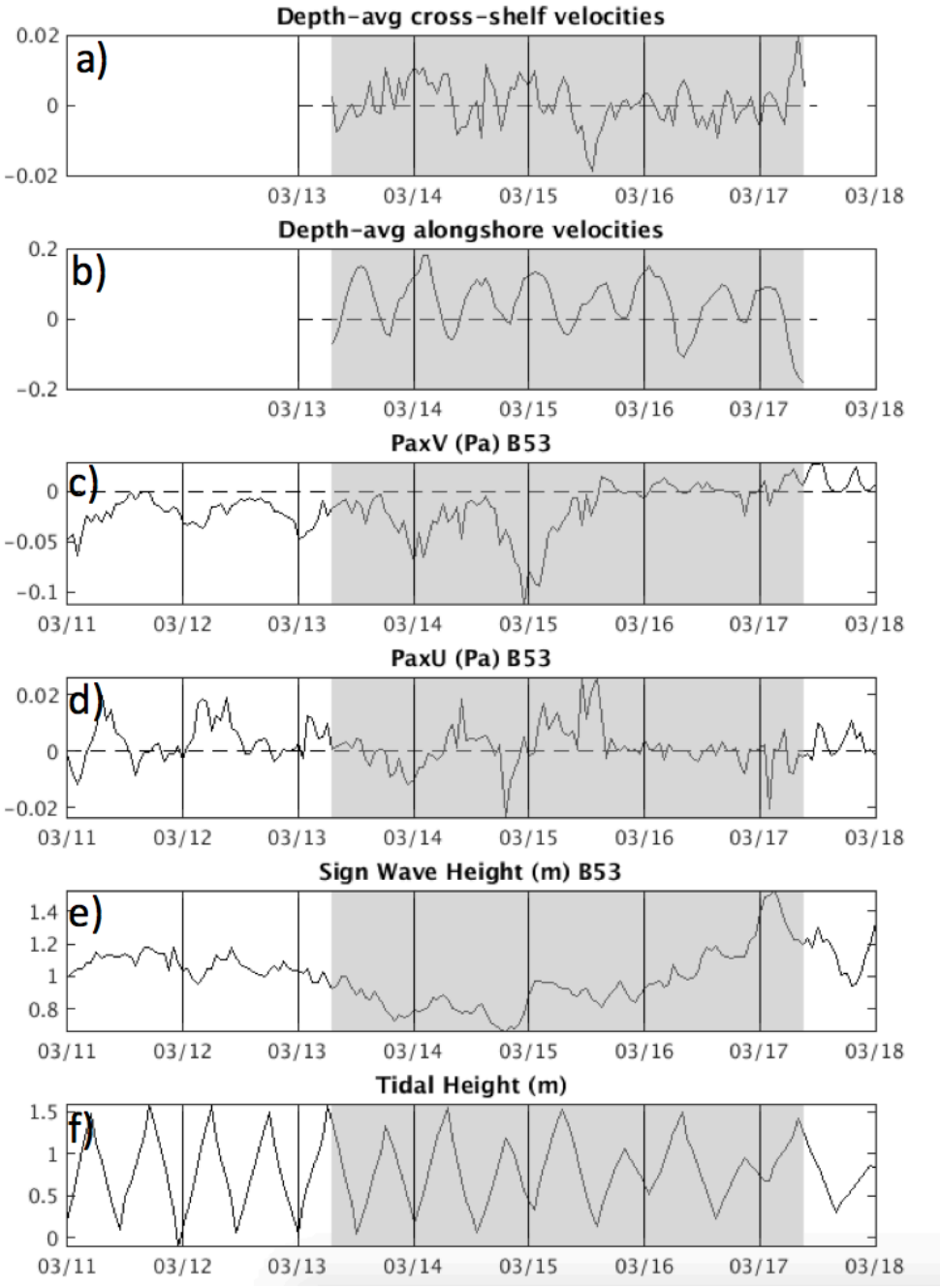

Figure 14. Environmental conditions during the case study mission M8b, in March 2013; a) depth-average cross-shore velocities at the Mohawk Mooring; b) depth-average alongshore velocities (positive velocities are towards east/equatorward); c) Principal axis of wind stress (along-channel; negative values are upwelling-favorable) d) Secondary axis of wind stress (cross-shore; positive values are onshore); e) Significant wave height from Goleta Buoy 46216 (~7km southwest of the glider experiment); f) Tidal height. All data were averaged every hour. Grey area is the period used in this analysis (where integrated cross-shore volume flux approximated zero).

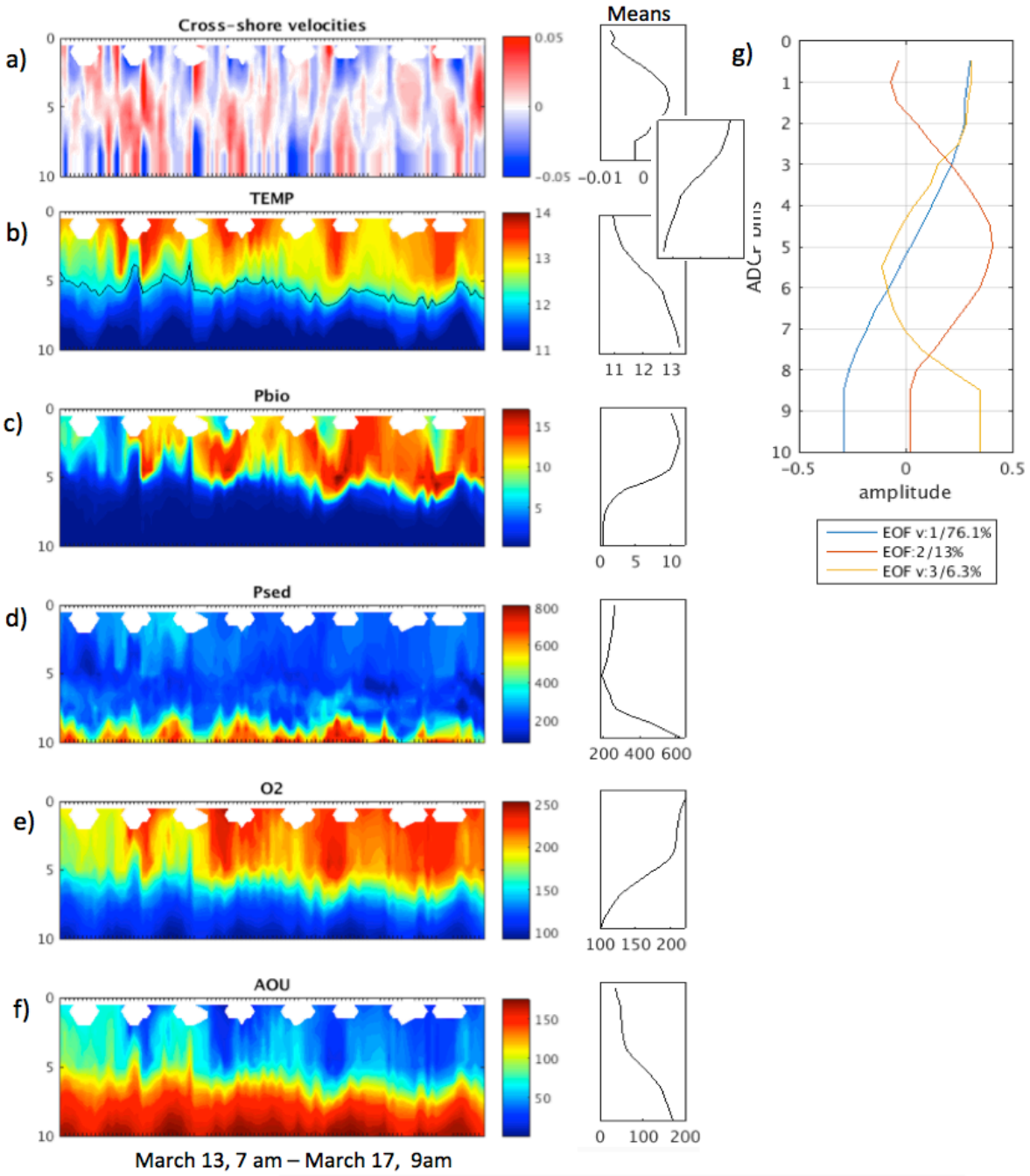

Figure 15. Depth–time evolution and mean vertical profiles of a) cross-shore velocities; b) estimated temperature profiles at the 10m isobath (°C); c) estimated P_{bio} (mg/m^3); d) estimated P_{sed} (mg/m^3); e) estimated O_2 (µmol/l) f) estimated AOU (µmol/l); g) EOF analysis for cross-shore velocities. Hourly tick-marks are shown along the x-axis number of profiles = 89). The depth of the 25.5kg/m^3 isopycnal is shown in black with temperature profiles. The original virtual mooring data collected at the ~42m isobath can be found in Appendix D.

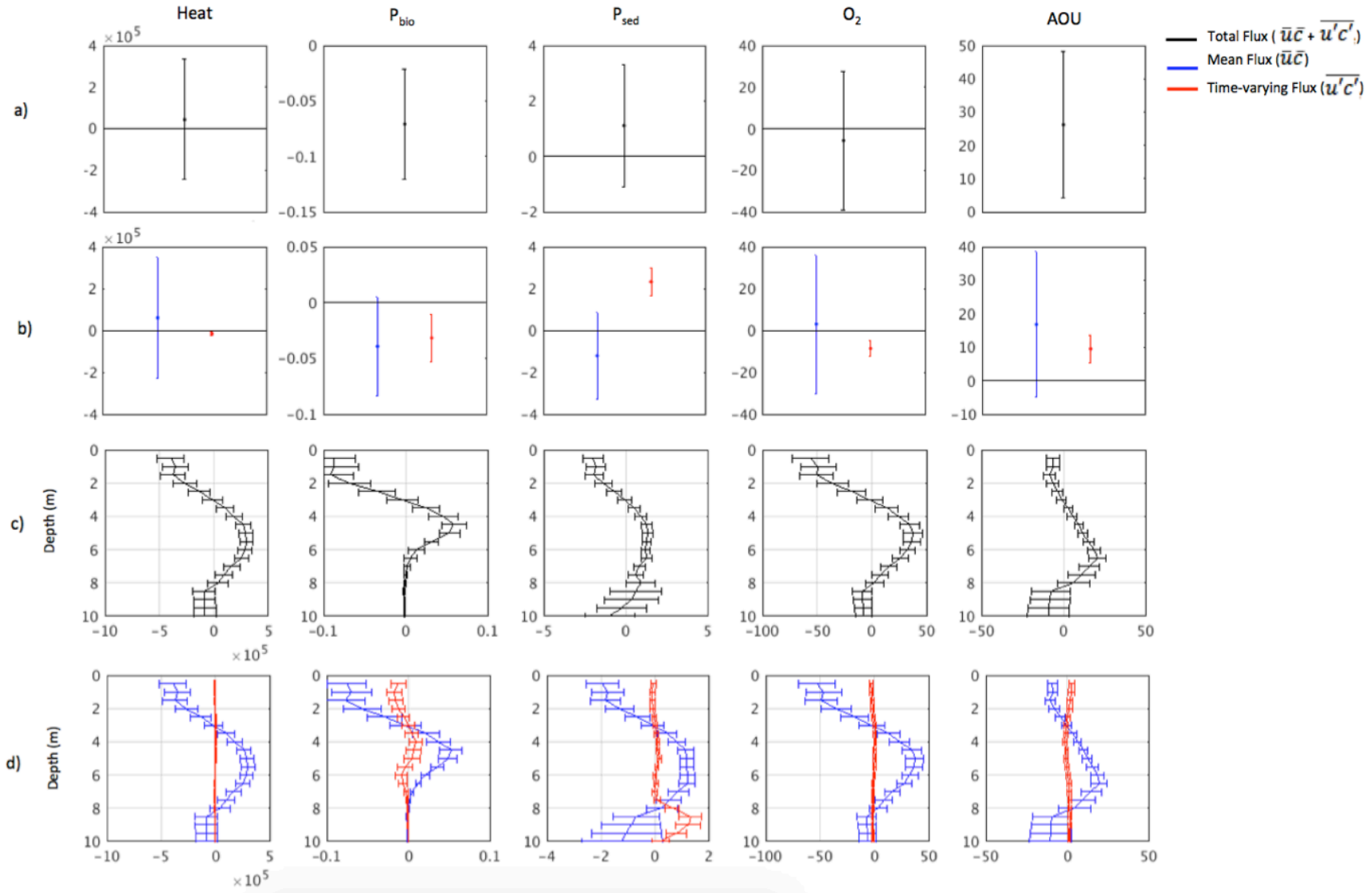

Figure 16. a) Total fluxes of heat, P_{bio}, P_{sed}, dissolved oxygen and AOU; b) contribution of mean and time-varying terms to total fluxes; c) depth-distribution of total fluxes; d) depth-distribution of mean and time-varying fluxes.

APPENDICES

Appendix A: matlab code for optode calibration

(http://people.eri.ucsb.edu/~fernanda/Thesis/)

APPENDIX B. Power spectra for the different mission lengths (using high-frequency ADCP data)

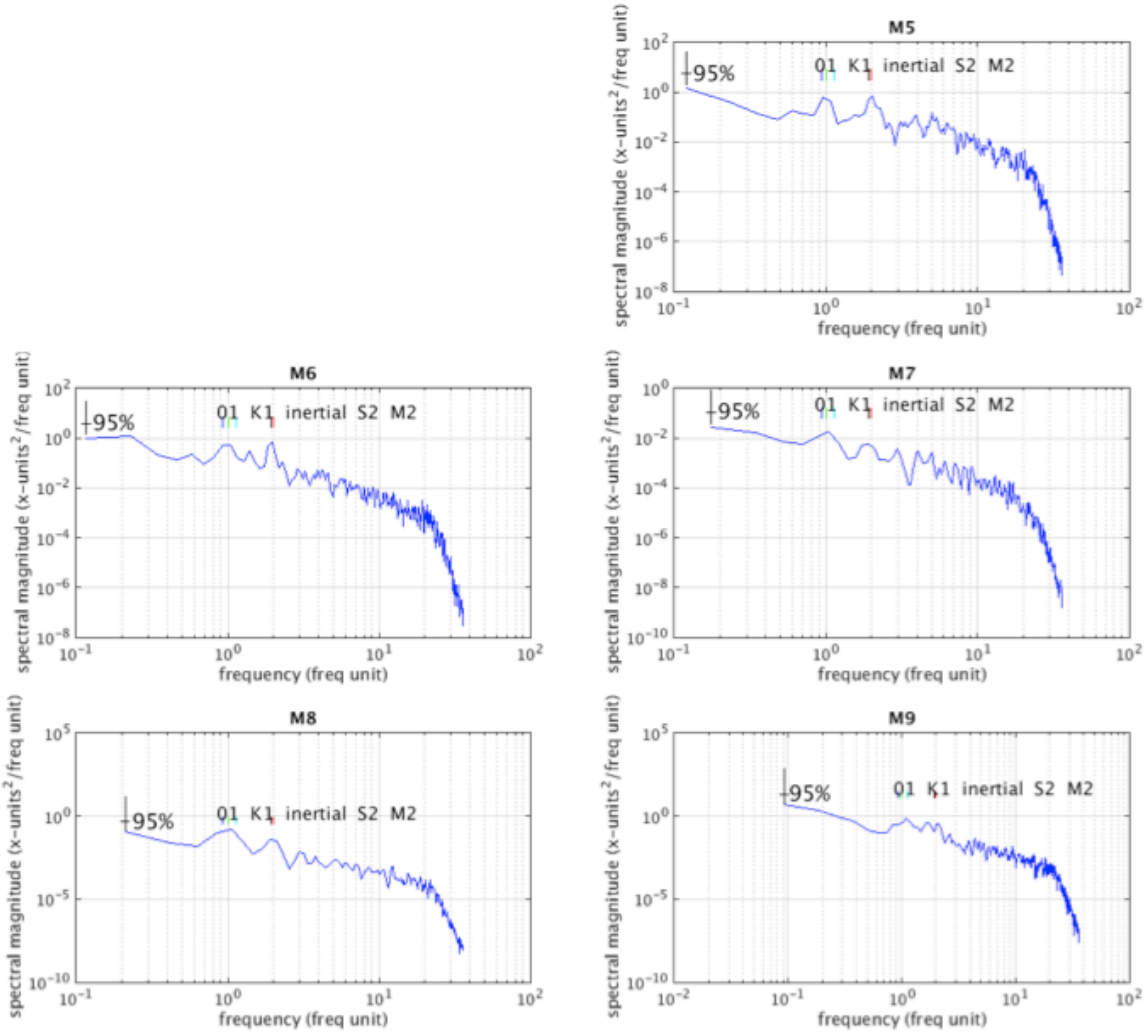

APPENDIX C. ADCP profiles at the 10m isobath and glider profiles at the 42m isobath. a) cross-shore velocities and means; b) temperature (°C); c) P_{bio} (mg/m^3); d) P_{sed} (mg/m^3); e) O_2 (µmol/l) f) AOU (µmol/l); g) EOF analysis for cross-shore velocities. Hourly tick-marks are shown on the x-axis (number of profiles = 99). The depth of the 25.5kg/m^3 density line is shown in black with temperature profiles. Notable diurnal cycles in temperature, P_{bio}, oxygen and AOU are observed.

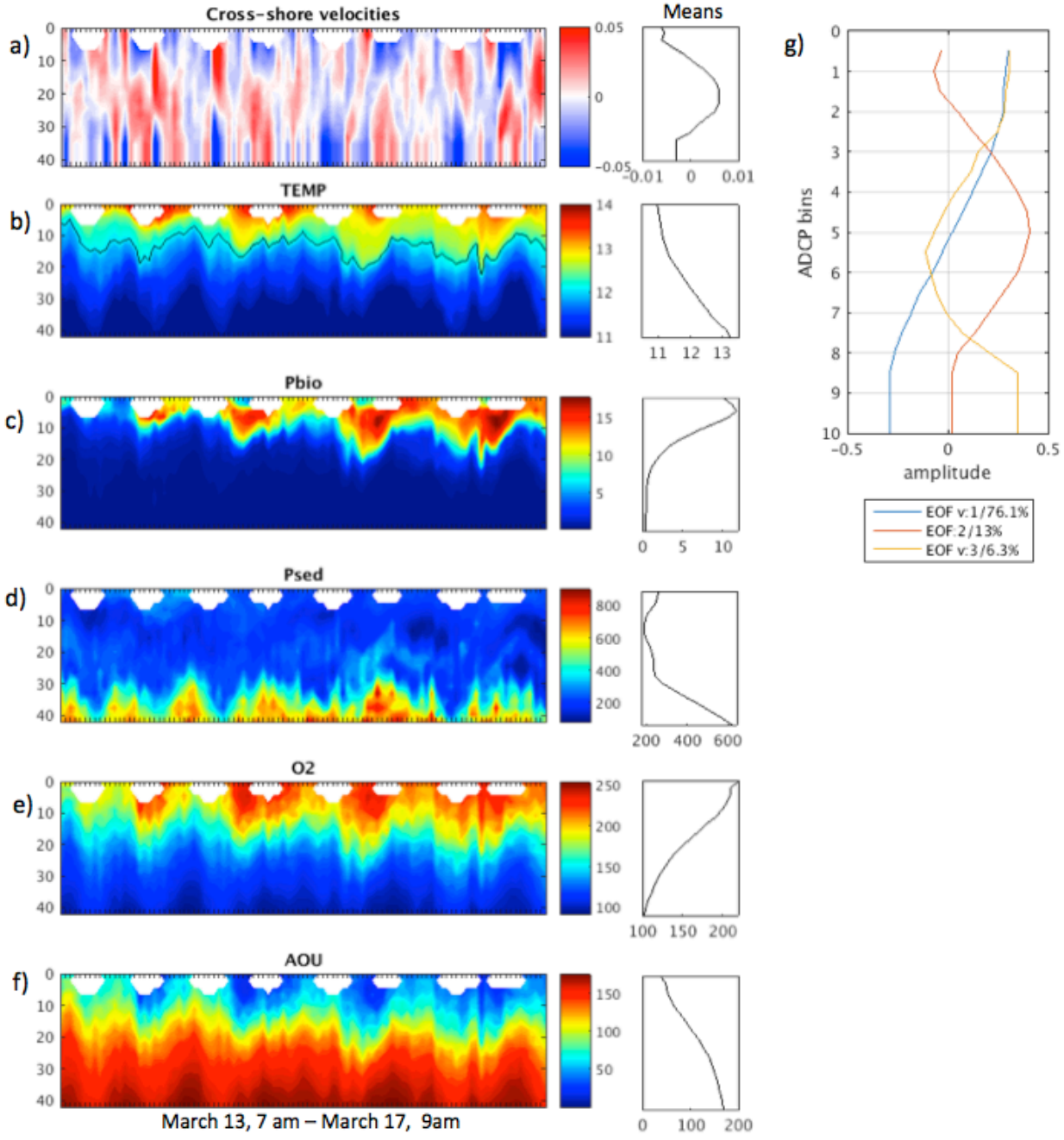

APPENDIX D (Below) a) Total fluxes of heat, P_{bio}, P_{sed}, dissolved oxygen and AOU; b) contribution of mean and time-varying terms to total fluxes; c) depth-distribution of total fluxes; d) depth-distribution of mean and time-varying fluxes. Data used for flux calculation was not extrapolated to the 10m isobath through density surfaces. Instead, 20 glider bins at 42m depth were directly linked to the 20 ADCP bins at the mooring site (i.e data in Appendix D). This assumes that vertical profiles at 10 and 42m isobaths are coherent.

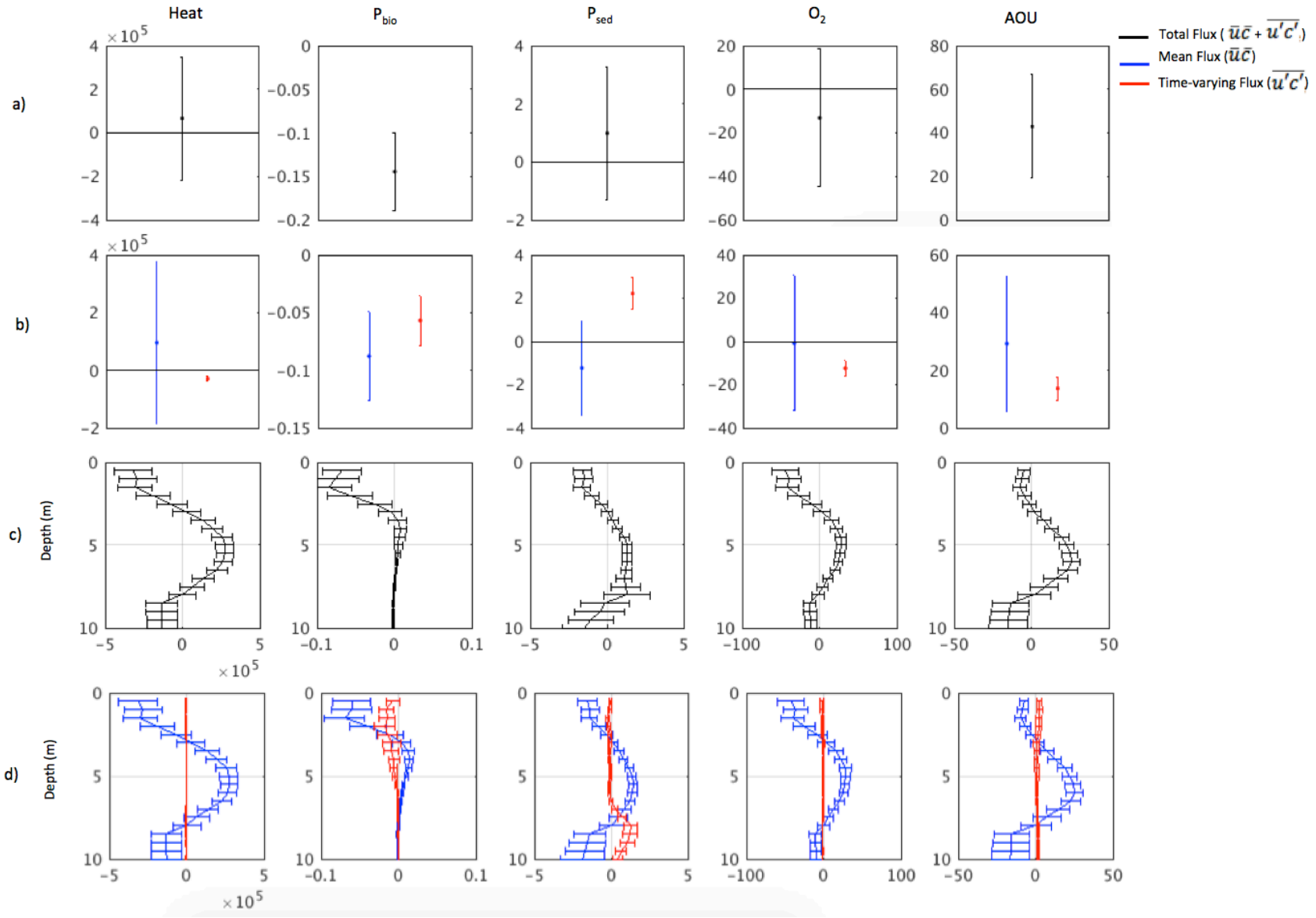
Heat
P_bio
P_sed
O_2
AOU
Total Flux ($\bar{u}\bar{c} + \overline{u'c'}$)
Mean Flux ($\bar{u}\bar{c}$)
Time-varying Flux ($\overline{u'c'}$)
a)
b)
c)
d)
Depth (m)
Depth (m)
×10^5

CHAPTER THREE

Satellite assessments of particulate matter and phytoplankton variations in the Santa Maria Basin and Southern California Bight

Abstract

Satellite observations of chlorophyll (CHL) and optical backscattering coefficients (BBP) in the California Current System are often described in terms of CHL responses to regional upwelling and BBP responses to episodic inputs from storm runoff. Here we show however that surface waves have a larger role in controlling BBP than previously considered, and also describe how SST and wind conditions affect CHL determinations in different portions of the Santa Maria Basin and Southern California Bight. More than 13 years of 2-km resolution SeaWiFS, MODIS and MERIS satellite imagery spectrally-merged with the Garver-Siegel-Maritorena bio-optical model were used to assess the relative importance of various physical forcings in controlling changes in chlorophyll and particle load throughout the domain. The space-time distributions of BBP and CHL estimates from the model were analyzed using Empirical Orthogonal Function analysis, and patterns were compared with several environmental variables. Analysis revealed that CHL blooms in the Southern California Bight occur in phase with SST minima, usually in early spring, while

CHL blooms in the Santa Maria Basin lag SST minima and occur simultaneously to the largest equatorward winds every year, often in the summer. Connections among CHL changes and El Niño and Pacific Decadal Oscillation were also found, illustrating the wide range of processes that likely interact to affect CHL variability over various time/space scales. Tight coupling between BBP and CHL variability is seen in offshore areas, as expected for productive waters. However, values of BBP in a band of variable thickness near the coast are primarily modulated by surface waves. The relationship with waves holds throughout all seasons and often extends offshore until about 100m in depth. Riverine inputs are associated with elevated BBP near the coast mostly during the larger El Nino events of 1997/1998 and 2005. The implication of surface waves determining BBP variability beyond the surf zone has large consequences for the life cycle of many marine organisms, as well as for the interpretation of remote sensing signals near the coast.

1. Introduction

The California Current System (CCS) is the equatorward eastern boundary current of the North Pacific, connecting the eastward flowing west wind drift in the north (~50N) to the westward flowing North Equatorial Current in the South (~20N) [*Hickey*, 1979; *Strub et al*., 1990]. Eastern boundary regions such as the CCS are known for their high coastal productivity due to upwelling processes that advect nutrients into the euphotic zone [*Hill et al.*, 1998]. In these regions, the input of nutrients from other sources such as river runoff or the solubilization of previously deposited nutrient-laden sediments is considered small compared to inputs from oceanic processes [e.g., *Warrick et al*., 2005; *Brzezinski et al*.,

2013]. River discharge and re-suspension can, however, significantly affect the biogeochemistry and optical properties of the upper water column in nearshore waters and near river mouths [*Otero and Siegel*, 2004; *Warrick et al*., 2005]. In this study, patterns and sources of changes in satellite-derived bio-optical properties (specifically particle backscatter, a proxy for suspended particles, and chlorophyll concentrations, a proxy for phytoplankton abundances) over a 13-year period are assessed for an area which encompasses different biogeographic regions such as the Santa Maria Basin (SMBasin) and the Santa Barbara Channel, in the northernmost portion of the Southern California Bight (SCBight; see Figure 1).

Ocean circulation is complex in the northern portion of the Southern California Bight [e.g., *Harms and Winant*, 1998; *Bray et al*. 1999]. Large-scale wind systems force latitudinally dependent seasonal processes that are often disrupted by El Niño and La Niña conditions, with coastal topography imposing local variation on these patterns [*Legaard and Thomas*, 2006]. Winds throughout the CCS are generally equatorward and upwelling-favorable along the entire coastline [*Dorman and Winant*, 1995]. North of Point Conception (PC; 34.4°N), upwelling favorable winds are more consistent and drive offshore Ekman transport from spring to fall [*Harms and Winant*, 1998]. South of Point Conception, the transition from a North-South coastline to the East-West alignment of the Santa Barbara Channel and overall sheltering effect of the Southern California Bight results in weaker upwelling periods throughout the year compared to the area north of PC [*Dorman and Winant*, 1995].

The Santa Barbara Channel (SBC) is thus an important transition zone that, over large scales, receives inputs from both the California Current (cold, nutrient-rich) and Southern

California Countercurrent (warm, nutrient-poor) (Figure 1). During summer and fall, a cyclonic flow driven from a balance between poleward pressure gradient forces and equatorward wind stress is a recurrent feature of the SBC [*Harms and Winant* 1998]. These flows drive poleward currents along the mainland and equatorward currents along the northern Channel Islands, often closing to form eddies that last from days to weeks [*Nishimoto and Washburn*, 2002; *Brzezinski and Washburn*, 2011]. During very strong upwelling periods, equatorward winds are able to disrupt the cyclonic flow and currents become equatorward throughout the entire channel. Episodically, the circulation may also completely reverse and show poleward patterns during spring and winter [*Harms and Winant*, 1998; *Melton et al*., 2009].

Runoff associated with strong storms becomes an important source of fresh water, sediments and nutrients to the nearby ocean in the winter into early spring. The Santa Clara, Ventura and Santa Ynez rivers are the major drainage systems in the area, but intense discharge is brief and highly intermittent. For instance, over half of runoff at the Santa Clara River, the largest in the area, occurs in less than 1% of the time (~3 days a year), and, during much of the year (70% of the time), discharge is negligible [*Warrick*, 2002; *Warrick et al*., 2005]. *Warrick et al*. [2004] showed that sediments settle very rapidly within ~1 km of the river mouth, being further transported along and across the continental shelf through nepheloid layers. The importance of riverine discharge in determining optical properties in nearshore waters compared to other mechanisms such as particle re-suspension and cross-shelf transport are not well determined.

Questions also remain on the physical drivers of phytoplankton changes over similar time and space scales in these dynamic waters. The complex circulation patterns of the CCS

affect the distribution and variability of phytoplankton in the domain beyond the regional upwelling effects. For instance, upwelled waters north of Point Conception typically flow south and enter the SBC, force eddy formations, and promote primary productivity in channel [*Hayward and Venrick*, 1998; *Brzezinski and Washburn*, 2011]. However, decoupling and non-linearity between changes in sea surface temperature, nutrient inputs and wind conditions and their response to biological productivity is common, especially in nearshore coastal waters [e.g. *Kim et al.*, 2009; *Santoro et al*., 2010] or when associated to harmful algal bloom episodes [*Kudela et al*., 2010]. Inter-annual variability in phytoplankton patterns is generally attributed to climatic variables such as El Niño [e.g. *Kahru and Mitchell*, 2001; *Kahru et al*., 2015], but long-term stable datasets capable of appropriately investigating trends are still lacking.

Satellite observations of ocean color have emerged as important tools to detect spatial-temporal trends in bio-optical properties due to their improved temporal frequency and spatial coverage compared to traditional ship-based sampling. Ocean color sensors such as SeaWiFS, Aqua-MODIS and MERIS have sampled the Earth on and off since 1997, with global coverage every 1-2 days, clouds permitting, and spatial resolution of around 1 km. In this chapter, 13 years of satellite and field estimations of sea-surface temperature (SST), optical backscatter (BBP) and chlorophyll concentrations (CHL) are summarized for a portion of the Santa Maria Basin and Southern California Bight, and their general patterns of variability are resolved over time and space. The existence and implications of long-term trends in the signals are assessed. Potential environmental controls that affect chlorophyll and backscatter variability over different time scales and different portions of the domain are identified and discussed. Sources of deviation in the chlorophyll: backscatter co-variability

in coastal and open waters are assessed. This analysis will help diagnose issues in satellite algorithms and improve understanding and interpretation of ocean color products.

2. Data and Methods

2.1 Satellite data and validation

All daily Level-2 normalized water-leaving radiance data from SeaWiFS (1.1km resolution; reprocessing 2010), Aqua-MODIS (1km resolution; reprocessing 2013) and MERIS (1km resolution; reprocessing 2013) satellites from 1997 to 2010 with at least partial cloud-free views of the Santa Maria Basin and Southern California Bight were used in this study (http://oceancolor.gsfc.nasa.gov/). All standard Level-2 flags were applied. Normalized water-leaving radiances from all sensors were spectrally merged using the Garver-Siegel-Maritorena (GSM) semi-analytical bio-optical model [*Maritorena et al.*, 2002; *Maritorena and Siegel*, 2005; *Maritorena et al*. 2010] to retrieve single estimates of chlorophyll concentrations (CHL; mgm^{-3}), combined detrital and dissolved absorption coefficients at 443nm (CDM, a_g443+a_d443; m^{-1}), and particulate backscattering coefficients at 443nm (BBP, $b_{bp}443-b_{bw}443$, where $b_{bw}443$ is from Smith and Baker, 1981; m^{-1}). Spectral merging techniques increase daily spatial coverage and provide lower uncertainties in retrieved variables [*Maritorena and Siegel*, 2005]. All daily merged CHL, BBP and CDM data were re-mapped to a 2-km resolution grid, and presented as 8-day composites to increase spatial coverage. 1-km sea-surface temperature data (SST; remapped to 2-km grids) was obtained from MODIS-Aqua from 2002-2010 and used as a proxy for changes in physical ocean conditions during this period.

Prior to merging, remote sensing reflectances [$R_{rs}(\lambda)$] and GSM-derived CHL, BBP and CDM retrievals from all individual daily Level-2 images of each satellite were validated against the extensive *in situ* dataset from the Plumes and Blooms (PnB) program, which consists of monthly day-long cruises along 7 stations within the Santa Barbara Channel and has been in activity since 1996 (See Figure 1; http://www.eri.ucsb.edu/research/groups/plumes-and-blooms). *In situ* data used include near-surface measurements of BBP at 442nm from a HOBI Labs Hydroscat-6 instrument, and fluorometric chlorophyll and dissolved absorption spectra from water bottle samples, and remote sensing reflectances from a PRR instrument. Details of field measurements methods and data used are provided in *Toole and Siegel* [2001], *Kostadinov et al*. [2007, 2012] and *Barrón et al*. [2014].

Satellite matchups with the field data were made using cloud-free 3x3 neighborhood pixels of individual Level-2 images sampled at the nominal PnB locations within the same day of image acquisition. Spectral matchups were created only when no negative R_{rs}(412nm) values were found, since negative R_{rs}(412) values are thought to occur due to an over atmospheric correction in regions with high amounts of absorbing aerosols [*Gordon*, 1997; *Bailey and Werdell*, 2006]. Relevant statistics between $R_{rs}(\lambda)$, GSM products and field datasets for each of the three satellites are shown in Table 1.

Comparisons of $R_{rs}(\lambda)$ with radiometric PnB field measurements illustrate the difficulty in validating satellite ocean color products in complex environments (Figure 2). Overall, relationships between field and satellite $R_{rs}(\lambda)$ measurements are similar for all satellites, with wavelength 412nm showing the worst results throughout (a reflection of aerosol contamination effects). Satellite observations consistently underpredict the field

observations of remote sensing reflectances. The comparison between field CHL and satellite data is encouraging, with R^2 values around 0.5 for all satellites. Satellite and field BBP observations show good correspondence, especially for SeaWiFS (R^2=0.39). The performance however is not as good for CDM, especially for SeaWiFS and MERIS satellites. While satellites underpredict CHL estimates, they overpredict CDM and BBP observations. The poor performance for CDM is expected due to uncertainties in the blue-violet bands used in the retrieval of CDM due to poor atmospheric correction, as well as the unusual color dissolved organic matter (CDOM) dynamics at this site where only weak relationships are found between CDOM absorption characteristics and either salinity or phytoplankton biomass indices [*Barrón et al*., *in prep*]. Thus, in this study only CHL and BBP data products, in their merged form, will be used.

2.2 Environmental Forcings

Selected local and remote environmental factors are used to assess controls on space-time variability of physical and optical properties. Significant wave height, wind speed, and wind stress are used from NDBC buoy 46054 (http://www.ndbc.noaa.gov/station_page.php?station=46054; Figure 1) within the Santa Barbara Channel as rough indices for mixing, upwelling and relaxation conditions. Wind stress was calculated following *Edson et al.* [2013], and rotated into principal axis coordinates, such that by convention negative values refer to upwelling favorable winds [*Brzezinski and Washburn*, 2011]. Wind and wave variables were averaged ± four days around the mean time of each merged satellite image, but daily averages are also shown and discussed when necessary since shorter time-scale changes in wind and waves might control

episodic changes in optical properties. A 140-day gap in significant wave height data at buoy 46054 in 2002, as well as shorter gaps in wind data in 2002, 2005, 2009 and 2010, were filled through linear regression of the available wave heights and wind data from this buoy and NDBC buoy 46053 (mid-SBC channel; waves and winds at the two locations are well correlated, r=0.85 and r=0.64, respectively; wave height and wind data at buoy 46053 were available during the gap periods). In the absence of complete discharge records from the Santa Clara River, stream discharge for the Ventura River (VR; USGS gauge station 11118500 at www.waterdata.usgs.gov/nwist/rt) is used as an index for fresh water input and sediment fluxes entering the SBC [*Warrick et al*., 2004]. Linear correlations between Ventura and Santa Clara River discharges for the ~7 year period where coincident data exist (1997-2004) are good (r=0.89). Discharge data is shown as accumulated discharge every 8 days to match satellite sampling.

Monthly values of the NOAA's Southern Oscillation Index (SOI) and Pacific Decadal Oscillation (PDO) index (http://www.esrl.noaa.gov/psd/data/climateindices/list/), as well as the North Pacific Gyre Oscillation index [NPGO; *Di Lorenzeo et al*., 2008; http://www.o3d.org/npgo/npgo.php] are used as climatic-scale variables that may influence physical and optical variability in the area. Index values were linearly interpolated to match the 8-day periods of satellite composites. Extreme negative SOI values denote warm, El Niño-like conditions. PDO and NPGO are indicators of long-term changes in sea surface temperatures and circulation patterns, respectively. Large positive PDO values indicate warm eastern North Pacific waters. Positive NPGO values indicate a strong North Pacific gyre and stronger North to South transport along the California Current, while negative values indicate a weak gyre and decreased southward transport (see Appendix A for

information on their calculation). 8-day Photosynthetically Available Radiation data (PAR) from SeaWiFS (9-km resolution; data available at http://oceandata.sci.gsfc.nasa.gov/SeaWiFS/Mapped/8Day/9km/par/) from 1997-2002 and MODIS (4-km resolution; data available at http://oceandata.sci.gsfc.nasa.gov/MODISA/Mapped/8Day/4km/par/) from 2002-2010 are used to retrieve the shape of the seasonal cycle. PAR data were re-sampled to 2-km resolution to match merged bio-optical data.

3. Results

3.1. Mean spatial distributions of SST, BBP and CHL

Spatial means of SST, CHL and BBP illustrate the mean physical and bio-optical features of the domain. SST mean patterns in Figure 3a are consistent with the regional circulation patterns where colder waters from the California Current System enter the SBC from north of Point Conception, while warmer waters from the Southern California Bight dominate waters in the southern region of the SBC. Standard deviations are smaller in the Santa Maria Basin and further offshore than in the Southern California Bight (Figure 3b), reflecting the seasonal propagation of SCBight waters along the coast.

The highest CHL concentrations are found in the center of the Santa Barbara Channel, north of Point Conception, within the coastal upwelling region of the California Current System (up to San Nicholas Island) and along the mainland, where the flow is often poleward (Figure 3c). CHL patterns in the middle of the SBC channel indicate the

importance of the Santa Barbara Channel Eddy in driving productivity in the region [*Brzezinski and Washburn*, 2011]. The relatively reduced CHL in the vicinities of Points Arguello and Conception are related to the known asymmetry of chlorophyll distributions in coastal upwelling centers, where upwelling plumes are advected offshore by horizontal flows [*Jones et al*., 1988]. Values near land surfaces have higher uncertainty due to possible artifacts such as low pixel coverage due to imperfect cloud and land masks as well as the adjacency effects where bright land reflected radiances are forward scattered into the atmospheric paths of nearby ocean pixels [e.g., *Santer and Schmechtig*, 2000]. Thus, a mask excluding pixels whose coverage were less than 60% over the entire period was overlaid on all images, minimizing the contribution of lower confidence pixel values (Figure B in Appendix). The mask acts as an extension of the coastline over the continent and Channel Islands. Mean CHL estimates are above 1.5mg/m^3 in areas within and north of the SBC (Figure 3c). Standard deviations are generally larger than the mean (Figure 3d), reflecting the seasonal and episodic occurrences of phytoplankton blooms of various intensities. As expected, mean spatial patterns for CHL and SST are complementary, with colder regions within the SBC, north of Point Conception and along the upwelling California Current system showing the largest mean CHL estimates.

Particulate backscatter (BBP) patterns generally mimic the CHL distributions in offshore areas, within the SBC and north of Point Conception. This indicates that, in those areas, the BBP signal is dominated by phytoplankton assemblages (Figure 3e). Along the mainland, however, inputs of materials through rivers and re-suspension of sediments contribute with a larger portion of the BBP signal, with the largest mean BBP values occurring in the vicinity of the Santa Clara and Ventura Rivers in the eastern portion of the image (see Figure 1).

Despite general similarities between the mean fields of CHL and BBP, their standard deviation plots are considerably different (Figure 3f), with the largest changes occurring along the mainland and reflecting the potential roles of seasonal resuspension of particulates and episodic intrusions of terrigeneous materials from creeks and rivers.

3.2 Temporal changes and trends in SST, BBP and CHL

Domain-average changes in SST, BBP and CHL estimates exemplify the role of seasonality and inter-annual variability in driving physical and optical changes (Figure 4). A time-series of domain mean SST (Figure 4a) shows a typical seasonal cycle where the coldest waters occur in early spring due to the onset of upwelling, while the warmest waters are found in late summer and early fall due to seasonal warming and poleward advection of SCBight waters [*Harms and Winant*, 1998; *Otero and Siegel*, 2004]. Regional means of CHL show large inter-annual variations in the amplitude and shape of seasonal cycles, and patterns track fluctuations in SST. The highest mean CHL estimates are found in 2010, when the coolest summers were registered, while the lowest CHL estimates occurred in 1997-1998, during a large El Niño (see Figure 5a). Domain-mean BBP patterns are similar to that of CHL (r=0.80), demonstrating the large role of phytoplankton in determining regional BBP signals. Inter-annual variability however is less pronounced than that of CHL, likely due to the 1997-1998 El Niño years associated with large runoff, which increased BBP estimates compared to CHL at those same years.

Long-term changes in mean physical and optical variables are clearly observed from monthly anomaly ratios (Figures 4d-f). Here, the effects of the annual cycle (which dominates variability) are first removed by calculating the average monthly SST, CHL and

BBP values for each pixel and then using the ratio of monthly values to the mean value of the respective month, as in *Kahru et al*. [2012]. All trend calculations were made by type 1 linear regression and considered significant if within the 95% confidence interval. Trends are significant and positive for both BBP and CHL, but the increases for CHL monthly anomaly ratios are nearly four times greater than those for BBP (0.42% versus 0.11% per year). This suggests again a role for both biogenic and non-biogenic materials in driving BBP. The positive trends in CHL and BBP are accompanied by a negative, although not significantly different from zero, trend in SST determinations (-0.05% per year; p-value=0.28). SST and CHL, and SST and BBP anomaly ratios show a significant and negative relationship with each other (r=-0.36 and r=-0.27, respectively), as expected for upwelling regions.

Spatially, slopes of linear trends shown in Figures 4g-i confirm the general connection between decreased SST and increased CHL and BBP from 1997 to 2010. However, the largest trends in SST and CHL do not coincide over space, with the largest SST decreases observed offshore along the CC; while the largest CHL increases occur closer to the shore, focused in the SBC and SMBasin. Another discrepancy is observed in the BBP trends, where slopes are especially insignificant in those areas where CHL trends are the strongest. These observations suggest decoupling between physical and bio-optical processes at large scales.

3.3 The seasonal cycle of BBP and CHL

While the seasonal cycle of SST in the domain is well determined with maximum temperatures in late summer and coldest temperatures in the spring (Figure 6a), the shapes

of the averaged seasonal cycle of CHL and BBP are comparatively variable, reflecting the range of bio-optical conditions sampled in the domain (Figures 6b-c). Maximum CHL values tend to occur between April and June, when upwelling is the most intense in this region and SST values are at their lowest. The lowest values and lowest variability are found in the winter months, when nutrient, light and mixing conditions are likely less ideal. Maximum BBP values peak between May and June, but variability is large throughout the year. Runoff and mixing episodes contribute with increased BBP variability during winter compared to CHL.

The large variability shown in the CHL and BBP seasonal cycles is partially due to different portions of the domain peaking during different portions of the year. The mean Julian Day of maximum SST, CHL and BBP values for every pixel in the domain plotted in Figures 6d-f supports this observation. As expected, SST changes in the domain are spatially uniform with southern waters peaking slightly earlier in the year (August) than the northern waters (September). CHL in the SCBight, however, peak much earlier in the year, on average, than CHL in the SMBasin (spring vs. summer; Figure 6e), as expected when productivity is associated with seasonal changes in SST. Despite similarities in offshore patterns of CHL and BBP seasonal cycles, large differences occur along the mainland. BBP maximums along the coast (Figure 6f) occur in the first three months of the year, as opposed to the springtime patterns shown in the CHL data.

Spatial differences in the amplitude of the seasonal cycles of SST, CHL and BBP, defined as the maximum minus the minimum estimates for each location of the domain, are also observed (Figures 6g-i). Higher SST amplitudes are found in the SCBight than in the SMBasin, reflecting changes in large-scale circulation patterns (Figure 6g). The highest

seasonal amplitudes in CHL (Figure 6h) occur where the largest blooms are observed, mainly within the SBC and SMBasin, in agreement with mean CHL estimates in Figure 3. The range in BBP is the largest along the coast (Figure 6i), depicting seasonal changes in mixing conditions and sediment inputs. The large variability in shape and phase of the mean seasonal cycles in the domain reflects the range of oceanographic conditions sampled in the region, from oligotrophic areas offshore of the California Current to productive SBC waters and nearshore waters rich in terrigeneous materials. These disparate regions are modulated by different mechanisms during different portions of the year.

3.4 Co-variability between CHL and BBP

The role of mineralogenic and biological particles in controlling BBP variability is seen in plots of the frequency of co-occurrence of BBP and CHL observations. Figure 7a shows that most pixels in the domain contain CHL concentrations lower than 2 mg/m^3 and BBP values less than 0.005 m^{-1}. This is a reflection of the large amounts of clear, offshore waters sampled in the domain compared to highly productive coastal waters. A single fit through all points in Figure 7a yields a correlation coefficient of $r=0.64$ ($p<0.001$). However, episodically high CHL and BBP values tend to follow along two distinct clusters. The first has steep slopes and is characterized by high CHL – low BBP values typical of oceanic areas rich in phytoplankton and poor in mineralogenic materials, while the other has shallow slopes and is characterized by high BBP values and relatively lower CHL values, typical of coastal environments where suspended sediments and detrital materials dominate particulate optical properties [e.g. *Chang and Dickey*, 2001]. The spatial dominance of these clusters is clearly seen in Figure 7b, where mean correlation coefficients between CHL and BBP over

time are plotted for each pixel of the domain. A thin band of low correlation coefficients is shown along the mainland, indicating that in these areas the variability in CHL and BBP are decoupled in time as they are likely governed by different mechanisms. In offshore areas where mean CHL values are relatively high ($\geq$ 1 mg m^{-3}; Figure 3c), the correlation coefficients become stronger (up to r=0.9), suggesting a tighter coupling between processes regulating CHL and BBP changes over time. Further offshore where mean CHL values are less than ~0.2 mg m^{-3} (Figure 3c), correlation values are smaller (r between 0.5 and 0.7) suggesting that other processes, such as photoacclimation of phytoplankton pigment concentrations, are important in this relatively oligotrophic region of the domain [e.g., *Behrenfeld et al*. 2005; *Siegel et al*. 2013].

3.5. Modes of space-time variability in SST, BBP and CHL

Empirical Orthogonal Function analysis was used to help determine the main controls on particle and phytoplankton variability in the domain. EOF analysis partitions the variability of a time evolving dataset into a set of uncorrelated spatial modes and independent, time varying amplitude functions [e.g., *Emery and Thomson,* 1997]. The lower modes explain comparatively larger fractions of the total variance and their patterns in time and space can be compared with simultaneously observed environmental and physical patterns. The analysis was performed on time-mean subtracted and linearly de-trended data. It was noted however that images heavily dominated by clouds led to artificial features on the final EOFs. Thus, prior to this analysis only, those data where clouds occupied a majority of the scene were manually extracted from the time series (8.5% of all images; n=52). Table 2 shows the

correlation coefficients between overall means, EOF amplitude functions and selected local and larger scale environmental forcings.

The first mode of the SST EOF field (Figure 8a) explains 86% of the variance in SST and depicts the mean state of SST variability, while its amplitude function oscillates with the seasonal cycle (Figure 9a). A nearly perfect correspondence between the first SST mode and domain-average SST estimates is observed (r=0.999). The second mode explains 4.4% of the variance in SST and shows a dipole between the warmer and colder waters of the domain (Figure 8b). Together with the east-west gradient observed, the significance of correlations between the SST amplitude functions in Figure 9b and wind stress (r=0.55) characterizes the upwelling-like pattern of this mode. Certainly, a portion of the statistical correlation between mode 2 and wind stress is due to the coherent seasonal cycle that both variables present. If the seasonal cycle is removed, the correlation reduces to r=0.38. The remaining modes explain little of the variability and will not be discussed.

The first CHL EOF explains 27.7% of the variance and is positive everywhere, with largest values occurring in the western SBC and north of Point Conception, and lowest values occurring in the southeastern and southwestern sections of the domain (Figure 8c). Spatial patterns resemble the CHL variability for the domain (Figure 3c-d). As expected, the amplitude functions correlate well with the domain mean CHL values (r=0.93), showing both coherent intra-seasonal (~2 months) and seasonal oscillations. The highest values are found during spring months and the lowest during winter (Figure 9c), with the exception of the winter of 2010.

Extreme positive and negative EOF loadings in the time series often drive the patterns observed and allow better understanding of general EOF features. Thus, Figure 10a-b

highlights the mean CHL values during the extreme 3% lowest and highest amplitude functions for this mode (n=18 each). Although the SCBight and SMBasin are often characterized as highly productive waters, Figure 10a shows that the entire domain appears almost devoid of CHL during portions of the year. When the extreme loadings are mapped over time, the first positive extreme (high CHL) only occurred in the spring of 2000, becoming more common after 2002 (Figure 10g). Only weak correlations are observed between this mode and wind stress (r=-0.34), indicating that wind stress fails to account for almost 90% of Mode 1 variability.

The second EOF mode explains 7.6% of the variability in CHL (Figure 8d) and shows abrupt east-west spatial gradients that separate CHL variability in the SMBasin from variability in the SCBight. Thus, this second mode indicates where in the domain, on average, the largest CHL peaks depicted in the first mode occur: either SMBasin or SBC/SCBight (see Figures 10c-d). The timing of the oscillations between positive and negative amplitude functions (Figure 9d) characterize the seasonal spatial transition between blooms within these two regions during spring and early summer, as Figure 6e also suggested. Seasonally, CHL increases occur in the SBC before they occur in the SMBasin, except during years 2000 and 2003. Temporal transitions between SBC and SMBasin blooms are often very quick, with maximum increases in the two areas separated on average by 45 days (but ranging from 8 to 72 days). Significant correlations are observed between this second mode and SST (r=-0.34), indicating that, to first-order, CHL increases in the SCBight are related to the arrival of cold waters in the domain.

The third EOF CHL mode (Figure 8e) explains only 4% of the variance, but provides additional insights into mechanisms for CHL variability. The negative spatial patterns of

Mode 3 show high values in the western SBC and north of Point Conception, while large positive values are found offshore along the California Current and south of the Channel Islands. Despite similarities with mode 2, extreme negative loadings in mode 3 are stronger within the SBC and occur closer to shore north of PC (Figure 10e). This is consistent with CHL increases associated with upwelling events that lead to the advection of California Current waters into the SBC, fueling phytoplankton productivity within the Channel [*Brzezinski and Washburn*, 2011]. Positive extremes highlight cases when CHL blooms are more evenly distributed along the CC and SBC (Figure 9f). This mode shows the highest significant relationship of any CHL mode with significant wave height (r=0.22), suggesting perhaps a role of vertical mixing and possibly deeper mixed layers in determining the positive mode 3 patterns. The remaining modes explain little of the variance compared to the first three, and will not be discussed.

The first mode for BBP variability (Figure 8f) explains 22.8% of the variability and, as expected, spatial patterns and amplitude functions (Figure 9f) resemble the mean state of BBP distribution in the domain (r=0.80). Spatial patterns are similar to the first CHL mode, with the exception of the coastal zone where a larger portion of the variability is explained by the first BBP EOF mode. Mode 1 is significantly correlated with wind speeds (r=0.37), upwelling-favorable wind stresses (r=-0.37), discharge events (r=0.20) and significant wave height (r=0.12). Correlations remain significant when removing the seasonal cycle from these variables (r=0.18, r=-0.23, r=0.21, and r=0.22, respectively, see Table 3), indicating that these relationships go beyond the natural seasonal variability of the time series. The similarities and differences between the first EOF for CHL and BBP suggest that this first

BBP mode reflects the combination of phytoplankton and, to second-order, non-phytoplankton materials to total BBP variability in the domain.

The second BBP mode explains 12.2% of the variability in optical backscatter, and separates the BBP variability along the mainland from its patterns offshore (Figure 8g). Positive anomalies are found along the entire mainland and around the islands, with the highest amplitudes in the surroundings of river mouths. Thus, this mode corresponds well with mean BBP aggregates within 10-km of the shore (r=0.83; correlations vary slightly if different distances from shore are used). Good correspondence is observed between variations of this mode's amplitude function (Figure 9g) and accumulated discharge at Ventura River (r=0.56), significant wave height observations in the middle of the SBC (r=0.48), and downwelling-favorable winds (r=0.26). Correlations remain significant between this mode and wave height and river discharge values if the seasonal cycle is removed from all variables (r=0.35 and r=0.51, respectively; Table 3). Increases in BBP along the coast (positive amplitude functions) appear associated with decreases in mean CHL (r=-0.40), much like the observed in Figure 7b. Thus, this mode represents the modulation in suspended sediments in the water column due to re-suspension, mixing and discharge episodes.

The third BBP mode explains only 5.2% of the variability in BBP but highlights the importance of the very large episodic storm events in driving changes in BBP across the domain (Figure 8h). The largest negative peak in Figure 9h occurs during the 1998 El Niño event in the vicinity of the Santa Clara and Ventura Rivers, while positive anomalies are generally seen everywhere else along the coast. Correlations remain significant between this

mode, river discharge and waves with and without the removal of the seasonal cycle (Table 2 and Table 3).

4. Discussion

Thirteen years of continuous satellite and field observations provided detailed information on the distribution of BBP and CHL and their variations in the SMBasin-SCBight region. In the following, the limitations, assumptions and artifacts that influence interpretations of the satellite-derived backscatter and chlorophyll concentration observations are addressed for this complex region. Then, the main controls on particle and phytoplankton variability depicted in the EOF analysis are further discussed. Finally, the regional trends in SST, BBP and CHL observed in this study are summarized in the context of larger scales processes such as ENSO.

4.1 Potential issues with satellite data

There are obvious limitations of satellite studies. First, ~90% of the light exiting the water column and sensed by satellites come from the first optical depth [*Gordon and McCluney*, 1975], which in the Santa Barbara Channel is around 10 meters during summer months [*Lewis et al*., 2011]. Additionally, many small-scale fronts, eddies and filaments that are likely important in driving productivity and material dispersal in energetic coastal waters will be largely missed when a 2-km mapped grid is used [see *Romero et al*., 2013]. Clouds, however, are generally the main issues preventing acquisition of quality imagery, and

processes that accompany them such as wind relaxations and winter storms are often missed by satellite ocean color observations. Satellite chlorophyll data from nearshore waters also have systematic and random errors due to the optical complexity of the coastal environment rich in organic and inorganic suspended particles [*IOCCG*, 2000]. Further issues can arise from the adjacency effect where bright land pixel radiances are forward scattered into the atmospheric paths of darker ocean pixels [e.g., *Santer and Schmechtig*, 2000]. The standard Level-2 masks applied to all imagery prior to the merging procedure and the use of only valid pixels after the merging (see Figure B in Appendix) likely minimized some of the above mentioned issues. The impact of time binning and cloud cover in characterizing optical variability in the domain and the potential effect of land proximity in affecting bio-optical observations are addressed below.

All analysis here was performed using 8-day averaged merged ocean color data products [*Maritorena et al*. 2010]. Thus, it is important to assess what proportion of this data was composed of multiple versus single images, information that is especially crucial during the 1997-2002 period where only SeaWiFS data were available. A histogram highlighting these numbers (Figure C in Appendix) shows that during the first 5 years of the time series, almost 40% of the 8-day binned images are made up of a single day image. The merged satellite data shows much improved results, with less than 25% of 8-day bin images made up of a single day image. This confirms not only that merging satellite products improves spatial/temporal coverage, but also that the majority of 8-day bin data, even during the SeaWiFS-only Era, were only partially affected by time binning issues.

Underrepresentation of sediment plumes that develop and decay very quickly in time and are often associated with cloudy conditions is likely to occur when 8-day averages and

2-km grid points are used. Fortunately, discharge records indicate that storm runoff events were not significantly undersampled. Figure 11 shows that all major runoff events are reflected in the second EOF mode for BBP, which represents the relationship between particle loads and terrestrial runoff to BBP near the coast.

The weak relationships between CHL and BBP along the coast shown in Figure 7 could arise if land adjacency and contamination of CHL signal due to high loads of suspended sediments were important factors. Simultaneous field sampling of chlorophyll concentrations and particulate backscattering data from surface waters of PnB stations 1 (~1.5 km offshore; n=92) and station 5 (mid-channel; n=98) were selected to test if the relationships between CHL and BBP observed in the satellite data (Figure 7a) are also present in analysis of the *in situ* data (Figure 12). Indeed, samples closest to the shore show a tendency of high BBP_{PnB}: low CHL_{PnB} estimations when compared with station 5, further offshore, and lower correlation coefficients between the variables. These observations increase the level of confidence in the nearshore satellite-derived BBP:CHL patterns discussed throughout this analysis.

4.2 Waves as major controls on particle distributions in nearshore waters

Satellite BBP determinations were shown to be largely dominated by particles of biogenic origin such as phytoplankton, with overall patterns (e.g. overall space-time means) correlating very well with CHL changes throughout most of the domain (Table 2; Figure 7b). These relationships are also observed locally, with mean BBP changes in the SBC ("SBC-mean" in Table 2) showing good correspondence with *in situ* biogenic silica estimates from Plumes and Blooms measurements [BSi; proxy for the presence of diatoms;

r=0.33; *Krause et al*., 2013], and no significant relationship between satellite-sensed SBC-mean BBP and field observations of lithogenic silica [LSi; associated with inorganic materials; *Toole and Siegel*, 2001]. Correlations between the first EOF mode of BBP variability and these proxies show similar relationships (Table 2), even though Plumes and Blooms data are likely not representative of ocean conditions distant from the SBC. The expected role of mineralogenic particles in determining BBP changes in an optically complex system only appears when considering the second mode for BBP variability, which describes coastal changes in BBP. In this case, good correlations are observed between BBP mode 2 and field estimates of LSi (r=0.44), as well as negative correlations with field BSi (r=-0.18).

The role of episodic runoff in determining variability in oceanic particle loads has been long suggested for the SBC [e.g., *Mertes and Warrick*, 2001; *Otero and Siegel*, 2004]. Recent studies in the SCBight have shown however that other processes, such as re-suspension of sediments associated with the passage of storms and large waves, may have a large role in controlling BBP variations [*Warrick et al*., 2004; *Chapter One* of this dissertation]. Waves are able to not only actively stir the water column and promote particle re-suspension but also create conditions for internal wave breaking in shallower waters, leading to materials being suspended in the water column for extended periods of time [*Cheriton et al*., 2014]. Here, waves are assumed to be a proxy for mechanisms that accompany or lead to the resuspension of materials within the water column. Along and across-shore advection of previously re-suspended material, for instance, is likely a major mechanism resulting in the increases in BBP in offshore areas.

Assessing the relative roles of runoff and wave action in controlling BBP variability in the coastal zone requires partitioning their activities over time and space. The relationships among mean nearshore aggregates of BBP (which correspond well with the second EOF mode amplitude function) and significant wave height and river discharge determinations are shown in Figure 11a-b. Changes in wave height and discharge explain 27% and 43% of the variability in mean nearshore BBP, respectively. Correlations remain relatively strong if the seasonal cycle is removed from all time-series, with wave heights explaining 18% and discharge and 36% of the variability. Spatially, significant correlations among BBP variability and wave height and discharge are found along the entire mainland, as expected from BBP mode 2 patterns (Figure 13a). Correlations between BBP and wave height decrease with distance from shore, in agreement with the increased effect of resuspension processes in shallower waters. Relationships between Ventura River discharge and BBP in Figure 13b show similar spatial patterns, although features are patchier and extend further offshore, particularly in the vicinity of the Santa Clara and Ventura Rivers. This might be a consequence of incomplete sampling of riverine plumes during storm events due to clouds.

Results of a multiple linear regression between significant wave height and discharge explain 57% of the variability in mean nearshore BBP over time (the coefficient of determination between the two variables is 0.0437, and the variance inflation factor $1/[1-R^2]$ is small, ~1; Figure 11d). However, while seasonal changes in BBP nearshore over time (Figure 11a) are largely modulated by changes in significant wave height, the largest BBP increases occur sporadically during extreme discharge episodes, namely during the years 1998, 2001, 2005 and 2008. Conversely, at times, significant changes in BBP appear related to changes in wave conditions alone. During winters of 1999-2000, 2004, 2007 and 2010,

for instance, discharge was negligible but BBP was comparable to those during years with larger runoff (e.g. 2001). Indeed, observations indicate that the explanatory capability of waves remains strong over time and space even in the absence of storms, as shown in the correlations between BBP and surface waves for a subset of data that excludes the top 5% largest discharge episodes of the record (Figure 13c). This is expected as extreme wave conditions occur more regularly and often independently of the very large runoff events (compare Figures 11a-b). Thus, the role of discharge in driving BBP changes along the coast is limited to the very few intense winter storm events in the record.

Waves also appear to capture the initial increases in BBP prior to the large winter storms of 1998 and 2008. During other years, neither discharge nor wave activity explains above-average increases in mean BBP nearshore. High BBP signals during late summer of 2003, for example, occurred during low wave conditions and negligible discharge records, possibly linking these BBP increases to large nearshore phytoplankton blooms. Alternatively, the lack of correspondence between waves and BBP might be related to the 8-day average scales used, since a episodically large and quick wave event might not be well represented by these longer averages. However, the same analysis using the maximum wave heights instead of mean wave heights yielded virtually the same results, since the variables scale well with each other ($r=0.90$). In contrast, in the fall/winter of 2000, increases in wave height conditions led to below-average nearshore BBP estimates. This may be a result of undersampling in the nearshore due to clouds, although the presence of different particle types at different times of the year may also affect temporal variability of BBP and their relationship with mixing processes.

The importance of surface waves in determining BBP variability along the coast has large implications for the modeling of cross-shelf particle transport. The thickness of the coastal band delimited by EOF mode 2, as well as the low correlation coefficient region between BBP and CHL, varies greatly throughout the domain, from ~6km near Point Conception to ~42km in the surroundings of the Santa Clara River. Long-period deep-water waves in this region (i.e. >10s) theoretically have the ability to interact with the bottom over depths larger than 80m (i.e. wavelengths >160m). Indeed, bathymetry records indicate that this coastal band is generally confined to the 100m isobath, the offshore limit where *Drake and Cacchione* [1985] reported that winter storm-induced long-period surface waves transport suspended sediments across the continental shelf (Figure D in Appendix). Nonetheless, the largest correlations between BBP and waves or the lowest correlations between CHL and BBP are most pronounced much closer to shore, and likely become even stronger closer to the shoreline. The 2-km resolution of the satellite data products and land masks limits these interpretations to this point.

The present analysis assumes that surface wave information from a central mooring adequately quantifies the action of waves throughout the domain. This is likely not the case as waves may change characteristics when encountering different coastal orientations and topographies, which might explain the deviations in BBP:CHL values along the coast. High-spatial resolution surface wave information along the coast would be necessary to more thoroughly address these specific considerations. Nonetheless, the implication of waves determining BBP variability beyond very shallow waters may have important consequences for many marine organisms, as well as for the interpretation of remote sensing signal near the coast.

4.3 Space-time components of spring/summer blooms

The upwelling of cold, saline, nutrient-rich waters associated with strong equatorward winds is considered the main mechanism driving primary productivity and phytoplankton biomass in coastal California [e.g. *Otero and Siegel*, 2004; *Venegas et al*., 2008; *Brzezinski and Washburn*, 2011]. Thus, it is expected that in upwelling-favorable conditions, increases in CHL will be associated with low temperatures (a proxy for nutrient increases) as there should be sufficient light levels for net growth of phytoplankton populations [*Behrenfeld et al.*, 2006; *Siegel et al*., 2013]. Here, changes in winds, temperature (and nutrients) are all shown to affect CHL retrievals differently in different portions of the domain, indicating that complex local and large scale processes likely overlap in time to determine regional changes in productivity and CHL patterns.

Changes in domain-mean CHL are significantly associated with upwelling-favorable wind stresses (r=-0.32; Figure 14a) and increases in wind speed (r=0.26), while no simple relationship with SST is observed (Figure 14b). However, the second CHL EOF mode (AF2-CHL) showed that seasonal CHL changes in the domain can be spatially decomposed into blooms that occur during spring in the SCBight (usually starting in March and peaking in April-May) and during summer in the SMBasin (with blooms peaking as late as September; Figures 7d and 8d). Alternatively, seasonal CHL plots for a SBC and a SMBasin region are presented separately in Figure 15. This figure shows that blooms in the SBC are on average stronger, peaking in a smaller time window of the year, whereas blooms in the SMBasin region occur over a wider range of months. SST changes in the domain partially

explain changes in the location of theses blooms (i.e. AF2-CHL; r=-0.35; Figure 14c), but lags between the variables are also observed (Figure 14c and 14d).

Although no simple relationship links wind stress conditions to CHL Mode 2 patterns (Table 2), the role of very strong upwelling-favorable winds in determining the timing of blooms in the SMBasin is clear. The major negative amplitude function values every year often occur simultaneously to or shortly lag the largest upwelling-favorable wind stresses off of buoy 46054 (for instance years 1998,1999, 2001, 2003, 2004, 2006-2008; Figure 14d). Negative peaks in CHL mode 2 occur with increasing temperatures and peak PAR values every year, around day of year 179 (June 28th +/- 30 days) for all years before 2009 (Figure 14e-f). This indicates the strong seasonality of CHL increases in the SMBasin. CHL changes in phase with upwelling winds and lagging SST minima are known features of eastern boundary currents, generally resulting in summer CHL maxima and winter minima in this region [*Thomas et al*., 2001; *Thomas and Strub*, 2001; *Legaard and Thomas*, 2006].

CHL increases in the SBC and SCBight (positive AF2-CHL values), on the other hand, occur over a wide range of wind conditions (for instance, increases in AF2-CHL occur simultaneously to strong upwelling-favorable winds in 2000 and 2002, while large AF2-CHL values during 2005 and 2010 occurred during less intense wind conditions; Figure 14d). However, peaks consistently co-occur with the lowest SST estimates in the SBC (from mean *in situ* surface estimates across the Plumes and Blooms stations; Figure 14e), as well as increasing PAR conditions (Figure 14f). Additionally, increases in mean CHL in the SBC ("SBC-mean CHL" in Table 2) are significantly associated with decreased Plumes and Blooms measurements of sea-surface temperature (r=-0.34) and shallower mixed-layer depths (r=-0.18), as well as increased surface salinity (r=0.29), surface nitrate (r=0.23), and

biogenic silica (r=0.55). This indicates that CHL blooms in the SBC are associated with large-scale circulation processes that result in the advection of colder, nutrient rich waters into the Southern California Bight, rather than regional-scale upwelling creating local phytoplankton responses.

Although the 1.5 months average timing difference between large blooms in the SCBight and SMBasin may arise from similar lags in CHL responses to SST changes in the domain, the lack of significant relationships along the CCS where mean CHL levels are often high is intriguing (Figure 16). In these areas, SST values are relatively cold throughout the year and show little variability (see Figure 3a-b). Thus, it is possible that other processes such as the seasonal deepening of the mixed layer (associated with strong winds) may help explain CHL variability decoupled from SST. Patterns in the third EOF CHL mode provide some evidence for the role of mixing in determining CHL changes (Figures 8e and 10f). Positive Mode 3 values are accentuated along the CC and coincide with the negative peaks in mode 2 (i.e. blooms in the SMBasin). Indeed, Mode 3 changes are also associated with large wave height conditions (Table 2).

The wide range of the relationships between CHL changes and physical forcings in the domain highlight a complex area where changes in CHL determinations (and likely productivity) are attributed to different controlling mechanisms over different time scales. The relationships with winds and SST support the role of regional upwelling in determining CHL changes in the SMBasin, while seasonal advection of water masses appear more directly related to CHL increases in the SCBight. Although the triggers of seasonal cycles of CHL in these two different regions were generally characterized, the role of short-scale, episodic processes such as eddies, jets, poleward flows and internal waves in determining

the timing and magnitude of CHL changes are likely responsible for many of the short-term patterns and deviations in the time-series comparisons.

4.4 Long-term trends in SST, BBP and CHL

While waves and discharge control nearshore BBP variability over times scales of days to weeks to seasons, and winds and SST control seasonal changes in CHL estimates throughout the domain, decreases in SST, at longer time scales, match tendencies of larger climatic variables such as the Pacific Decadal Oscillation (PDO) and ENSO. Indeed, SST anomalies show a positive and significant relationship with the PDO (r=0.67), and a negative relationship with the Southern Oscillation Index (SOI; r=-0.62). The long-term temporal SST trend was small and not significant at the 95% c.i., which might be due to the shorter time-span analyzed, missing the warm phases of ENSO in 1997-1998 (Figure 4d). However, SST trends are indeed significant in certain portions of the domain (Figure 4g), partially supporting the observed CHL increases over time and space.

Overall, good correspondence is observed between wind stress and mean changes in CHL (Mode 1 CHL) during most of the time series (e.g. 2000-2004 and 2007-2009). However, strong deviations also occur (Figure 15a). For instance, above-average wind conditions did not lead to increases CHL during the 1998-1999 period. The opposite is observed during 2005 and 2010, when large CHL signals are observed in a period where winds were weak. This indicates the role of larger-scale processes such as El Niño (strong in 1998; Figure 5a), and PDO (strong in 2010; Figure 5b) in determining CHL variability in the domain and decoupling productivity from local upwelling conditions. Increases in CHL during the 2005-2006 period coincided with the only negative NPGO conditions observed in

the time series (Figure 5c). However, negative NPGO conditions are not usually related to increases in CHL in the SMBasin/SCBight region, since it implies a weaker North to South transport of nutrient rich waters [*Di Lorenzo et al*., 2008]. Here, CHL increases were registered in both the SMBasin and SCBight regions (Figure 9d), and a very large bloom was observed in July 2005 along the CCS (largest positive peak in Mode 3 during 2005 in Figure 9e). This large bloom is shown in more detail in Figure E in the Appendix. These observations illustrate the complexity of the relationships among ocean circulation processes, which likely interact nonlinearly, and bio-optical changes in this SMBasin/SCBight transition region. In the case of the July 2005 bloom, increases in sub-mesoscale eddy activity and mixing with Southern California waters (see the patchy distribution of SST in Figure D) could have driven increases in CHL at those locations.

The implications of global climate change in determining long-term variations in CHL and SST across regional scales for the CCS have been widely studied [*Kahru and Mitchell*, 2001; *Kahru et al.*, 2009; *Kahru et al*., 2012; *Siegel et al*., 2013; *Kahru et al*., 2015]. The trend of increasing CHL in the domain (0.42% per year; Figure 4) is consistent with the literature [*Kahru et al*., 2009; *Nezlin et al*., 2012; *Karhu et al*., 2015], and believed to be linked to an increase in upwelling-favorable winds and wind-driven upwelling due to increased onshore-offshore atmospheric pressure gradients and enhanced alongshore winds tied to global warming [*Garcia-Reyes and Largier*, 2010; *Kahru et al*., 2015]. However, the extreme low/high CHL values occur at opposite ends of the available 13-year time series, augmenting linear trends, and perhaps artificially linking these long-term changes to warm/cold phases of ENSO and PDO (see Figure 5). Removing the extreme negative and positive anomaly years for CHL (i.e. 1997-1998 and 2010) resulted in reduced but still

significant trends (+0.19% per year; p-value=0.0062). Certainly, the unusual oceanographic conditions that led to very large CHL increases such as in 2010 (i.e. much colder SSTs in August and September of that year than any other year; see Figure F in Appendix) need to be further addressed in order to assess if changes are local/episodic or if they are indeed associated with large-scale anomalies in oceanographic conditions.

Temporal trends in BBP do not increase at the same rate as trends in CHL. This is likely because BBP changes are driven by both biogenic and non-biogenic processes that operate during different portions of the year (see Figure 6f). In particular, two main events appear responsible for the flatter BBP trends compared to CHL (Figures 4e-f). First, the intense El Niño of 1997-1998 resulted in large runoff into the ocean, increasing the importance of non-biogenic BBP to the total BBP signal but not affecting CHL values positively. The second large discrepancy between CHL and BBP anomalies occurs in 2003-2004. During this period, BBP anomalies are as large as those of 1998, but the source of the high values is not storm-related, since its peak occurs in the summer and no large storms were registered in the several months before the event. The lack of a strong CHL:BBP correspondence at those times (see how their distributions differ over space in Figure G in Appendix) may be related to the occurrence of blooms with higher BBP:CHL signatures, such as coccolithophores [*Balch et al*., 2011]. However, photoacclimation processes may also be responsible for CHL and BBP disparities in offshore waters, especially during summer months. Nonetheless, differences in species composition (including harmful algal blooms) and exposure to light as sources of deviation between CHL and BBP require further investigation. Appropriate biogeochemical models supporting the conversion of BBP and CHL into carbon estimates in

these optically complex waters, as well as information of species composition over large spatial scales would be necessary to address these questions.

Thirteen years of satellite data are obviously not sufficient to conclusively determine the effects of multi-year and decadal changes in physical and bio-optical properties. However, results support the use of an integrated approach that takes advantage of merging several satellites grounded with consistent field observations to analyze long-term changes in surface ocean properties in complex waters. Future analysis should explore the use of spatial information on waves (e.g. CDIP; https://cdip.ucsd.edu/), surface currents (e.g. HF-Radar; http://www.sccoos.org/data/hfrnet/) and winds (e.g. QuickSCAT; http://manati.star.nesdis.noaa.gov/datasets/QuikSCATData.php/) to help understand meso and sub-mesoscale variability in bio-optical parameters and determine the specific mechanisms that lead to the accumulation and advection of phytoplankton patches and sediment plumes across the domain.

5. Conclusions

Thirteen years of spectrally merged satellite observations of chlorophyll (CHL) and optical backscattering coefficients (BBP) for the Santa Maria Basin / Southern California Bight region were analyzed to retrieve the main controls on particle variability over seasonal to multi-annual time scales. CHL blooms in the domain occur between early spring and summer, although mean CHL estimates for the region can be decoupled in space between large blooms that occur in the Southern California Bight, and large blooms that occur in the Santa Maria Basin. CHL increases in the Southern California Bight occur in phase with SST

minima, while CHL blooms in the Santa Maria Basin lag SST minima and occur simultaneously to the largest equatorward winds every year and highest PAR levels, indicating the high seasonality of CHL changes in this region. Connections among CHL changes and El Niño and Pacific Decadal Oscillation were also found, illustrating the wide range of processes that likely interact to affect CHL variability over various time/space scales. Surface waves were shown to have a large role in controlling BBP throughout all seasons, often affecting variability of waters shallower than 100m depth. River runoff effects on particle variability were observed to be roughly limited to those years associated with El Niño events, when extreme storms occurred. The implication of surface waves determining BBP variability beyond the surf zone has large consequences for the life cycle of many marine organisms, as well as for the interpretation of remote sensing signals near the coast.

Tables and Figures

Table 1. Matchup statistics between Plumes and Blooms field observations and SeaWIFS (SW), MODIS (MO) and MERIS (ME) $R_{rs}(\lambda)$ data and GSM-derived BBP, CHL and CDM. All coefficients of determination are significant at the 95% c.i..

	Rrs412			Rrs443			Rrs490			Rrs555			CHL			BBP			CDM		
	SW	MO	ME	SW	MO	ME	SW	MO	ME	SW	MO	ME	SW	MO	ME	SW	MO	ME	SW	MO	ME
R^2	0.03	0.04	0.1	0.12	0.18	0.26	0.27	0.3	0.38	0.39	0.39	0.42	0.56	0.52	0.58	0.34	0.22	0.41	0.02	0.28	0.19
Slope	0.4163	0.3737	0.4435	0.4112	0.4578	0.513	0.4663	0.5201	0.5161	0.6797	0.5688	0.7812	0.7001	0.6905	0.8012	0.5844	0.3756	0.6519	0.272	0.8247	0.7186
RMS	0.0015	0.0008	0.0008	0.0011	0.0006	0.0006	0.0007	0.0006	0.0004	0.0006	0.0005	0.0005	1.0375	0.9948	0.9470	0.0024	0.0021	0.0015	0.0958	0.0644	0.0563
N	492	343	169	491	343	169	493	344	169	467	344	169	388	245	160	210	189	136	332	237	152

Table 2. Correlation coefficients among domain-mean SST, BBP, CHL, their anomalies, SBC-mean CHL and BBP, dominant amplitude functions, and selected environmental forcings. Only significant correlations at the 95% c.i. are shown. **Bold** values indicate correlations that are discussed in the text.

		Means and Anomalies								EOF Amplitude Functions							
		mean SST	mean CHL	mean BBP	SST anomaly	CHL anomaly	BBP anomaly	SBC-mean CHL	SBC-mean BBP	AF1-SST	AF2-SST	AF1-CHL	AF2-CHL	AF3-CHL	AF1-BBP	AF2-BBP	AF3-BBP
Means and Anomalies	mean SST	x								**0.94**			**-0.34**	-0.17	-0.12	-0.18	0.35
	mean CHL		x								-0.43	**0.93**			**0.67**	**-0.40**	
	mean BBP		**0.80**	x							-0.53	0.70			**0.80**	-0.16	0.17
	SST anomaly	0.41	-0.19	-0.11	x					0.28	0.21	-0.16	-0.13			0.16	
	CHL anomaly		0.68	0.43	**-0.36**	x					-0.11	0.63	0.11	0.12	0.41	-0.21	
	BBP anomaly		0.53	0.59	**-0.27**	0.76	x				-0.11	0.47		0.20	0.56		
	SBC-mean CHL	-0.21	0.78	0.59	-0.19	0.53	0.38	x		-0.15	-0.27	0.80	0.48	-0.20	0.59	-0.23	0.14
	SBC-mean BBP	-0.12	0.52	0.73		0.29	0.48	0.65	x	-0.23	-0.24	0.52	0.30	-0.12	0.75	0.23	0.43
Forcings	Sig Wave Height	-0.45	-0.16	-0.09			0.12		0.13	-0.51	0.17	-0.12	0.11	**0.23**	**0.12**	**0.48**	-0.20
	Wind Speed		**0.26**	0.34				0.24	0.27		-0.58	0.28		0.10	**0.37**		
	Pax Wind Stress		**-0.30**	-0.34				-0.27	-0.17		**0.55**	**-0.32**		-0.10	**-0.34**	**0.23**	0.10
	PDO	0.16	-0.08		**0.67**	-0.10			0.12		0.10				0.10	0.27	
	SOI	-0.27	0.15		**-0.62**	**0.33**	0.22	0.15		-0.22		0.13	0.14			-0.16	-0.11
	NPGO	-0.12			-0.37	-0.09					-0.16						
	PAR	0.32	0.37	0.47				0.27	0.22	0.33	-0.59	0.31		-0.20	0.22	-0.41	0.28
	VR discharge		-0.10	0.12	0.12	-0.09	0.16		0.38	-0.11	0.10	-0.09			**0.20**	**0.56**	0.30
PnB measurements	SST (PnB)	0.87	-0.18	-0.18	0.24	-0.26	-0.20	**-0.34**	-0.30	0.87		-0.16	-0.39	-0.12	-0.26	-0.16	0.25
	MLD (PnB)	-0.44	-0.28	-0.35				**-0.18**	-0.15	-0.48	0.45	-0.27	0.15	**0.29**	-0.15	0.35	-0.35
	surf salinity (PnB)	-0.14	0.33	0.36	-0.43	0.11		**0.29**	0.20		-0.51	0.27	0.12		0.18	-0.33	0.16
	surf NO3 (PnB)	-0.46	0.15	0.19	-0.32	0.09		**0.23**	0.21	-0.47	-0.21	0.11	0.25	0.13	0.19		-0.10
	suf Bsi (PnB)	-0.38	0.44	0.41	-0.38	0.27	0.17	**0.55**	**0.31**	-0.31	-0.31	0.41	0.31	-0.12	0.33	**-0.18**	
	surf Lsi (PnB)	-0.34	-0.24	-0.14		-0.18		-0.12		-0.33	0.21	-0.20	0.13			**0.44**	-0.14

Table 3. Correlation coefficients among de-seasoned amplitude functions and domain-mean SST, CHL, BBP, as well as de-seasoned wave height, wind speed and wind stress. Discharge was not de-seasoned. Only significant correlations at the 95% c.i. are shown. Bold values indicate correlations that are discussed in the text.

	Mean SST_d	Mean CHL_d	Mean BBP_d	SWH_d	Wind $Speed_d$	Wind $Stress_d$	Discharge
AF1 $Temp_d$	0.50	-0.31	-0.19	-0.12	-0.30	0.25	
AF2 $Temp_d$	0.28	-0.24	-0.18	-0.20	-0.45	**0.38**	
AF1 BBP_d		0.65	0.83	**0.22**	**0.18**	**-0.23**	**0.21**
AF2 BBP_d	0.11	-0.28		**0.35**		0.09	**0.51**
AF3 BBP_d					-0.10	0.25	0.37
AF1 CHL_d	-0.12	0.93	0.68		0.08	-0.18	
AF2 CHL_d							
AF3 CHL_d		0.16	0.22	0.10	0.18	-0.21	

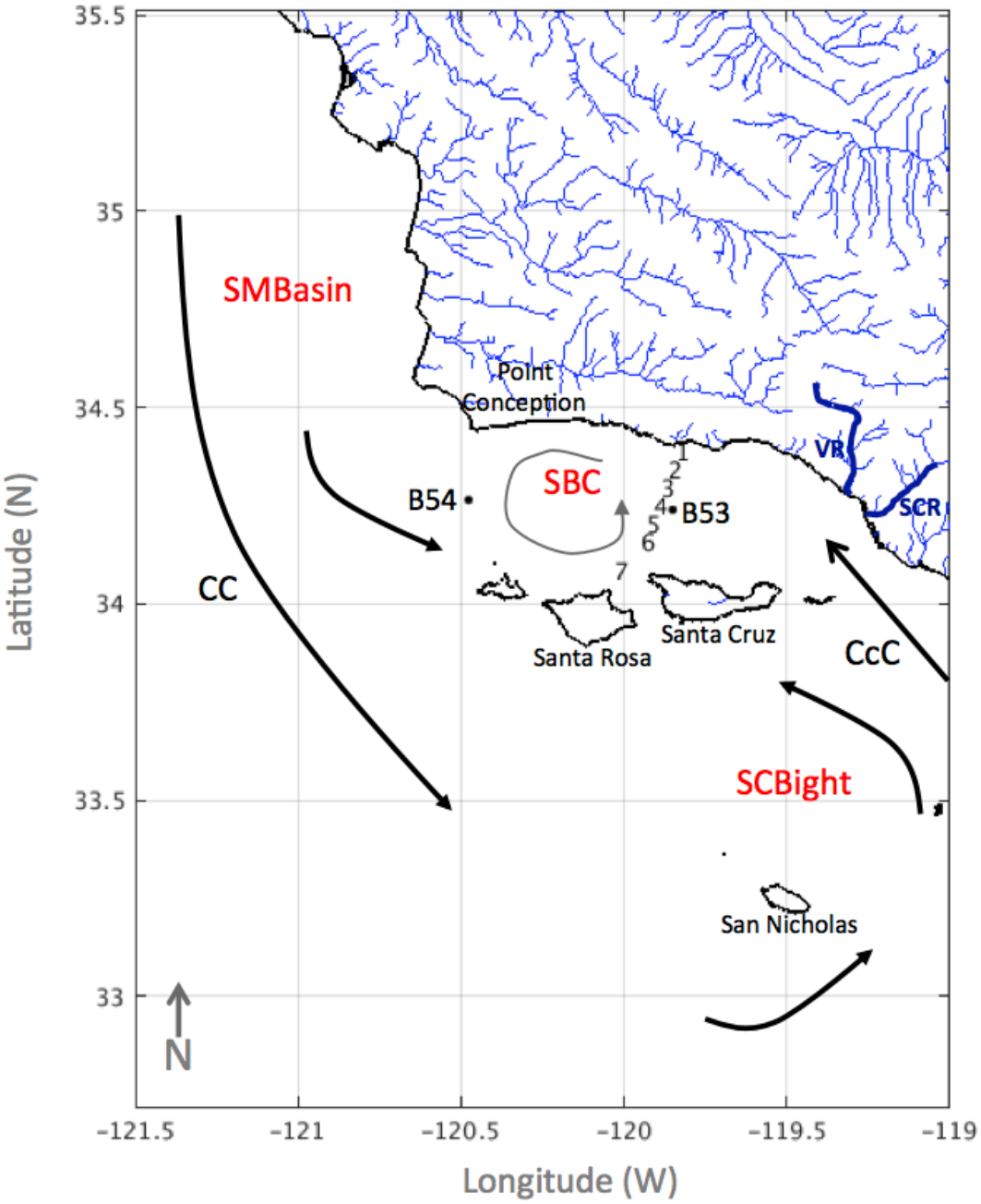

Figure 1. The Santa Maria Basin – Southern California Bight study area including streams, a conceptual view of main currents and flows, as well as the locations of NDBC buoys 46053/46054 and Plumes and Blooms stations. The SBC eddy is illustrated in the middle of the channel. VR = Ventura River; SCR = Santa Clara River; CC = California Current; CcC = California counter-current.

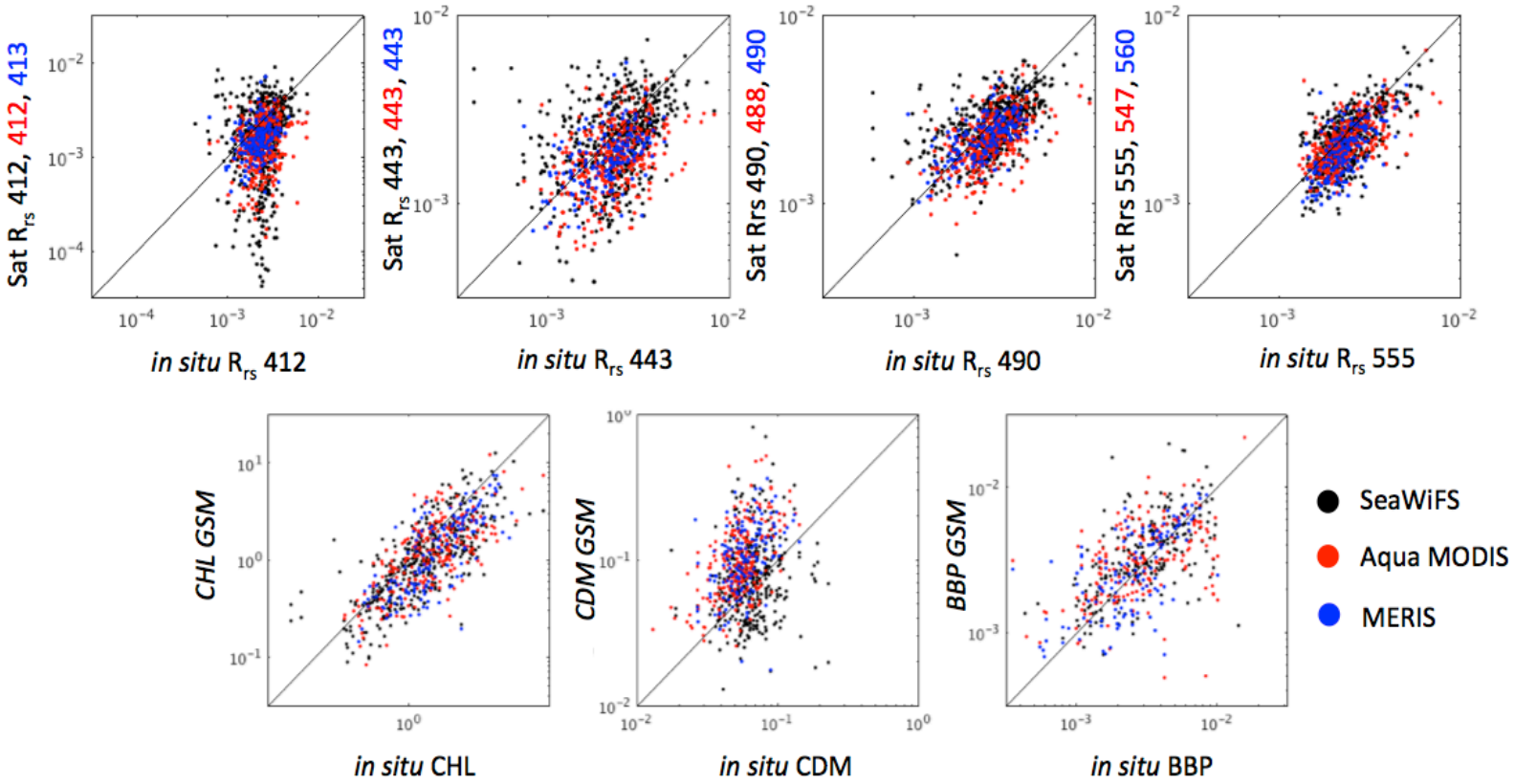

Figure 2. Top panel: Matchup comparison between satellite and field $R_{rs}(\lambda)$ measurements. Note that wavelengths available per satellite do not always perfectly match field observations. **Bottom panel:** Matchup comparison between GSM-derived satellite estimates of CHL, CDM and BBP for each of the three satellites used in this study and field observations of $b_{bp}442$nm, detritus and dissolved absorption, and fluorometric chlorophyll . SeaWiFS data covers 1997 – 2010; MODIS and MERIS cover 2002-2010. Reflectances were inverted in GSM to retrieve CDM (a_g443+a_d443), BBP ($b_{bp}443-b_{bw}443$, where $b_{bw}443$ is from Smith and Baker (1981)), and CHL is in mg/m3. The 1:1 reference line is shown on all graphs. Coefficients of determination between field and observations are presented in Table 1.

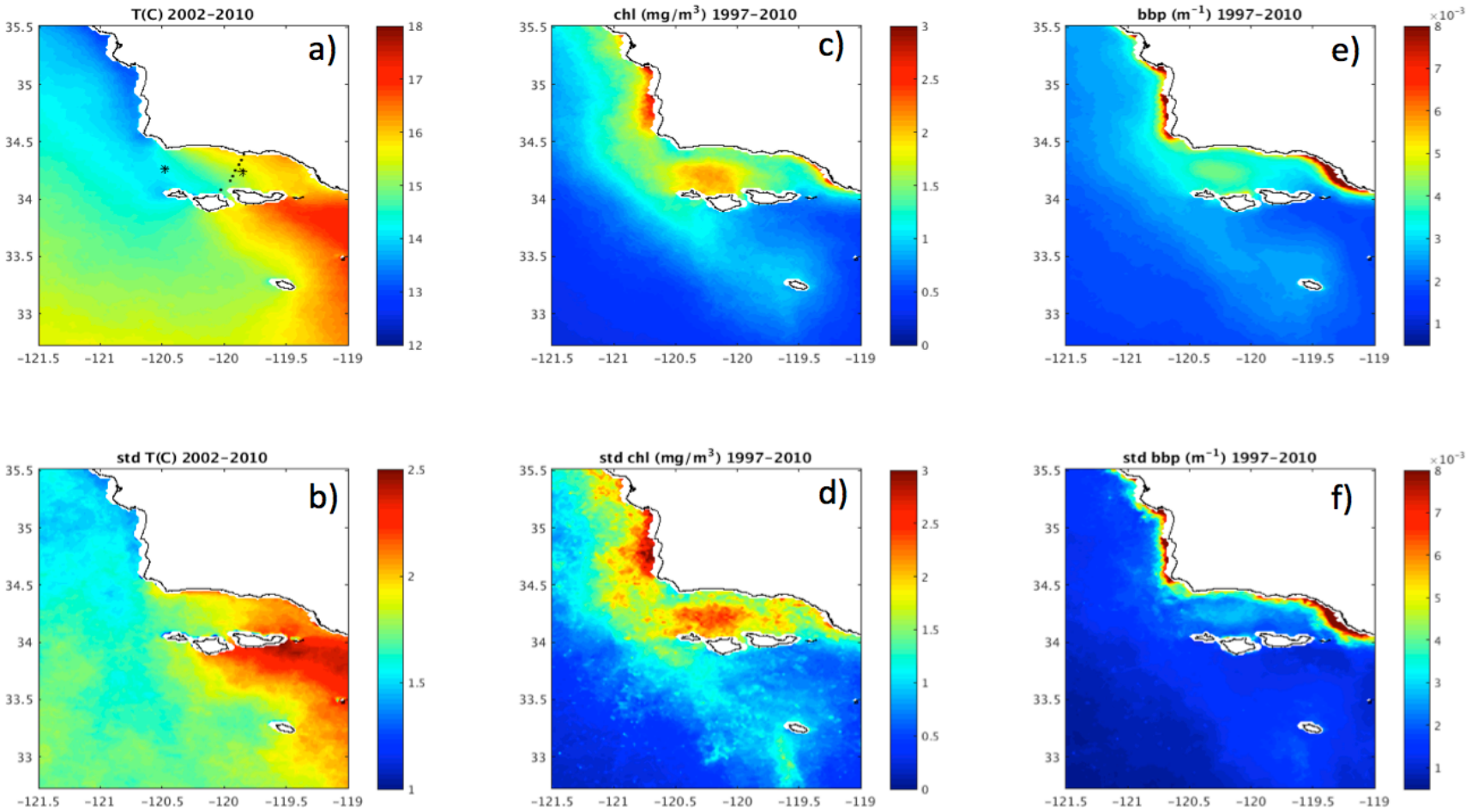

Figure 3. Means and standard deviations of SST, CHL and BBP between 2002-2010 (SST) and 1997 and 2010 (bio-optical properties); a-b) Means and standard deviations of MODIS-Aqua SST estimates; c-d) Means and standard deviations of CHL from 8-day Merged GSM data (SeaWIFS, MODIS and MERIS); e-f) same as b but for BBP. Spatial resolution is 2km for all variables. A mask excluding pixels with less than 60% coverage over the entire time series is applied (mask affects pixels along the shore and islands; see Figure A in Appendix). Black dots in first panel are the Plumes and Blooms stations 1 (closest to shore) to 7 (furthest offshore). Westernmost asterisk is the location of NDBC buoy 46054, easternmost asterisk is NDBC 46053.

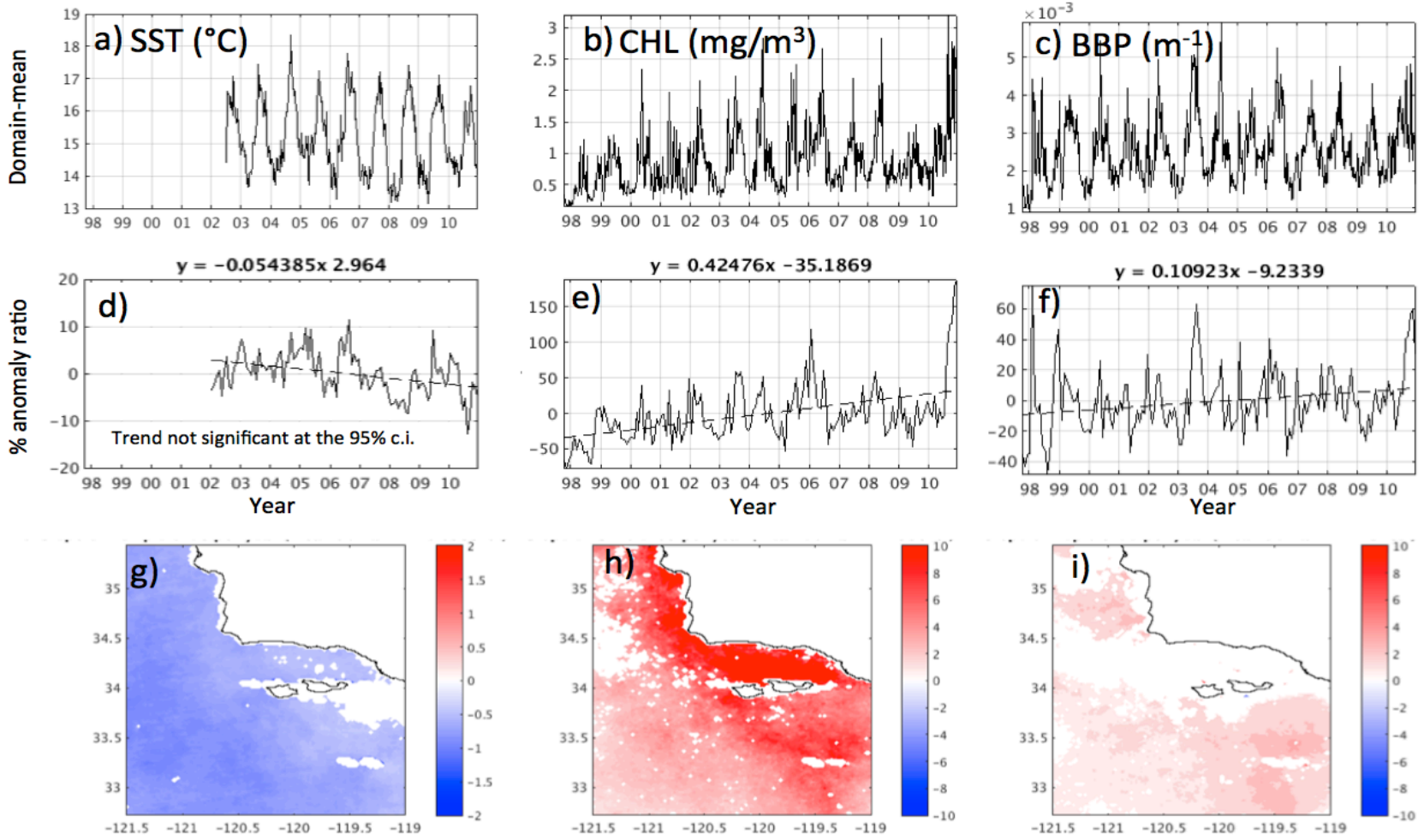

Figure 4. Regional means and long-term trends in SST, BBP and CHL. a) Domain-average SST estimates from 8-day average data; b) Domain-average CHL estimates from 8-day averages of GSM-merged data; c) same as b) but for BBP; d) Anomaly ratio from monthly SST data and linear trend (trend is not significantly different from zero at the 95% c.i.); e) Anomaly ratio from monthly CHL data and linear trend (significant at the 95% c.i.); f) same as e) but for BBP (significant at the 95% c.i.); g) significant slopes of a linear trend from monthly anomaly ratios for SST data per year (in percentage) for the available time period for each pixel; h) same as g) but for CHL; i) same as g) but for BBP. Only values significant at the 95% confidence level are plotted. Anomaly ratio is the ratio of that month's current value to the mean value of that month, and is expressed as percentage anomaly with 100 x (Anomaly -1) as in Kahru et al. (2012).

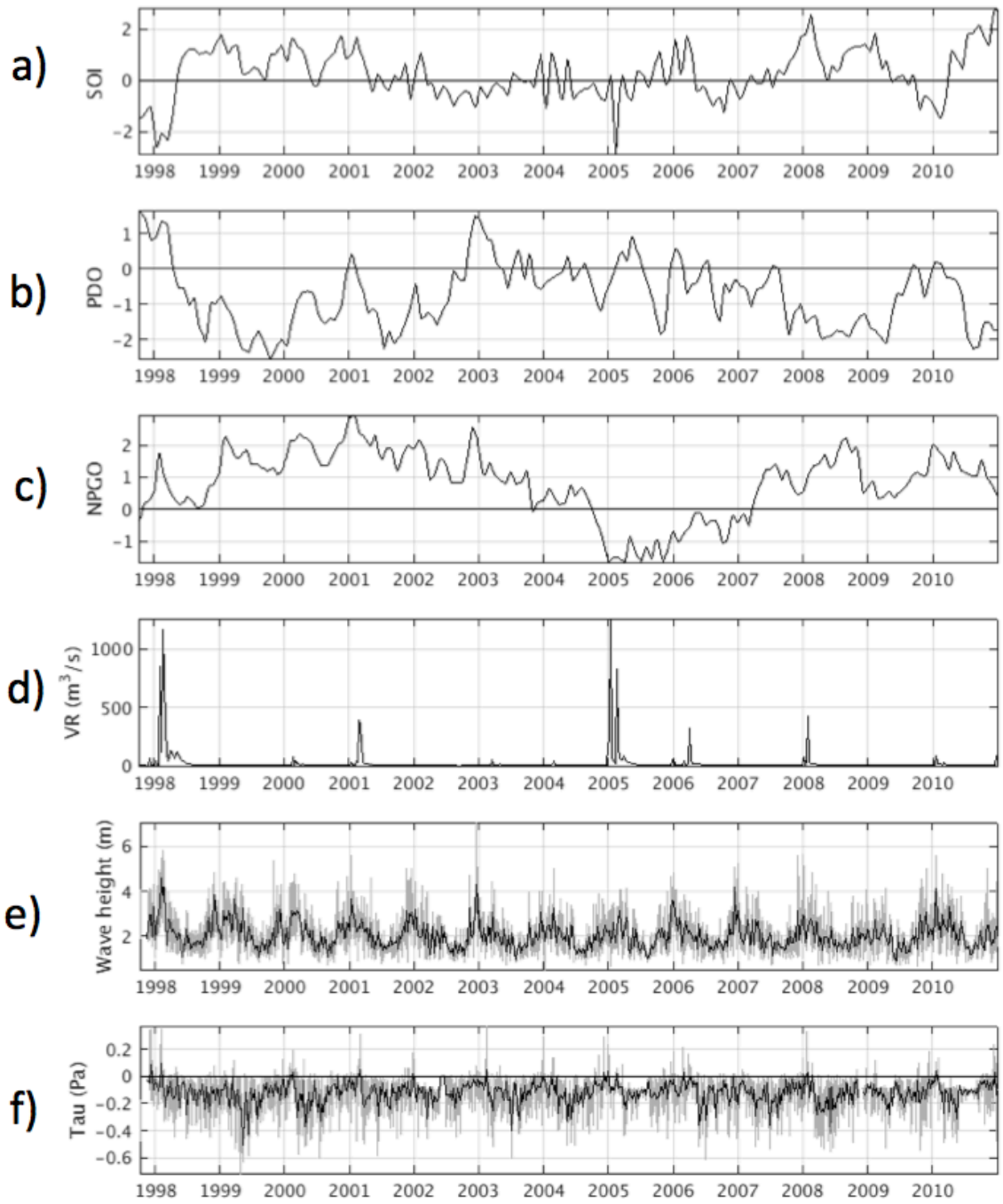

Figure 5. a) Monthly Southern Oscillation Index; b) Pacific Decadal Oscillation; c) North-Pacific Gyre Oscillation; d); 8-day accumulated discharge at Ventura River; e) 8-day mean significant wave heights at NDBC buoy 46054; f) 8-day means of the principal axis of wind stress from buoy NDBC buoy 46054. Extreme negative SOI = El Nino; Positive PDO = warm North-Pacific waters; Extreme positive NPGO = stronger N to S advection of CC waters.

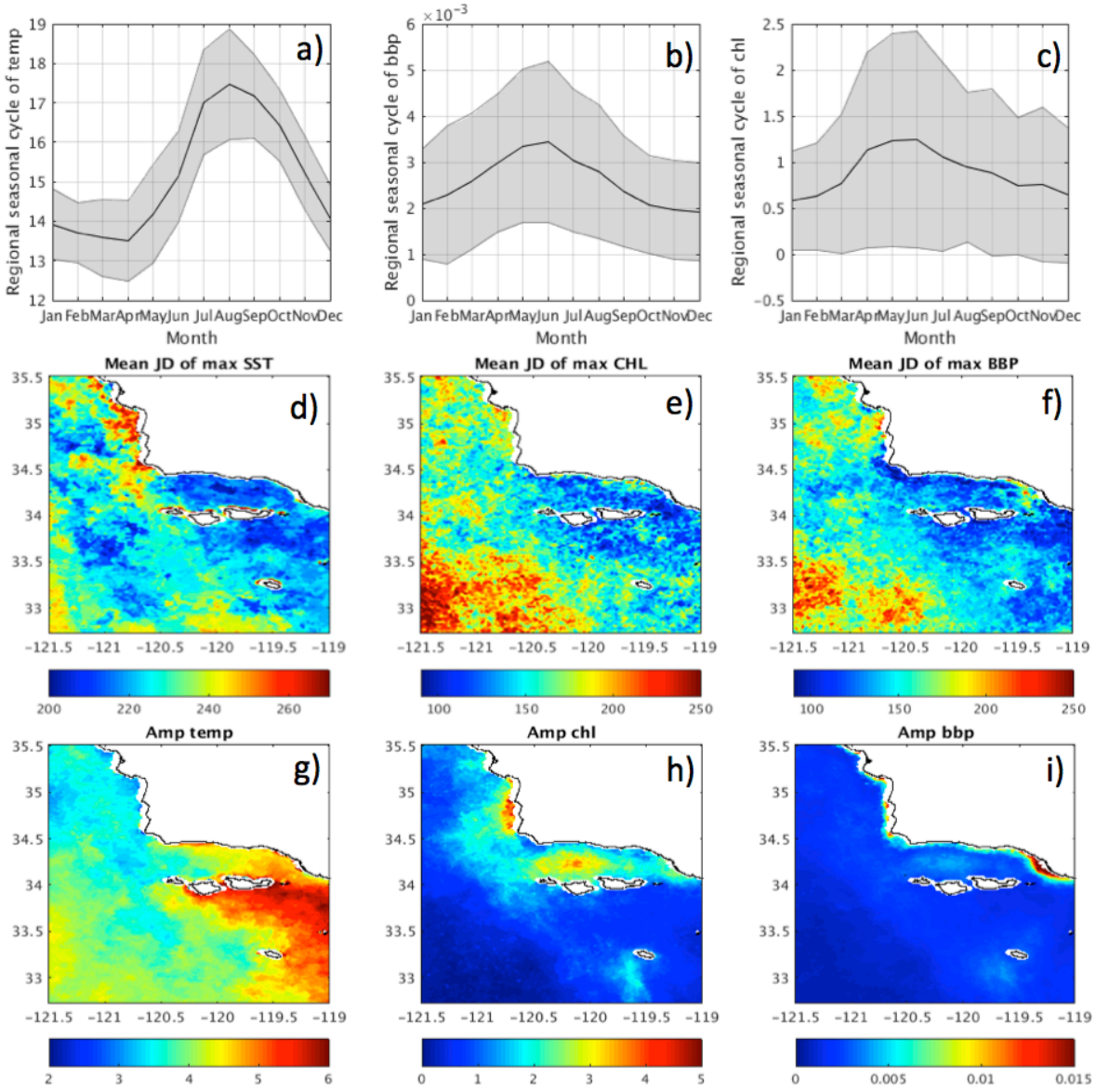

Figure 6. Mean seasonal cycle over time and space. a) Mean seasonal cycle of SST and variability (1 standard deviation about the mean); b) same for CHL); c) same for BBP; d) Mean Julian Day of maximum SST for each pixel; e) same for CHL; f) same for BBP; g) mean amplitude of the seasonal cycle (max-min) for SST; h) same for CHL; i) same for BBP.

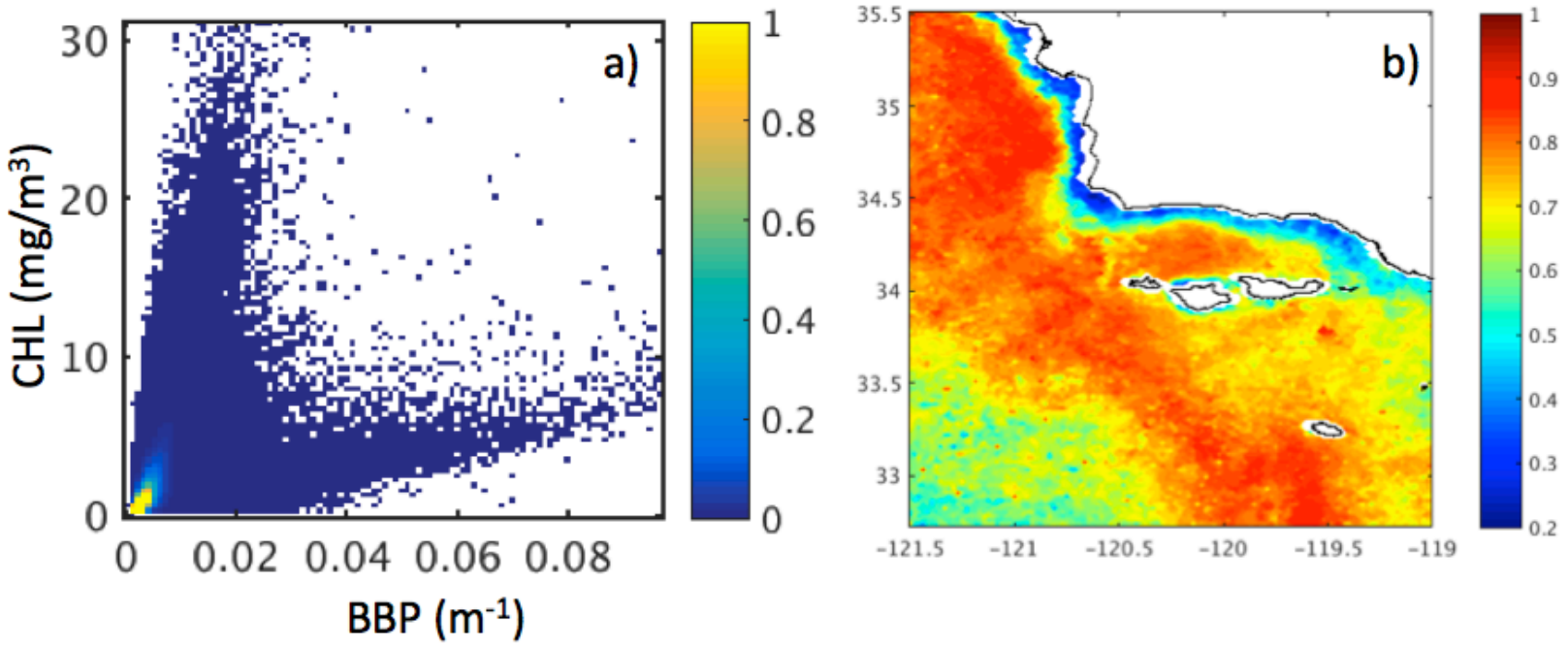

Figure 7. a) Probability frequency of occurrence for BBP versus CHL for every pixel in the domain during the 1997-2010 period. Values of probability of occurrence were calculated for 100 bins for both chl and bbp ranges, and are scaled so that the sum over all parameter space is equal to 1; b) map of correlation coefficients between BBP and CHL from the Merged, 8-day BBP and CHL data.

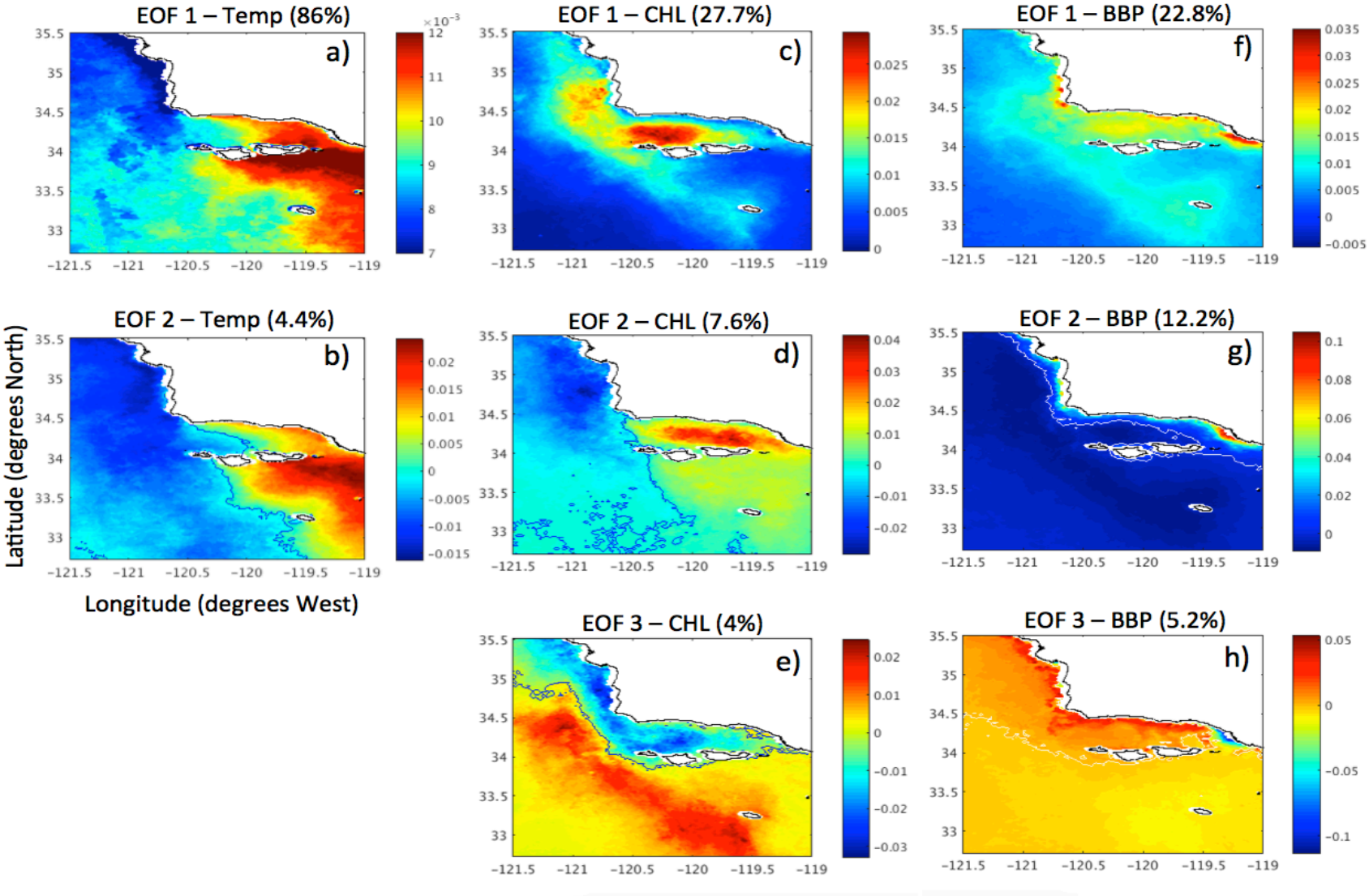

Figure 8. Empirical Orthogonal Function maps of SST, CHL and BBP. a-b) Dominant modes of variability of SST; c-e) dominant modes of variability of CHL; f-h) dominant modes of variability of BBP. The percentage of explained variance is given for each EOF. The white and blue contours delineate the zero crossing line where the EOF signs flip.

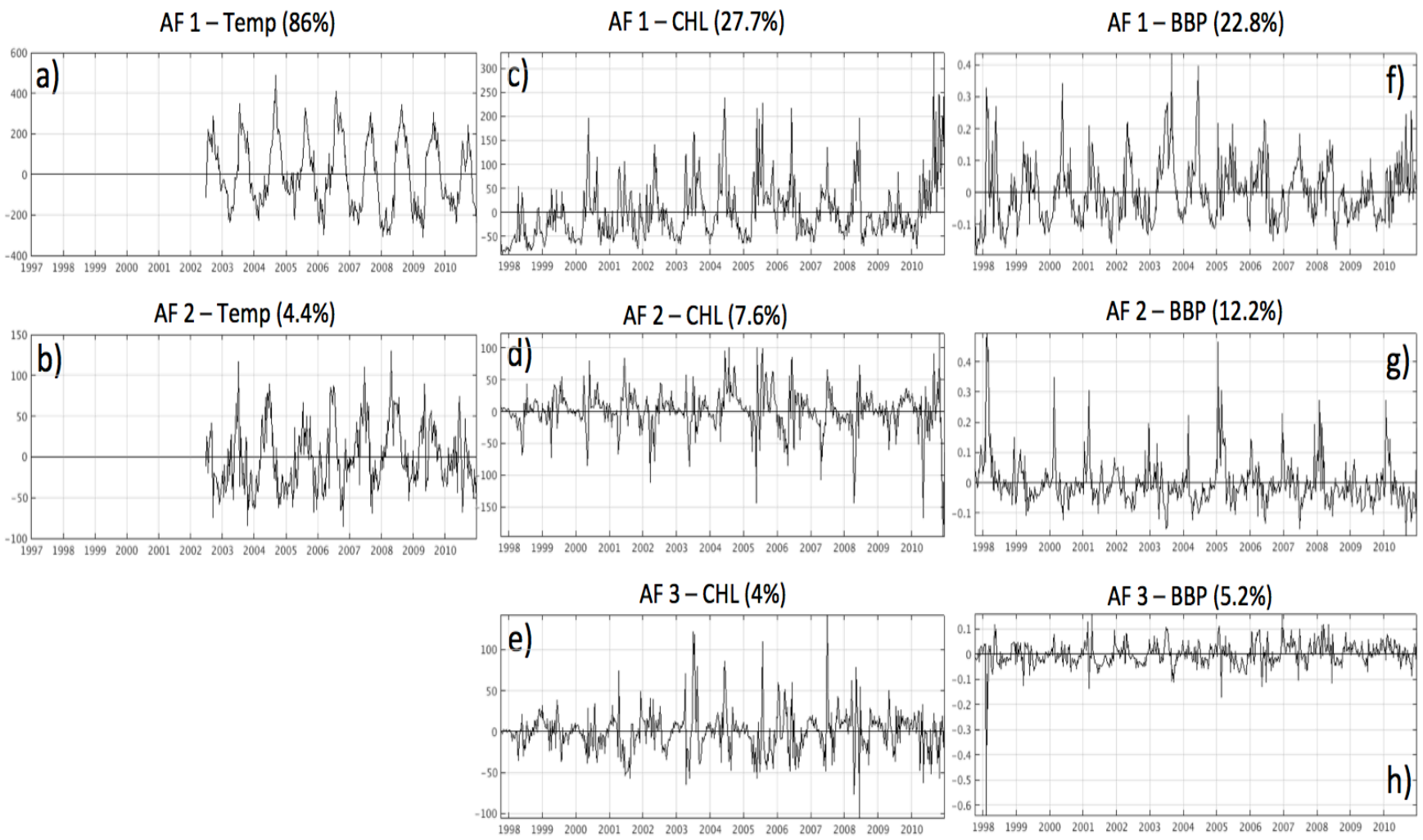

Figure 9. Dominant Amplitude Functions from Empirical Orthogonal Functions of SST, CHL and BBP; a-b) Dominant amplitude function of SST; c-e) dominant amplitude functions CHL; f-h) dominant amplitude functions of BBP.

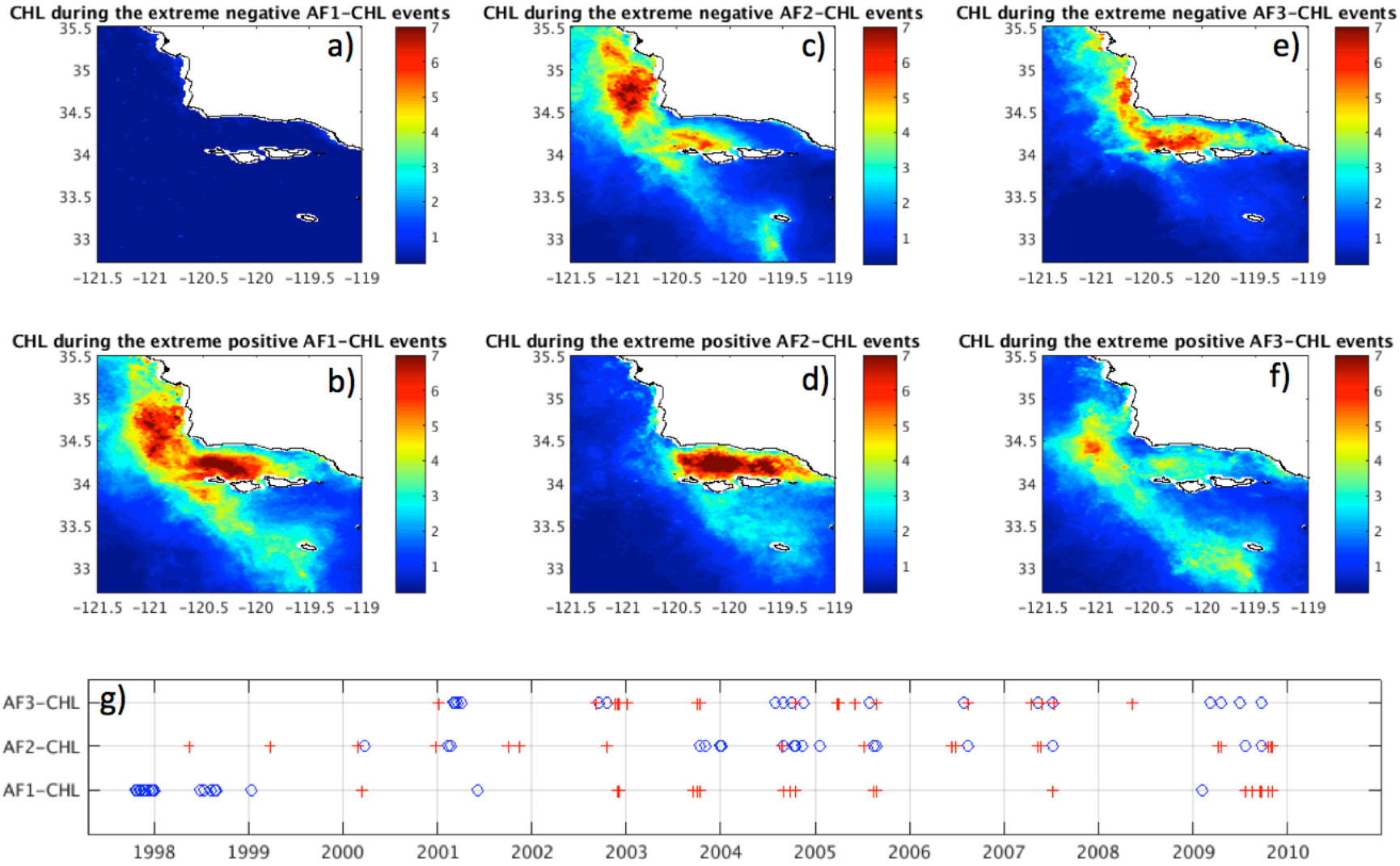

Figure 10. Mean CHL values during the extreme 3% negative and positive CHL EOF Amplitude Functions. a-b) Mean CHL in mg/m^3 during the extreme negative (a) and positive (b) amplitude functions of Mode 1; c-d) same for Mode 2; e-f) same for Mode 3; g) extreme negative (blue circles) and positive (red plus signs) amplitude functions mapped in time.

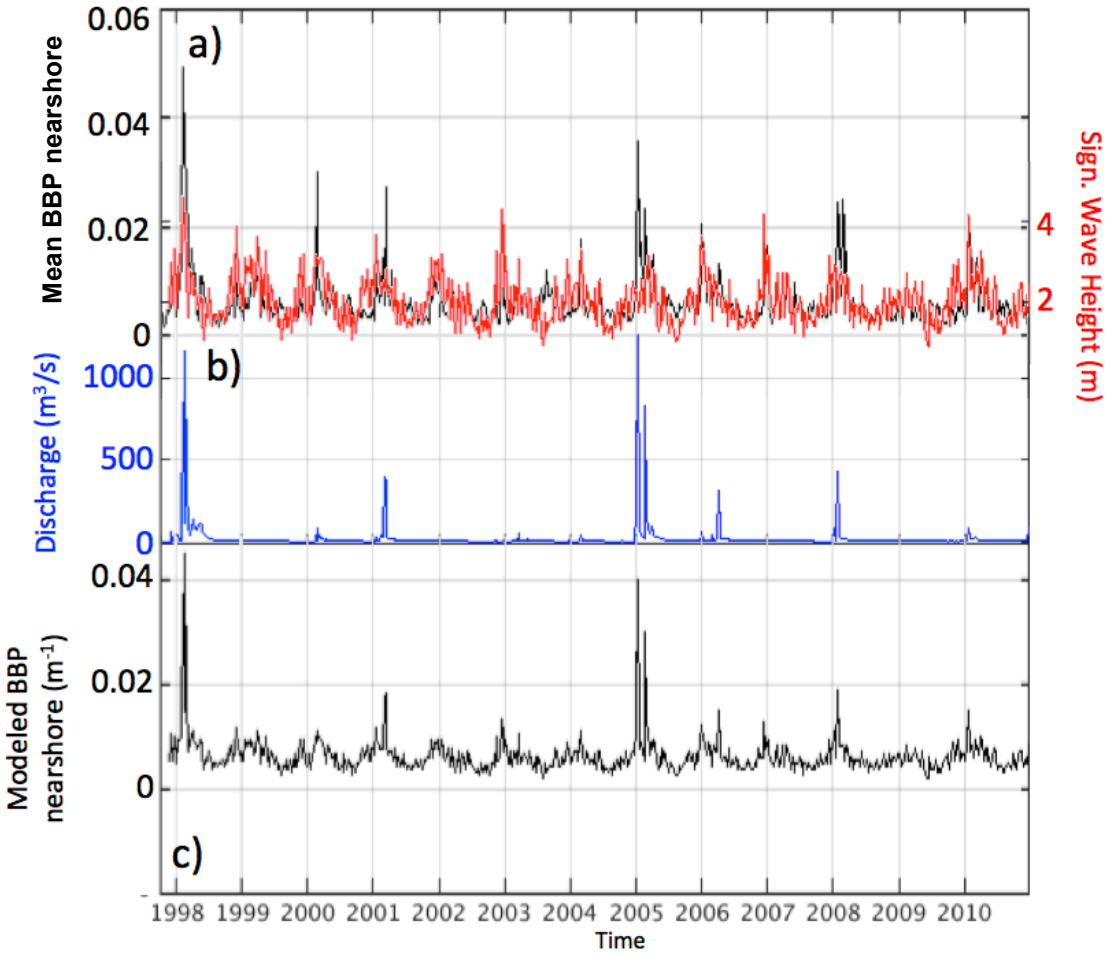

Figure 11. a) Comparison between mean BBP aggregates (black) for a nearshore region ~10km from the coast and 8-day averages of significant wave height (SWH; red); b) accumulated discharge over 8 days from the Ventura River (blue); c) The results of a multiple linear regression using wave height and discharge as predictors of mean BBP nearshore (model BBP = R^2=0.57; p-value <<0.001; variance inflation factor between explanatory variables is small).

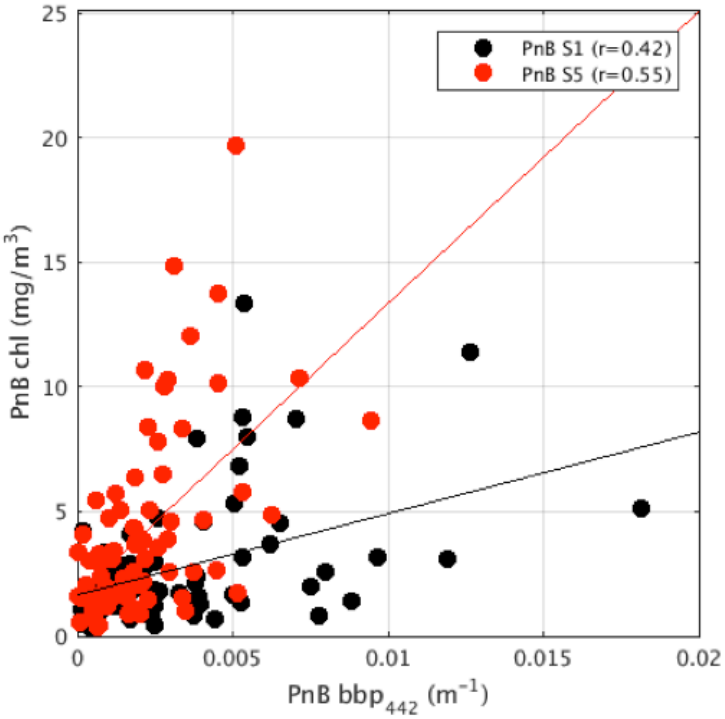

Figure 12. Relationship between simultaneous near-surface in situ chlorophyll concentrations and optical backscattering at 442nm from Plumes and Blooms Station 1 (black; closer to shore; n=92) and Station 5 (red; offshore; n=98). PnB data from 1998 – 2013 are used.

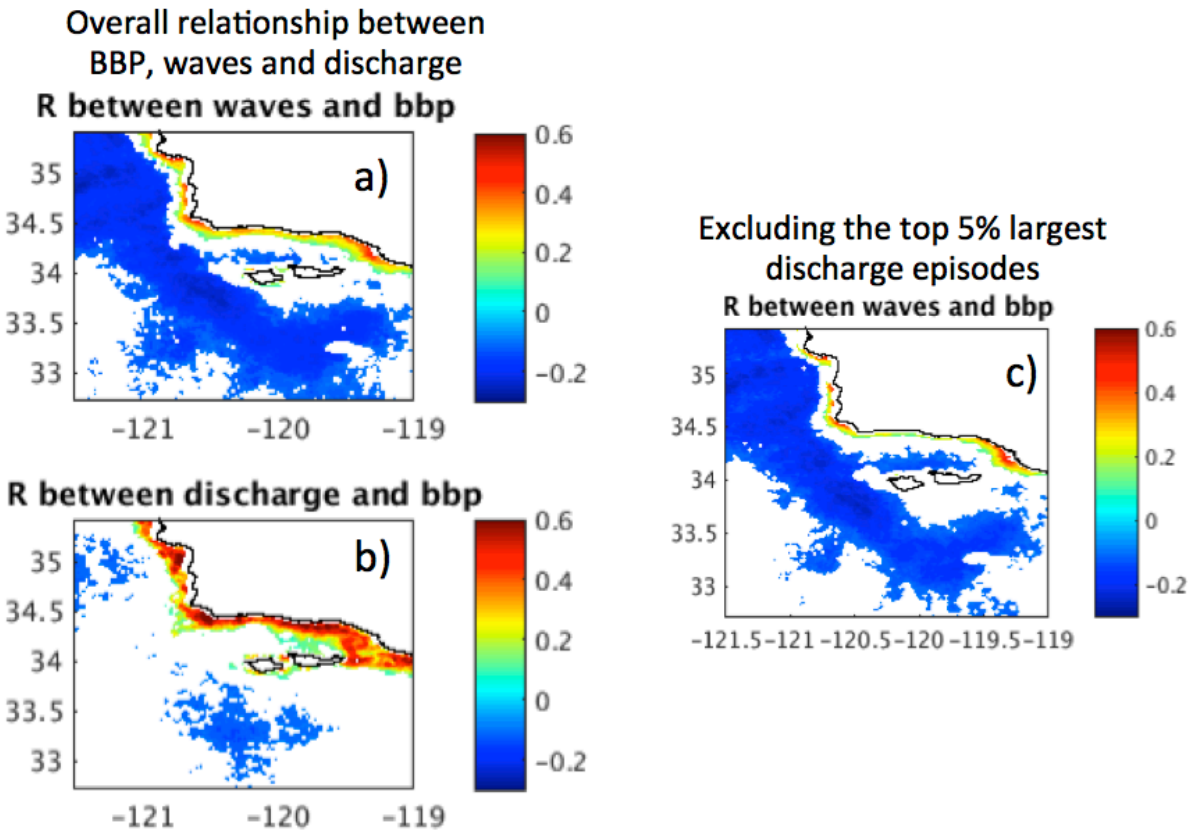

Figure 13. Correlation coefficient maps between BBP and a) significant wave height at NDBC buoy 4604 and b) river discharge at Ventura River; c) same as a) but excluding BBP during the 5% highest discharge episodes. Wave values used in the calculation were averaged every 8 days around the mean timestamp of every satellite merged product. Discharge values are accumulated discharge for the same 8-day period. White areas are not significant at the 95% confidence interval.

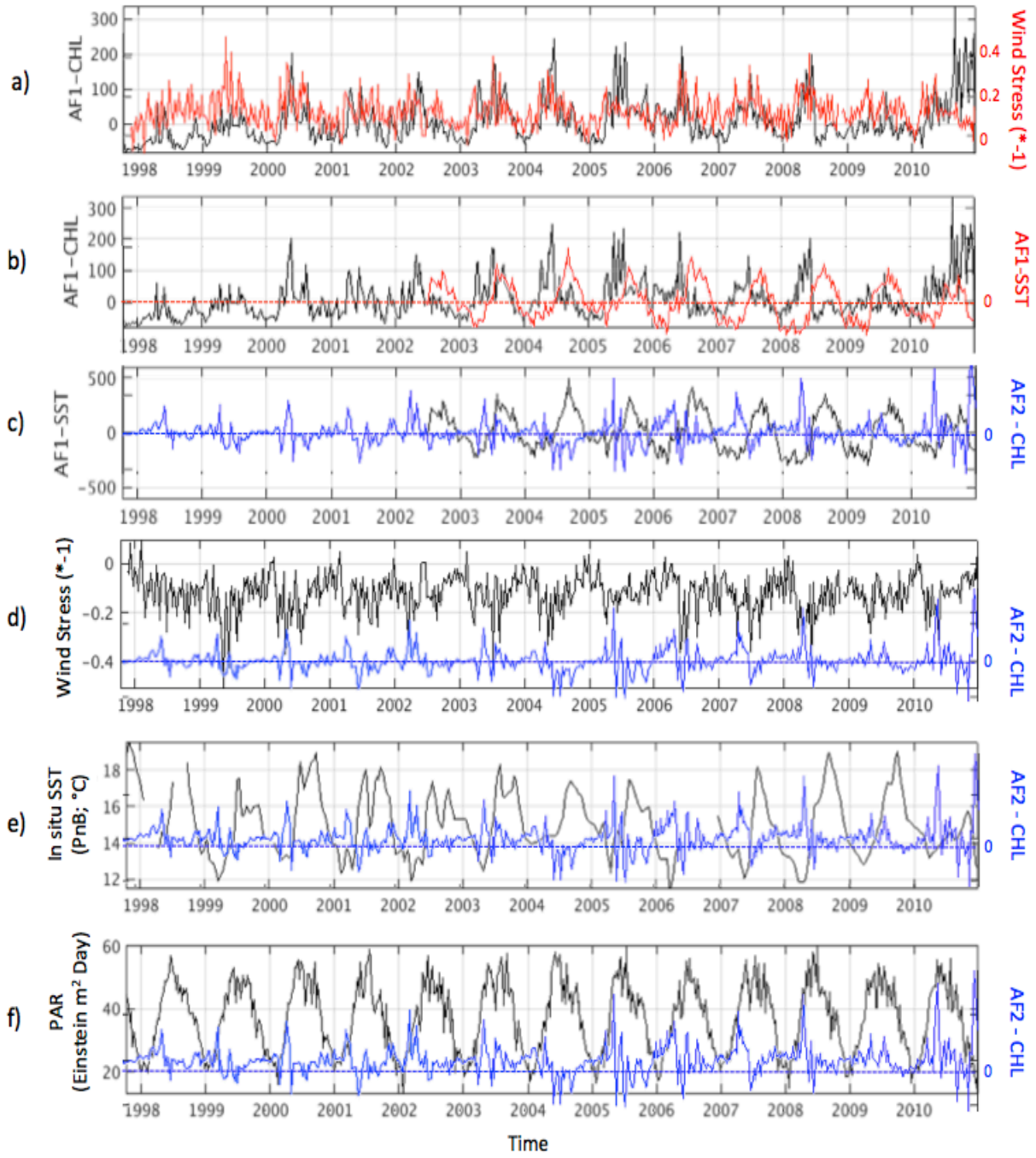

Figure 14. a) First Mode of CHL variability for the domain (AF1-CHL) and the Principal Axis for wind stress at buoy 46054 (multiplied by -1 to facilitate comparison with AF1-CHL; positive value thus denote upwelling-favorable conditions); b)AF1-CHL and AF1-SST (roughly equivalent to the mean domain SST estimates; c) AF1-SST and AF2-CHL; d) Wind stress (original units where negative values are upwelling-favorable) and the second mode of CHL variability for the domain (AF2-CHL); e) in situ surface temperature measurements from the mean of all seven Plumes and Blooms stations (since satellite SST was only available after 2002) and AF2-CHL; f) mean domain PAR from Aqua-MODIS data.

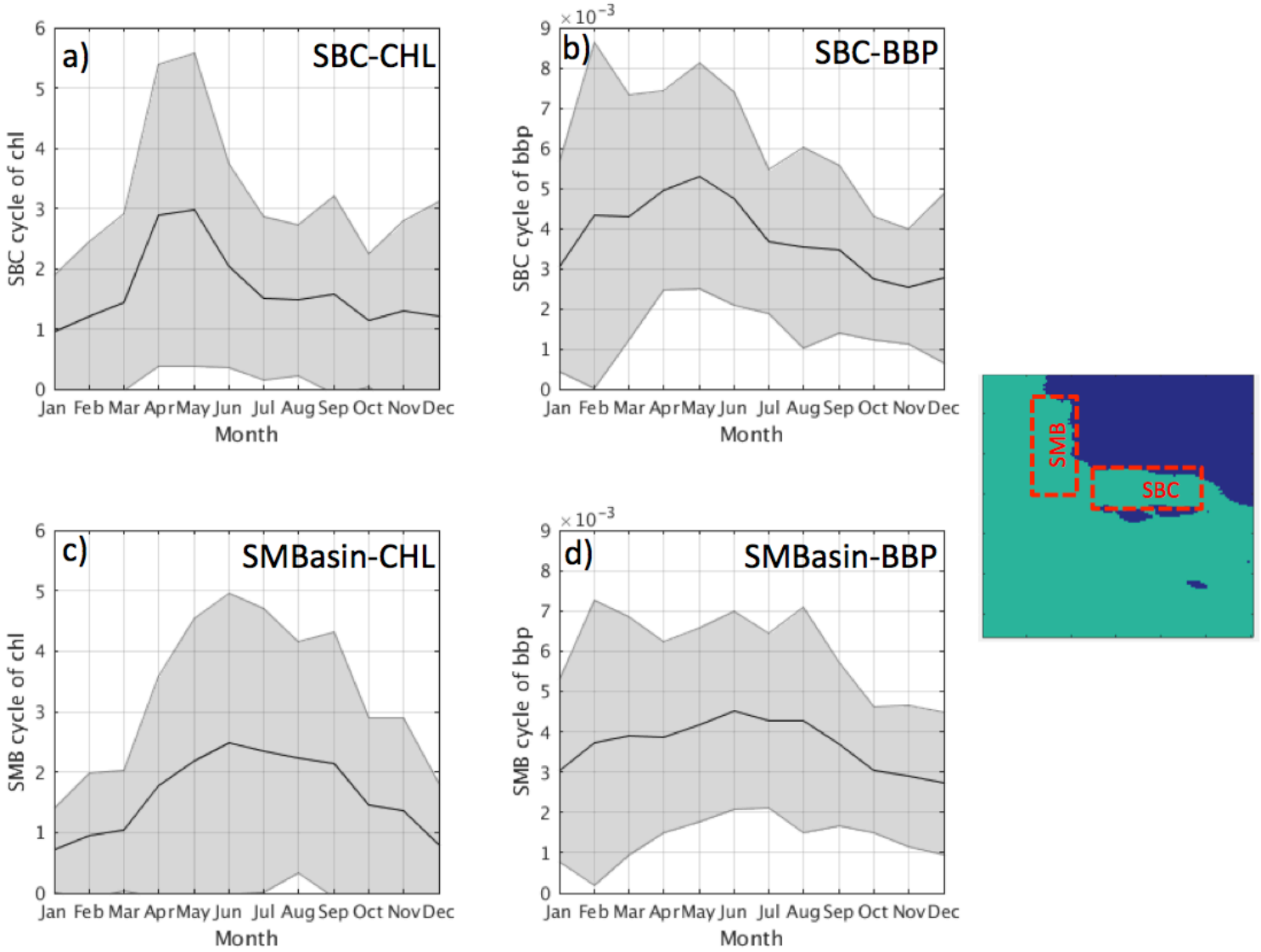

Figure 15. Mean seasonal cycle of CHL and BBP for specific regions of the domain highlighted on the map on the right.

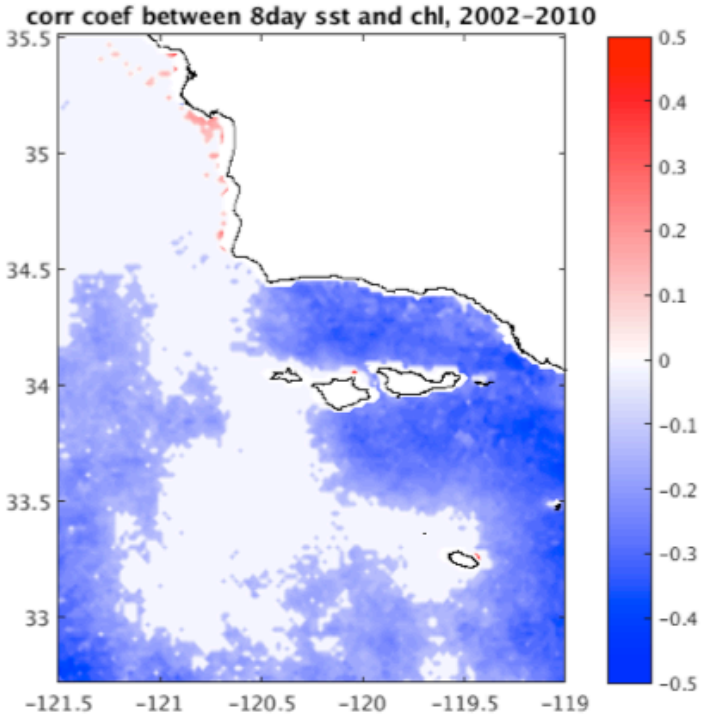

Figure 16. Correlation maps of the relationship between 8-day SST and 8-day CHL data. Data used is from 2002-2010.

APPENDICES

APPENDIX A

PDO and NPGO

The *PDO* index is derived as the leading amplitude function (from an EOF analysis) of monthly SST anomalies in the North Pacific Ocean, poleward of 20N. The monthly mean global average SST anomalies are removed (extracted from: http://research.jisao.washington.edu/pdo/PDO.latest). For more details, see:

Zhang, Y., J.M. Wallace, D.S. Battisti, 1997: ENSO-like interdecadal variability: 1900-93. J. Climate, 10, 1004-1020.

Similarly, the **NPGO** index is defined as the second leading mode of Sea Surface Height anomalies over the region between 180W – 110W and 25N – 62N (see https://www.ncdc.noaa.gov/teleconnections/enso/indicators/soi/).

SOI

The Southern Oscillation Index (SOI) is a standardized index based on the observed sea level pressure differences between Tahiti and Darwin, Australia. In general, smoothed time series of the SOI correspond very well with changes in ocean temperatures across the eastern tropical Pacific. The negative phase of the SOI represents below-normal air pressure at Tahiti (SLP) and above-normal air pressure at Darwin. Prolonged periods of negative (positive) SOI values coincide with abnormally warm (cold) ocean waters across the eastern tropical Pacific typical of El Niño (La Niña) episodes. The methodology used to calculate SOI is available below (Extracted from: https://www.ncdc.noaa.gov/teleconnections/enso/indicators/soi/)

Anomalies are departures from the 1951-1980 base period.

$$SOI = [\text{Standardized Tahiti} - \text{Standardized Darwin}] / \text{MSD}$$

Where Standardized Tahiti =

$$\text{sqrt}(\sum (\text{actual Tahiti SLP} - \text{mean Tahiti SLP})^2 / N),$$

where N is number of months, and

MSD is the Monthly Standard Deviation =

$$\text{sqrt}(\sum (\text{Standardized Tahiti} - \text{Standardized Darwin})^2 / N),$$

where Standardized Darwin =

$$[\text{Actual Darwin SLP} - \text{Mean Darwin SLP}] / \text{STD\_Darwin},$$

where STD_Darwin =

$$\text{sqrt}(\sum (\text{actual Darwin SLP} - \text{mean Darwin SLP})^2 / N),$$

where N is the number of summed months.

APPENDIX B

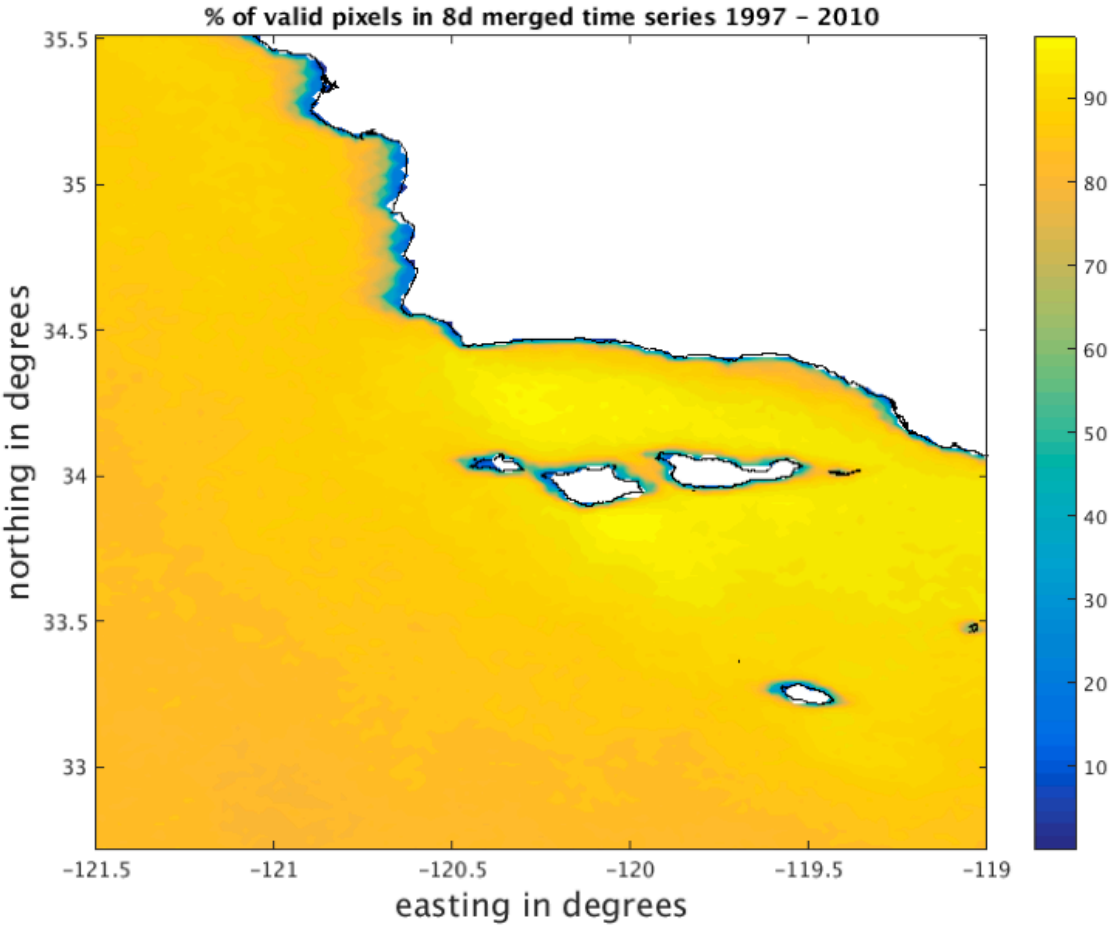

Figure B. % of valid pixels during the 1997-2010 period. A mask was created for pixels with coverage less than 60%.

APPENDIX C

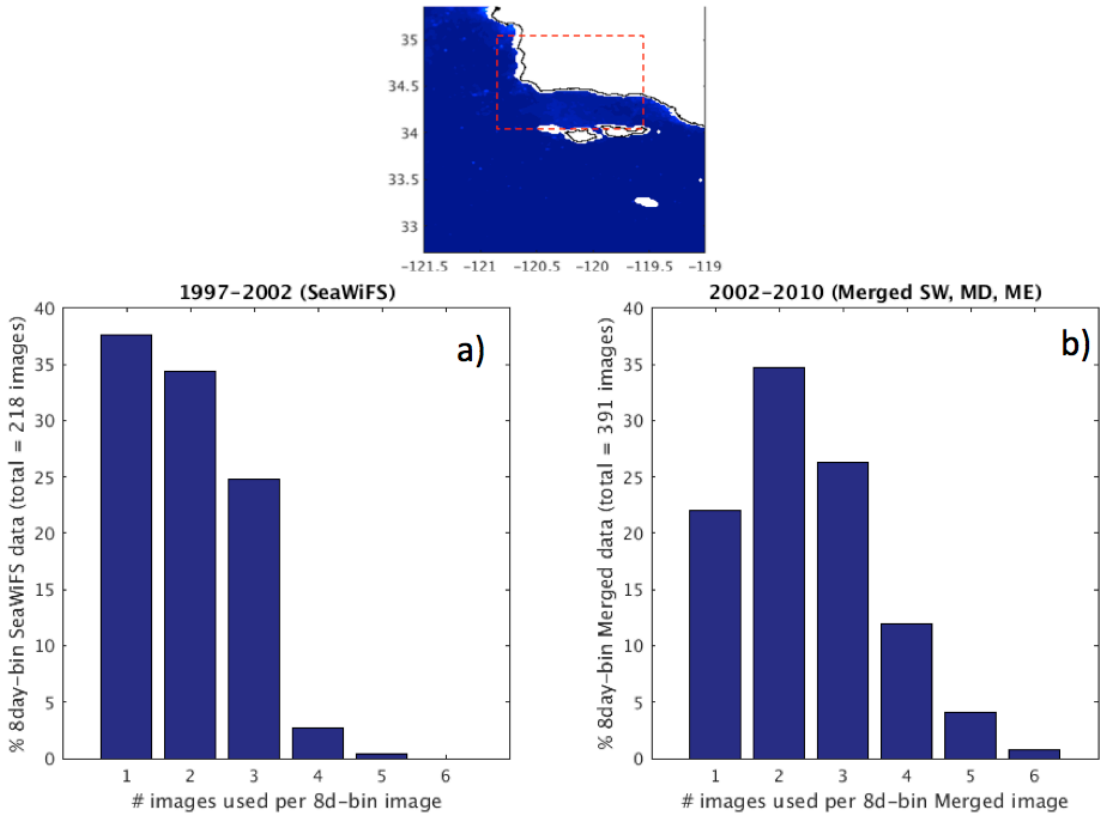

Figure C. Histogram of the number of days that make up each 8-day bin image of SeaWiFS (a) and the merged product (b). Only data from the area highlighted on the top panel is used here, since this is the area most sensitive to binning bias due to its high bio-optical variability.

APPENDIX D

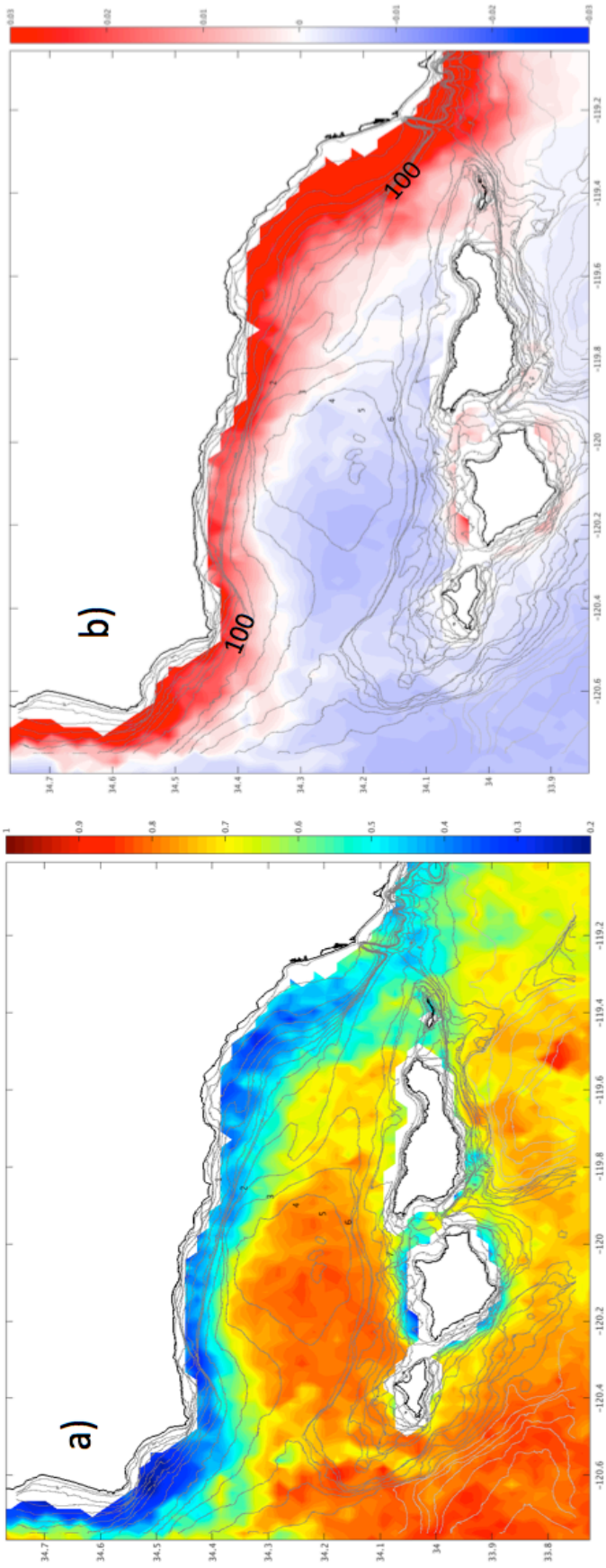

Figure D. Bathymetry overlaid on a) correlation coefficients between CHL and BBP; b) the second EOF mode for BBP variability.

APPENDIX E

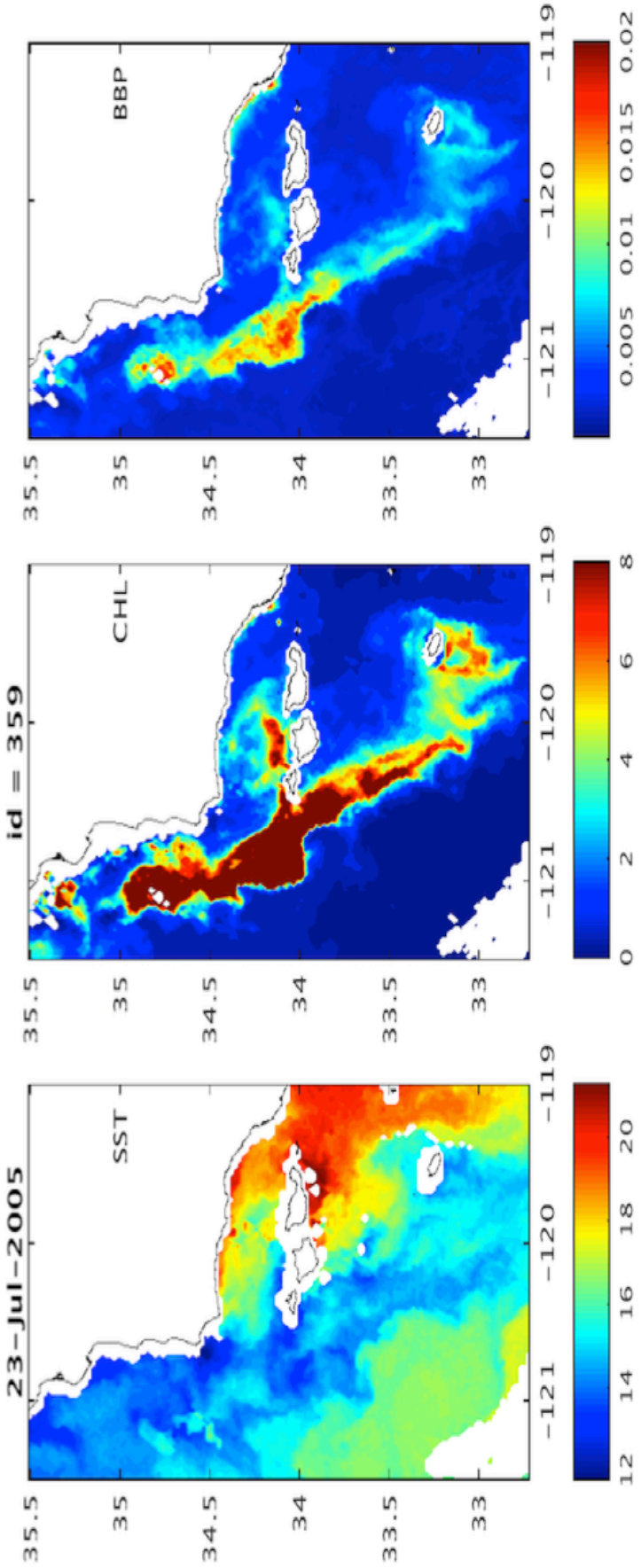

Figure E. SST, CHL and BBP estimates during July 23 2005 (+/- 4 days). During this period, NPGO is at its lowest but large CHL blooms are observed offshore along the CC. SST patterns show high variability and mixing.

APPENDIX F

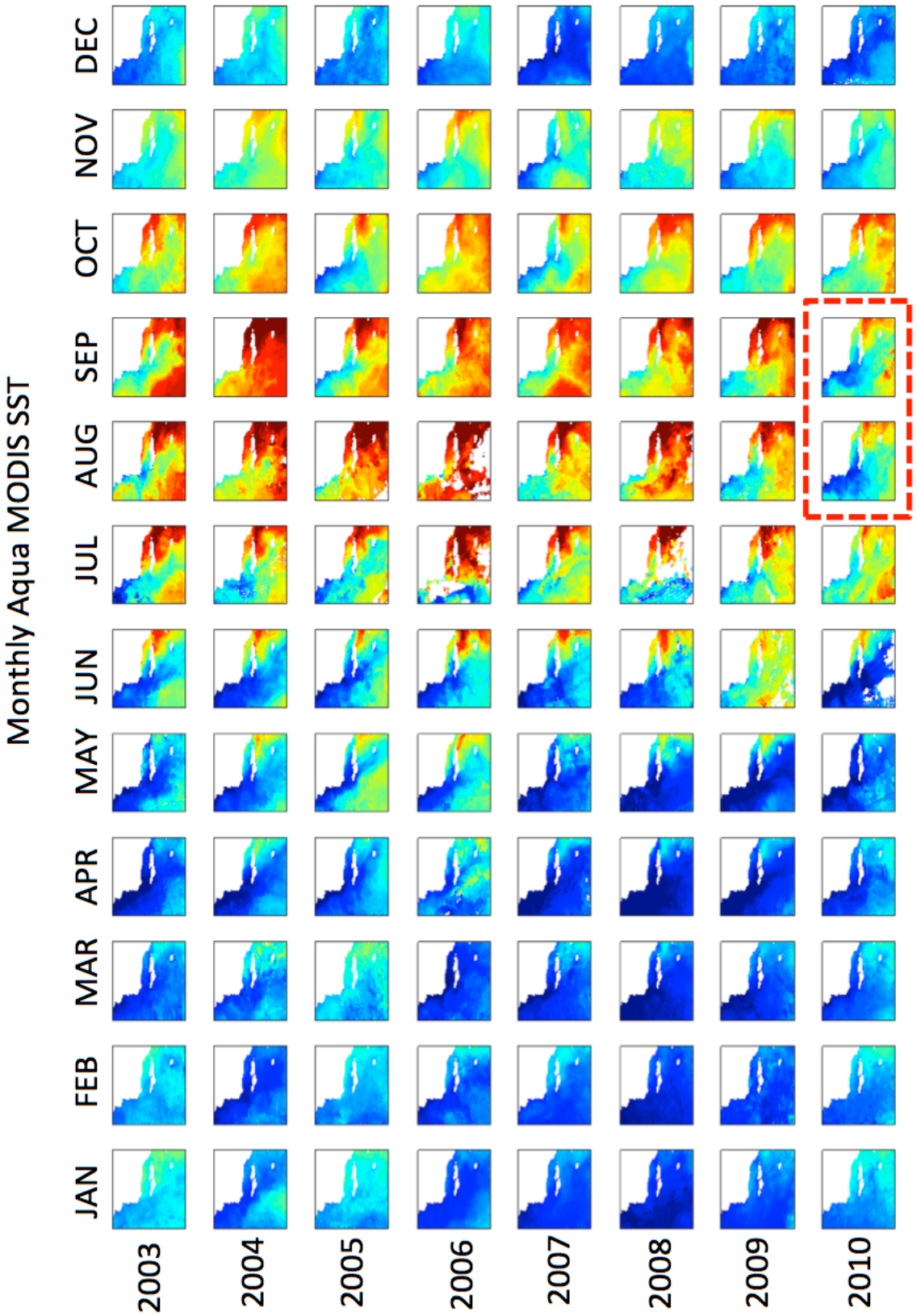

Figure F. Monthly SST estimates from 2002-2010. Highlighted it the anomalous August/September SST conditions during summer 2010.

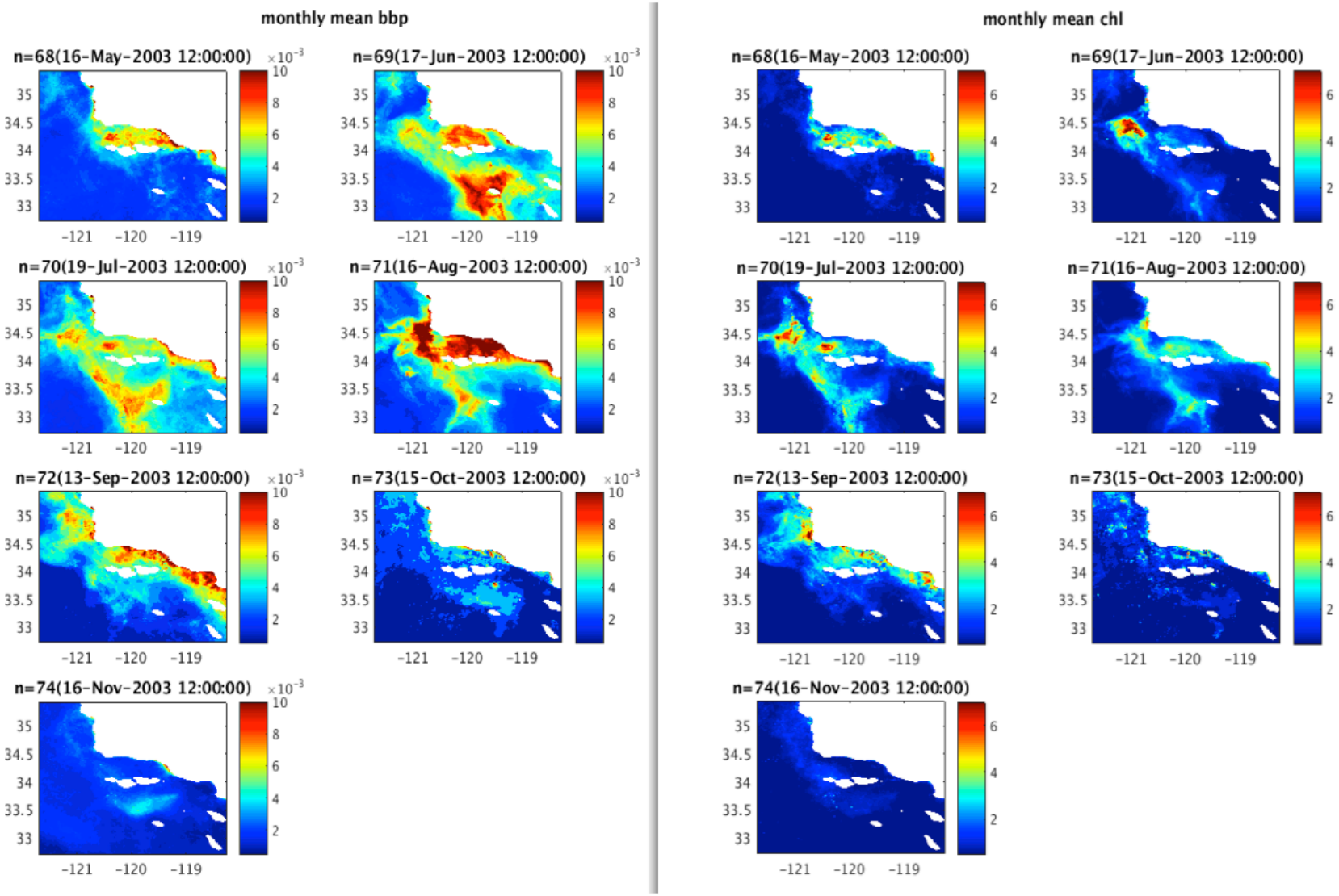

Figure G. Examples of large blooms with high BBP, low CHL content that resulted in large differences between CHL and BBP anomalies during 2003. Monthly data is shown (average time of each image is plotted along with the number of images used during each assemblage).

References

Aandera Data Instruments (2004). TD218 Operating Manual, Oxygen Optodes.

Anderson, C., D. A. Siegel, M. A. Brzezinski, and N. Guillocheau (2008), Controls on temporal patterns in phytoplankton community structure in the Santa Barbara Channel, California, *J. Geophys. Res.*, *113*(C4), C04038, doi:10.1029/2007JC004321.

Antoine, D., D. A. Siegel, T. S. Kostadinov, S. Maritorena, N. B. Nelson, B. Gentili, V. Vellucci, and N. Guillocheau (2011), Variability in optical particle backscattering in contrasting bio-optical oceanic regimes, *Limnol. Oceanogr.*, *56*(3), 955–973, doi:10.4319/lo.2011.56.3.0955.

Babin, M., A. Morel, V. Fournier-Sicre, F. Fell, and D. Stramski (2003), Light scattering properties of marine particles in coastal and open ocean waters as related to the particle mass concentration, *Limnol. Oceanogr.*, *48*(2), 843–859.

Bailey, S. W., and P. J. Werdell (2006), A multi-sensor approach for the on-orbit validation of ocean color satellite data products, *Remote Sens. Environ.*, *102*(1-2), 12–23, doi:10.1016/j.rse.2006.01.015.

Balch, W. M., D. T. Drapeau, B. C. Bowler, E. Lyczskowski, E. S. Booth, and D. Alley (2011), The contribution of coccolithophores to the optical and inorganic carbon budgets during the Southern Ocean Gas Exchange Experiment: New evidence in support of the "Great Calcite Belt" hypothesis, *J. Geophys. Res.*, *116*, C00F06, doi:10.1029/2011JC006941.

Barron, R. K., D. a. Siegel, and N. Guillocheau (2014), Evaluating the importance of phytoplankton community structure to the optical properties of the Santa Barbara Channel, California, *Limnol. Oceanogr.*, *59*(3), 927–946, doi:10.4319/lo.2014.59.3.0927.

Barron, R.K., D. Siegel, N. Nelson and N. Guillocheau (2015) Colored dissolved organic matter dynamics in a nearly autochthonous coastal site. *In Prep*.

Bassin, C.J., L. Washburn, M. Brzezinski, and E. McPhee-Shaw (2005), Sub-mesoscale coastal eddies observed by high frequency radar: A new mechanism for delivering nutrients to kelp forests in the Southern California Bight, *Geophysical Research Letters*, 32, doi:10.1029/2005GL023017.

Behrenfeld, M. J., R. T. O'Malley, D. a Siegel, C. R. McClain, J. L. Sarmiento, G. C. Feldman, A. J. Milligan, P. G. Falkowski, R. M. Letelier, and E. S. Boss (2006), Climate-driven trends in contemporary ocean productivity., *Nature*, *444*(7120), 752–5, doi:10.1038/nature05317.

Bell, T. W., K. C. Cavanaugh, D. C. Reed., D. A. Siegel (2015), Geographical variability in the controls of giant kelp biomass dynamics, *J. Biogeography*, 1-12, doi:10.1111/jbj.12550.

Bishop, C. M. (2008), Sensor Dynamics of Autonomous Underwater Gliders, 150pp., Memorial University of Newfoundland.

Bjornsson, H., and S. A. Venegas (1997), *A Manual for EOF and SVD analyses of Climatic Data*, Montreal, Quebec.

Bogucki, D., T. Dickey, and L. Redekopp (1997). Sediment resuspension and mixing through resonantly-generated internal solitary waves, *J. Phys. Oceanogr.*, 27, 1181-1196.

Bogucki, D.J., Redekopp, L.G., Barth, J. (2005). Internal solitary waves in the Coastal Mixing and Optics 1996 experiment: Multimodal structure and resuspension. *J. Geophys. Res.*, *110*, doi:10.1029/2003JC002253

Boss, E., and W. S. Pegau (2001), Relationship of light scattering at an angle in the backward direction to the backscattering coefficient., *Appl. Opt.*, *40*(30), 5503–7.

Boss, E., W. S. Pegau, W. D. Gardner, J. R. V. Zaneveld, A. H. Barnard, M. S. Twardowski, G. C. Chang, and T. D. Dickey (2001), Spectral particulate attenuation and particle size distribution in the bottom boundary layer of a continental shelf, *J. Geophys. Res.*, *106*(C5), 9509, doi:10.1029/2000JC900077.

Bray, N. A., A. Keyes, and W. M. L. Morawitz (1999), The California Current system in the Southern California Bight and the Santa Barbara Channel, *J. Geophys. Res.*, *104*(1998), 7695–7714.

Brzezinski, M. A., and L. Washburn (2011), Phytoplankton primary productivity in the Santa Barbara Channel: Effects of wind-driven upwelling and mesoscale eddies, *J. Geophys. Res.*, *116*(C12), doi:10.1029/2011JC007397.

Brzezinski, M., D. C. Reed, S. Harrer, A. Rassweiler, J. M. Melack, B. M. Goodridge, and J. E. Dugan (2013), Multiple sources and forms of nitrogen sustain year-round kelp growth on the inner continental shelf of the Santa Barbara Channel, *Oceanography*, *26*(3), 114–123, doi:http://dx.doi.org/ 10.5670/oceanog.2013.53.

Cacchione, A., D. E. Drake, U. S. G. Survey, M. Road, and M. Park (1986), Nepheloid Layers and Internal Waves Over Continental Shelves and Slopes, *Geo-Mar Let.*, 6 147–152.

Chang, G. C. (2002), Nearshore physical processes and bio-optical properties in the New York Bight, *J. Geophys. Res.*, *107*(C9), doi:10.1029/2001JC001018.

Chang, G.C. and Dickey, T.D. (2001). Optical and physical variability on timescales from minutes to the seasonal cycle on the New England shelf: July 1996 to June 1997. *J. Geophys. Res.*, *106*(C5)

Cheriton, O. M., E. E. McPhee-Shaw, W. J. Shaw, T. P. Stanton, J. Bellingham, and C. D. Storlazzi (2014), Suspended particulate layers and internal waves over the southern Monterey Bay continental shelf: An important control on shelf mud belts? *J. Geophys. Res. Ocean.*, *119*(1), 428–444, doi:10.1002/2013JC009360.

Clarke, T. L., B. Lesht, R. A. Young, D. J. P. Swift, and G. L. Freeland (1982), Sediment Resuspension by surfave-wave action: an examination of possible mechanisms, *Mar. Geol.*, *49*, 43–59.

Cloern, J. E., S. Q. Foster, and A. E. Kleckner, (2014), Phytoplankton primary production in the world's estuarine-coastal ecosystems. *Biogeosciences*, 11(9), 2477-2501.

Connolly, T. P., B. M. Hickey, S. L. Geier, and W. P. Cochlan (2010), Processes influencing seasonal hypoxia in the northern California Current System, J. Geophys. Res., 115(206), doi:10.1029/2009JC005283.Processes.

Cortés, A., F. J. Rueda, and M. G. Wells (2014), Experimental observations of the splitting of a gravity current at a density step in a stratified water body, *J. Geophys. Res. Ocean.*, *19,* 1038–1053, doi:10.1002/2013JC009304.

Cudaback, C. N. (2005), Subtidal inner-shelf circulation near Point Conception, California, *J. Geophys. Res.*, *110*(C10), C10007, doi:10.1029/2004JC002608.

Cullen, J. J. (1982), The deep chlorophyll maximum: comparing vertical profiles of chlorophyll a, *Can. J. Fish. Aquat. Sci.*, *39*, 791–803.

D'Sa, E. J., and R. L. Miller (2005), Bio-optical properties of coastal waters, in *Remote Sensing of Coastal Aquatic Environments*, pp. 129–155, Springer.

Deutsch, C., H. Brix, T. Ito, H. Frenzel, and L. Thompson (2011), Climate-forced variability of ocean hypoxia, *Science*, *333*(6040), 336–9, doi:10.1126/science.1202422.

Di Lorenzo E., Schneider N., Cobb K. M., Chhak, K, Franks P. J. S., Miller A. J., McWilliams J. C., Bograd S. J., Arango H., Curchister E., Powell T. M. and P. Rivere (2008) North Pacific Gyre Oscillation links ocean climate and ecosystem change. *Geophys. Res. Lett.*, 35, L08607, doi:10.1029/2007GL032838.

Dickey, T., Banner, M. L., Bhandari, P., Boyd, T., Carvalho, L., Chang, G., Chao, Y., Czerski, H., Darecki, M., Dong, C., Farmer, D., Freeman, S., Gemmrich, J., Gernez, P., Hall-Patch, N., Holt, B., Jiang, S., Jones, C., Kattawar, G., LeBel, D., Lenain, L., Lewis, M., Liu, Y., Logan, L., Manov, D., Melville, W. K., Moline, M. a., Morison, R., Nencioli, F., Pegau, W. S., Reineman, B., Robbins, I., Röttgers, R., Schultz, H., Shen, L., Shinki, M., Slivkoff, M., Sokólski, M., Spada, F., Statom, N., Stramski, D., Sutherland, P., Twardowski, M., Vagle, S., Van Dommelen, R., Voss, K., Washburn, L., Wei, J., Wijesekera, H., Wurl, O., Yang, D., Yildiz, S., You, Y., Yue, D. K. P., Zaneveld, R., Zappa, C. J. (2012). Introduction to special section on Recent Advances in the Study of Optical Variability in the Near-Surface and Upper Ocean, *J. Geophys. Res*., 117, C00H20, doi:10.1029/2012JC007964.

Dickey, T.D., E.C. Itsweire, M. Moline, and M.J. Perry (2008) Introduction to the Limnology and Oceanography Special Issue on Autonomous and Lagrangian Platforms and Sensors (ALPS), Limnol. Oceanogr. 53(2), Part 2: 2057-2061.

Dorman, C. E., and C. D. Winant (1995), Buoy observations of the atmosphere along the west coast of the United States, 1981-1990, *J. Geophys. Res.*, *100*(C8), 16,029–16,044.

Duarte, C. M., A. Regaudie-de-Gioux, J. M. Arrieta, A. Delgado-Huertas, and S. Agustí (2013), The oligotrophic ocean is heterotrophic, *Ann. Rev. Mar. Sci.*, *5*, 551–69, doi:10.1146/annurev-marine-121211-172337.

Ducklow, H. W., and S. C. Doney (2013), What is the metabolic state of the oligotrophic ocean? A debate. *Ann. Rev. Mar. Sci.*, *5*, 525–33, doi:10.1146/annurev-marine-121211-172331.

Edson, J. B., V. Jampana, R. A. WM8er, S. P. Bigorre, A. J. Plueddemann, C. W. Fairall, S. D. Miller, L. Mahrt, D. Vickers, and H. Hersbach (2013), On the exchange of momentum over the open ocean, *J. Phys. Oceanogr*., 43(8), 1589–1610, doi:10.1175/JPO-D-12-0173.1.

Emery, W.J. and Thomson, R.E. (2004). Data analysis methods in physical oceanography. Elsevier.

Fewings, M. R., L. Washburn, and J. C. Ohlmann (2015), Coastal water circulation patterns around the Northern Channel Islands and Point Conception, California, *Prog. Oceanogr.*, *2005*, 1–22, doi:10.1016/j.pocean.2015.10.001.

Fewings, M., S. J. Lentz, and J. Fredericks (2008), Observations of cross-shelf flow driven by cross-shelf winds on the inner continental shelf, *J. Phys. Oceanogr.*, *38*(11), 2358–2378, doi:10.1175/2008JPO3990.1.

Franks, P. J. S. (1992), Phytoplankton blooms at fronts: patterns, scales, and physical forcing mechanisms, *Rev. Aquat. Sci.*, *6*, 121–137.

García-Reyes, M., and J. Largier (2010), Observations of increased wind-driven coastal upwelling off central California, *J. Geophys. Res.*, *115*(C4), C04011, doi:10.1029/2009JC005576.

Garland, E. D., C. A. Zimmer, and S. J. Lentz (2002), Larval distributions in inner-shelf waters: The roles of wind-driven cross-shelf currents and diel vertical migrations, *Limnol. Oceanogr.*, *47*(3), 803–817, doi:10.4319/lo.2002.47.3.0803.

Glenn, S. M., C. Jones, M. S. Twardowski, L. Bowers, J. Kerfoot, J. Kohut, and D. C. Webb (2008), Glider observations of sediment resuspension in a Middle Atlantic Bight fall transition storm, *Limnol. Oceanogr.*, *53*, 2180–2196.

Goodman, J., M. A. Brzezinski, E. R. Halewood, and C. A. Carlson (2012), Sources of phytoplankton to the inner continental shelf in the Santa Barbara Channel inferred from cross-shelf gradients in biological, physical and chemical parameters, *Cont. Shelf Res.*, *48*, 27–39, doi:10.1016/j.csr.2012.08.011.

Gordon, H. R. (1997), Atmospheric correction of ocean color imagery in the Earth Observing System era, *J. Geophys. Res.*, *102*(D14), 17081–17106, doi:10.1029/96JD02443.

Gordon, H. R., and W. R. McCluney (1975), Estimation of the Depth of Sunlight Penetration in the Sea for Remote Sensing, *Appl. Opt*., 14(2), 413, doi:10.1364/AO.14.000413.

Graham, M. H., J. A. Vásquez, and A. H. Buschmann (2007), Global ecology of the giant kelp macrocystis: from ecotypes to ecosystems, *Oceanogr. Mar. Biol. An Annu. Rev.*, *45*, 39–88.

Gregg, W. W., and N. W. Casey (2007), Sampling biases in MODIS and SeaWiFS ocean chlorophyll data, *Remote Sens. Environ.*, *111*, 25 – 35, doi:10.1016/j.rse.2007.03.008.

Harms, S., and C. D. Winant (1998), Characteristic patterns of the circulation in the Santa Barbara Channel, *J. Geophys. Res.*, *103*, 3041–3065.

Hayward, T. L., and E. L. Venrick (1998), Nearsurface pattern in the California Current: coupling between physical and biological structure, *Deep Sea Res. Part II Top. Stud. Oceanogr.*, *45*(8-9), 1617–1638, doi:10.1016/S0967-0645(98)80010-6.

Hickey, B. M. (1979), The California Current System--hypotheses and facts 1, , *2*(October 1978).

Hill, A. E., B. M. Hickey, F. A. Shillington, P. T. Strub, K. H. Brink, E. D. Barton, and A. C. Thomas (1998), Eastern Ocean Boundaries, in *The Sea*, edited by A. R. R. and K. H. Brink, pp. 29–67, John Wiley & Sons, Inc.

Huettel, M., P. Berg., J. E. Kostka (2014), Benthic exchange and biogeochemical cycling in permeable sediments, *Annu. Rev. Mar. Sci.*, 6, 23-51.

International Ocean Colour Coordinating Group (IOCCG) (2000), Remote sensing of ocean colour in coastal, and other optically-complex waters., in *Reports of the International Ocean-Colour Coordinating Group*, edited by S. Sathyendranath.

Ito, T., M. J. Follows, and E. A. Boyle (2004), Is AOU a good measure of respiration in the oceans?, *Geophys. Res. Lett.*, *31*(17), L17305, doi:10.1029/2004GL020900.

Kahru, M., and B. G. Mitchell (2001), Seasonal and nonseasonal variability of satellite-derived chlorophyll and colored dissolved organic matter concentration in the California Current, *J. Geophys. Res.*, *106*(C2), 2517–2529.

Kahru, M., R. M. Kudela, M. Manzano-sarabia, and B. G. Mitchell (2009), Trends in primary production in the California Current detected with satellite data, *J. Geophys. Res.*, *114*, 1–7, doi:10.1029/2008JC004979.

Kahru, M., R. M. Kudela, M. Manzano-Sarabia, and B. Greg Mitchell (2012), Trends in the surface chlorophyll of the California Current: Merging data from multiple ocean color satellites, *Deep Sea Res. Part II Top. Stud. Oceanogr*, 77-80, 89–98, doi:10.1016/j.dsr2.2012.04.007.

Kahru, M., Z. Lee, R. M. Kudela, M. Manzano-Sarabia, and B. Greg Mitchell (2015), Multi-satellite time series of inherent optical properties in the California Current, *Deep Sea Res. Part II Top. Stud. Oceanogr*, 112, 91–106, doi:10.1016/j.dsr2.2013.07.023.

Kortzinger, A., J. Schimanski, U. Send, and D. Wallace (2004), The ocean takes a deep breath, *Science, 306*.

Kostadinov, T. S., D. A. Siegel, S. Maritorena, and N. Guillocheau (2012), Optical assessment of particle size and composition in the Santa Barbara Channel, California, *Appl. Opt.*, *51*(9), 1–19.

Kostadinov, T. S., D. A. Siegel, S. Maritorena, and N. Guillocheau (2007), Ocean color observations and modeling for an optically complex site: Santa Barbara Channel, California, USA, *J. Geophys. Res.*, *112*(C7), 1–15, doi:10.1029/2006JC003526.

Krause, J. W., M. a. Brzezinski, D. a. Siegel, and R. C. Thunell (2013), Biogenic silica standing stock and export in the Santa Barbara Channel ecosystem, *J. Geophys. Res. Ocean.*, *118*(2), 736–749, doi:10.1029/2012JC008070.

Kudela, R. M., S. Seeyave, and W. P. Cochlan (2010), The role of nutrients in regulation and promotion of harmful algal blooms in upwelling systems, *Prog. Oceanogr.*, *85*(1-2), 122–135, doi:10.1016/j.pocean.2010.02.008.

Lamb, K. G. (2014), Internal wave breaking and dissipation mechanisms on the continental slope/shelf, *Annu. Rev. Fluid Mech.*, *46*(1), 231–254, doi:10.1146/annurev-fluid-011212-140701.

Lefort, T., and J. M. Gasol (2013), Short-time scale coupling of picoplankton community structure and single-cell heterotrophic activity in winter in coastal NW Mediterranean Sea waters, *J. Plankton Res.*, *36*(1), 243–258, doi:10.1093/plankt/fbt073.

Legaard, K. R., and A. C. Thomas (2006), Spatial patterns in seasonal and interannual variability of chlorophyll and sea surface temperature in the California Current, *J. Geophys. Res.*, *111*(C6), C06032, doi:10.1029/2005JC003282.

Lentz, S. J. (1995), Sensitivity of the inner-shelf circulation to the form of the eddy viscosity profile, *J. Phys. Oceanogr.*, *25*, 19–28.

Lentz, S. J., and M. R. Fewings (2012), The wind- and wave-driven inner-shelf circulation., *Ann. Rev. Mar. Sci.*, *4*, 317–43, doi:10.1146/annurev-marine-120709-142745.

Lévy, M., D. Iovino, L. Resplandy, P. Klein, G. Madec, A.M. Tréguier, S. Masson and K. Takahashi (2012), Large-scale impacts of submesoscale dynamics on phytoplankton: Local and remote effects, *Ocean Model*, *43-44*, 77–93, doi:10.1016/j.ocemod.2011.12.003.

Lorenzoni, L., R. C. Thunell, C. R. Benitez-Nelson, D. Hollander, N. Martinez, E. Tappa, R. Varela, Y. Astor, and F. E. Muller-Karger (2009), The importance of subsurface nepheloid layers in transport and delivery of sediments to the eastern Cariaco Basin, Venezuela, *Deep Sea Res. Part I Oceanogr. Res. Pap*, *56*(12), 2249–2262, doi:10.1016/j.dsr.2009.08.001.

Lorke, a., D. F. McGinnis, and a. Maeck (2013), Eddy-correlation measurements of benthic fluxes under complex flow conditions: Effects of coordinate transformations and averaging time scales, *Limnol. Oceanogr. Methods*, *11*(8), 425–437, doi:10.4319/lom.2013.11.425.

Lucas, A. J., C. L. Dupont, V. Tal, J. L. Largier, B. Palenik, P. J. S. Franks, and V. Tai (2011), The green ribbon: Multiscale physical control of phytoplankton productivity and community structure over a narrow continental shelf, *Limnol. Oceanogr.*, *56*(2), 611–626, doi:10.4319/lo.2011.56.2.0611.

Mann, K.H. and J.R.N Lazier (1991). *Dynamics of marine ecosystems: biological-physical interactions in the oceans*, 2nd ed. Cambridge, Mass. Blackwell Science.

Maritorena, S., D. A. Siegel, and A. R. Peterson (2002), Optimization of a semianalytical ocean color model for global-scale applications., *Appl. Opt.*, *41*(15), 2705–14.

Maritorena, S., O. H. F. d'Andon, A. Mangin, and D. a. Siegel (2010), Merged satellite ocean color data products using a bio-optical model: Characteristics, benefits and issues, *Remote Sens. Environ.*, *114*(8), 1791–1804, doi:10.1016/j.rse.2010.04.002.

McPhee-Shaw, E. E. (2006). Boundary-interior exchange: Reviewing the idea that internal-wave mixing enhances lateral dispersal near continental margins, *Deep Sea Res. Part II Top. Stud. Oceanogr, 53,* 42-59.

McPhee-Shaw, E. E., and E. Kunze (2002), Boundary layer intrusions from a sloping bottom: A mechanisms for generating intermediate nepheloid layers, *J. Geophys. Res.*, *107,* 1-16.

McPhee-Shaw, E. E., D. A. Siegel, L. Washburn, M. A. Brzezinski, J. L. Jones, A. Leydecker, and J. Melack (2007), Mechanisms for nutrient delivery to the inner shelf : Observations from the Santa Barbara Channel, *Limnol. Oceanogr.*, *52*(5), 1748–1766.

Melton, C., L. Washburn, and C. Gotschalk (2009), Wind relaxations and poleward flow events in a coastal upwelling system on the central California coast, *J. Geophys. Res.*, *114*(C11), 1–18, doi:10.1029/2009JC005397.

Mertes, L. a. K., and J. a. Warrick (2001), Measuring flood output from 110 coastal watersheds in California with field measurements and SeaWiFS, *Geology*, *29*(7), 659, doi:10.1130/0091-7613(2001)029<0659:MFOFCW>2.0.CO;2.

Miller, R. J., D. C. Reed, and M. aA?. Brzezinski (2011), Partitioning of primary production among giant kelp (Macrocystis pyrifera), understory macroalgae, and phytoplankton on a temperate reef, *Limnol. Oceanogr.*, *56*(1), 119–132, doi:10.4319/lo.2011.56.1.0119.

Nezlin, N. P., M. a. Sutula, R. P. Stumpf, and A. Sengupta (2012), Phytoplankton blooms detected by SeaWiFS along the central and southern California coast, *J. Geophys. Res.*, *117*(C7), C07004, doi:10.1029/2011JC007773.

Nishimoto, M. M., and L. Washburn (2002), Patterns of coastal eddy circulation and abundance of pelagic juvenile fish in the Santa Barbara, *Mar. Ecol. Prog. Ser.*, *241*, 183–199.

Nittrouer, C. A., and L. D. Wright (1994), Transport of particles across continental shelves, *Rev. Geophys*, *32*, 85–113.

Omand, M. M., J. J. Leichter, P. J. S. Franks, R. T. Guza, A. J. Lucas, and F. Feddersen (2011), Physical and biological processes underlying the sudden surface appearance of a red tide in the nearshore, *Limnol. Oceanogr.*, *56*(3), 787–801, doi:10.4319/lo.2011.56.3.0787.

Otero, M. P., and D. A. Siegel (2004), Spatial and temporal characteristics of sediment plumes and phytoplankton blooms in the Santa Barbara Channel, *Deep Sea Res. Part II Top. Stud. Oceanogr.*, *51*(10-11), 1129–1149, doi:10.1016/j.dsr2.2004.04.004.

Paduan, J. D., and L. Washburn (2013), High-frequency radar observations of ocean surface currents., *Ann. Rev. Mar. Sci.*, *5*, 115–36, doi:10.1146/annurev-marine-121211-172315.

Pak, H., J. R. V Zaneveld, and J. Kitchen (1980) Intermediate nepheloid layers observed off Oregon and Washington, *J. Geophys. Res, 85*(Cll), 6697–6708.

Perry, M. J., and D. L. Rudnick (2003), Special Issue — Ocean Observations Observing the Ocean with Autonomous and Lagrangian Platforms and Sensors (ALPS): the Role of ALPS in Sustained Ocean Observing Systems, *Oceanography*, *16*(4), 31–36.

Pineda, J., and M. Lopez (2002), Temperature, stratification and barnacle larval settlement in two Californian sites, *Cont. Shelf Res.*, *22*, 1183–1198.

Pinkel, R., M.A. Goldin, J.A. Smith, O.M. Sun, A.A. Aja, M.N. Bui, and T. Hughen (2011) The Wirewalker: a vertically profiling instrument carrier powered by ocean waves. *J. Atmos. Oceanic Technol.*, *28*, 426–435.

Roesler, C. S., and A. H. Barnard (2013), Optical proxy for phytoplankton biomass in the absence of photophysiology: Rethinking the absorption line height, *Methods Oceanogr.*, *7*, 79–94, doi:10.1016/j.mio.2013.12.003.

Romero, L., Y. Uchiyama, J. C. Ohlmann, J. C. McWilliams, and D. A. Siegel (2013), Simulations of Nearshore Particle-Pair Dispersion in Southern California, *J. Phys. Oceanogr.*, *43*(9), 1862–1879, doi:10.1175/JPO-D-13-011.1.

Rowe, G. T., C. H. Clifford, K. L. Smith Jr, and P. L. Hamilton (1975), Benthic nutrient regeneration and its coupling to primary productivity in coastal waters, *Nature*, *255*.

Rudnick, D. L. (2015), Ocean Research Enabled by Underwater Gliders, *Ann. Rev. Mar. Sci.*, (August), 1–23, doi:10.1146/annurev-marine-122414-033913.

Rudnick, D. L., R. E. Davis, C. C. Eriksen, D. M. Fratantoni, and M. J. Perry (2004), Underwater gliders for ocean research, *Mar. Technol. Soc. J.*, *38*(1), 48–59.

Santer, R., and C. Schmechtig (2000), Adjacency Effects on Water Surfaces: Primary Scattering Approximation and Sensitivity Study, *Appl. Opt.*, *39*(3), 361, doi:10.1364/AO.39.000361.

Santoro, A. E., N. J. Nidzieko, G. L. Van Dijken, K. R. Arrigo, and A. B. Boehma (2010), Contrasting spring and summer phytoplankton dynamics in the nearshore Southern California Bight, *Limnol. Oceanogr.*, *55*(1), 264–278, doi:10.4319/lo.2010.55.1.0264.

SBC-LTER, Washburn, L., Brzezinski, M. A., Carlson, C. A., Siegel, D. A. 2014. SBC LTER: Ocean Currents and Biogeochemistry: Nearshore water profiles (monthly CTD and chemistry) knb-lter-sbc.10.21.

Schofield, O., Bergmann, T., Bissett, P., Grassle, J.F., Haidvogel, D.B., Kohut, J., Moline, M., Glenn, S.M. (2002). The Long-Term Ecosystem Laboratory: an integrated coastal observatory, *IEEE J. Ocean. Eng*, 27(2), 146-154.

Siegel, D. A. (2005), Consistent merging of satellite ocean color data sets using a bio-optical model, *Remote Sens. Environ.*, *94*, 429 – 440, doi:10.1016/j.rse.2004.08.014.

Siegel, D. A. et al. (2013), Regional to global assessments of phytoplankton dynamics from the SeaWiFS mission, *Remote Sens. Environ.*, *135*, 77–91, doi:10.1016/j.rse.2013.03.025.

Smith, R. C., and K. S. Baker (1981), Optical properties of the clearest natural waters (200–800 nm), *Appl. Opt. 20*(2), 177, doi:10.1364/AO.20.000177.

Stramski, D. (1999), Estimation of Particulate Organic Carbon in the ocean from satellite remote sensing, *Science 285* (5425), 239–242, doi:10.1126/science.285.5425.239.

Stramski, D., E. Boss, D. Bogucki, and K. J. Voss (2004), The role of seawater constituents in light backscattering in the ocean, *Prog. Oceanogr.*, *61*(1), 27–56, doi:10.1016/j.pocean.2004.07.001.

Thomas, a. C., M.-E. Carr, and P. T. Strub (2001), Chlorophyll variability in eastern boundary currents, *Geophys. Res. Lett.*28(18), 3421–3424, doi:10.1029/2001GL013368.

Thomas, A., and P. Ted Strub (2001), Cross-shelf phytoplankton pigment variability in the California Current, *Cont. Shelf Res.*, 21(11-12), 1157–1190, doi:10.1016/S0278-4343(01)00006-1.

Toole, D. A., and D. A. Siegel (2001), Modes and mechanisms of ocean color variability in the Santa Barbara Channel, *J. Geophys. Res.*, *106*, 26,985 – 27,000.

Treguier, a. M., J. Deshayes, C. Lique, R. Dussin, and J. M. Molines (2012), Eddy contributions to the meridional transport of salt in the North Atlantic, *J. Geophys. Res.*, *117*(C5), C05010, doi:10.1029/2012JC007927.

van Loon, H. (1979), The association between latitudinal temperature gradient and eddy transport. Part I: Transport of sensible heat in winter, *Mon. Weather Rev.*, *107*, 525–534.

Venegas, R. M., P. T. Strub, E. Beier, R. Letelier, A. C. Thomas, T. Cowles, C. James, L. Soto-Mardones, and C. Cabrera (2008), Satellite-derived variability in chlorophyll, wind stress, sea surface height, and temperature in the northern California Current System, *J. Geophys. Res.*, *113*(C3), C03015, doi:10.1029/2007JC004481.

Warrick, J.A. (2002), Short-term (1997-2000) and long-term (1928-2000) observations of river water and sediment discharge to the Santa Barbara Channel, California. PhD Dissertation, University of California, Santa Barbara.

Warrick, J. A., Mertes, L. A., Washburn, L., & Siegel, D. A. (2004), A conceptual model for river water and sediment dispersal in the Santa Barbara Channel, California, *Cont. Shelf Res.*, *24*(17), 2029–2043, doi:10.1016/j.csr.2004.07.010.

Warrick, J. a., L. Washburn, M. A. Brzezinski, and D. A. Siegel (2005), Nutrient contributions to the Santa Barbara Channel, California, from the ephemeral Santa Clara River, *Estuar. Coast. Shelf Sci.*, *62*(4), 559–574, doi:10.1016/j.ecss.2004.09.033

Webb, D. C., P. J. Simonetti, and C. P. Jones (2001), SLOCUM: an underwater glider propelled by environmental energy, *IEEE J. Ocean. Eng.*, *26*(4), 447–452, doi:10.1109/48.972077.

Wiggert, J., T. D. Dickey, and T. Granata (1994), The effect of temporal undersampling on primary production estimates, *J. Geophys. Res.*, *99*, 3361–3371.

Williams, P. J. L. B., P. D. Quay, T. K. Westberry, and M. J. Behrenfeld (2013), The oligotrophic ocean is autotrophic, *Ann. Rev. Mar. Sci.*, 5, 535–49, doi:10.1146/annurev-marine-121211-172335.

Zhang, X., L. Hu, and M.-X. He (2009), Scattering by pure seawater: effect of salinity., *Opt. Express*, *17*(7), 5698–710.